

REPORT DOCUMENTATION PAGE			Form Approved OMB NO. 0704-0188		
<p>The public reporting burden for this collection of information is estimated to average 1 hour per response, including the time for reviewing instructions, searching existing data sources, gathering and maintaining the data needed, and completing and reviewing the collection of information. Send comments regarding this burden estimate or any other aspect of this collection of information, including suggestions for reducing this burden, to Washington Headquarters Services, Directorate for Information Operations and Reports, 1215 Jefferson Davis Highway, Suite 1204, Arlington VA, 22202-4302. Respondents should be aware that notwithstanding any other provision of law, no person shall be subject to any penalty for failing to comply with a collection of information if it does not display a currently valid OMB control number.</p> <p>PLEASE DO NOT RETURN YOUR FORM TO THE ABOVE ADDRESS.</p>					
1. REPORT DATE (DD-MM-YYYY) 29-08-2017		2. REPORT TYPE Final Report		3. DATES COVERED (From - To) 1-Jul-2013 - 30-Jun-2017	
4. TITLE AND SUBTITLE Final Report: Studies of ARO-Relevant Fuels using Shock Tube/Laser Absorption Methods			5a. CONTRACT NUMBER W911NF-13-1-0206		
			5b. GRANT NUMBER		
			5c. PROGRAM ELEMENT NUMBER 611102		
6. AUTHORS			5d. PROJECT NUMBER		
			5e. TASK NUMBER		
			5f. WORK UNIT NUMBER		
7. PERFORMING ORGANIZATION NAMES AND ADDRESSES Stanford University 3160 Porter Drive Suite 100 Stanford, CA 94304 -8445			8. PERFORMING ORGANIZATION REPORT NUMBER		
9. SPONSORING/MONITORING AGENCY NAME(S) AND ADDRESS (ES) U.S. Army Research Office P.O. Box 12211 Research Triangle Park, NC 27709-2211			10. SPONSOR/MONITOR'S ACRONYM(S) ARO		
			11. SPONSOR/MONITOR'S REPORT NUMBER(S) 63142-EG.18		
12. DISTRIBUTION AVAILABILITY STATEMENT Approved for public release; distribution is unlimited.					
13. SUPPLEMENTARY NOTES The views, opinions and/or findings contained in this report are those of the author(s) and should not be construed as an official Department of the Army position, policy or decision, unless so designated by other documentation.					
14. ABSTRACT					
15. SUBJECT TERMS					
16. SECURITY CLASSIFICATION OF:			17. LIMITATION OF ABSTRACT UU	15. NUMBER OF PAGES	19a. NAME OF RESPONSIBLE PERSON Ronald Hanson
a. REPORT UU	b. ABSTRACT UU	c. THIS PAGE UU			19b. TELEPHONE NUMBER 650-723-6850

RPPR Final Report

as of 12-Oct-2017

Agency Code:

Proposal Number: 63142EG

Agreement Number: W911NF-13-1-0206

INVESTIGATOR(S):

Name: Ronald Hanson
Email: rkhanson@stanford.edu
Phone Number: 6507236850
Principal: Y

Organization: **Stanford University**

Address: 3160 Porter Drive, Stanford, CA 943048445

Country: USA

DUNS Number: 009214214

EIN: 941156365

Report Date: 30-Sep-2017

Date Received: 29-Aug-2017

Final Report for Period Beginning 01-Jul-2013 and Ending 30-Jun-2017

Title: Studies of ARO-Relevant Fuels using Shock Tube/Laser Absorption Methods

Begin Performance Period: 01-Jul-2013

End Performance Period: 30-Jun-2017

Report Term: 0-Other

Submitted By: Ronald Hanson

Email: rkhanson@stanford.edu

Phone: (650) 723-6850

Distribution Statement: 1-Approved for public release; distribution is unlimited.

STEM Degrees: 5

STEM Participants: 5

Major Goals: Validation and refinement of reaction mechanisms and development of new and improved reduced mechanisms describing the pyrolysis, oxidation and ignition of practical fuels requires a reliable database of experimental combustion targets. This database must cover relevant combustion conditions and encompass realistic practical fuels, fuel surrogate mixtures and individual surrogate components. Shock tubes and laser absorption diagnostics are able to provide three important types of experimental measurements for this database: ignition delay times, species concentration time-histories and elementary reaction rate constants. These experimental methods are the mainstay of this ARO research program at Stanford.

The primary scientific problem that this research addresses is the need for a very high-quality experimental database with which to test and refine detailed reaction mechanisms for jet and diesel fuel surrogates. Over the past several years, we have made several advances in shock tube and laser absorption methodology that we believe are strongly supportive of the desired rapid advancement of fuel research in this area.

Research was performed in three main areas: improvements to shock tube performance, ignition delay times and species time-histories, and high-speed end-wall imaging.

Accomplishments: See uploaded document.

Training Opportunities: Students working under this grant benefited from training and education in the areas of combustion, propulsion, laser diagnostics and shock tube methods. The greater portion of the graduate students who have pursued higher degrees, M.Sc. and Ph.D., under the supervision of Professor R. K. Hanson at Stanford University have done so with the support of DoD funding. (Over 100 students have received Ph.D. degrees from the Hanson group.) Students have learned to develop and use state-of-the-art laser diagnostic and spectroscopic techniques, to design and use shock tube facilities, and to apply these tools to studying current combustion problems of interest to the ARO. At present count, 28 of the graduating students have gone on to become professors in their own right. Students who work on this equipment will be well-trained in new scientific methods and able to pursue careers as leaders in science and engineering in the United States.

Results Dissemination: Descriptions of the research have been presented at conferences annually including the International Symposium on Combustion, the International Symposium on Shock Waves and the International Colloquium on the Dynamics of Explosions and Reactive Systems. Research is described in a wide range of publications and conference proceedings. Advances in the research have also been disseminated through technology transfer described in a separate section.

RPPR Final Report

as of 12-Oct-2017

Honors and Awards: Professor Ronald K. Hanson was awarded the following honors during this contract:

2016 Energy Systems Award, AIAA
2016 H. S. Tsien Professorship, China Academy of Sciences
2015 Milton Van Dyke Award, American Physical Society
2015 David Goodwin Memorial Lecture, Caltech, inaugural speaker
2014 Honorary Prof. Appt. at Xi'an Jiaotong U. & Northwestern Polytechnic U.

Protocol Activity Status:

Technology Transfer: The following collaborations and technology transfers occurred during this contract:

- Dr. Chiping Li, AFOSR: collaborative effort to develop HyChem model for AF and ARO-relevant fuels. ARO-supported shock tube development has enabled the extension of HyChem-required speciation measurements to the NTC regime
- Dr. Josh Heyne, Univ. Dayton and Dr. Mohan Gupta, FAA/DOE: collaboration with NJFCP program for the development of compact (HyChem) models for jet fuels.
- Dr. Ken Brezinsky, Univ. Illinois-Chicago: direct collaboration and comparison of shock tube data from two different laboratories. This work resulted in the refinement of interpretation of shock tube measurements at different facilities.
- Dr. Tim Edwards, AF Wright Patterson: use of AF facilities to analysis fuel samples.
- Dr. Chol-Bum Kweon, M CIV USARMY RDECOM ARL (US): we studied a series of kerosene samples with varying cetane number provide by RDECOM to test the HyChem approach for variant fuels.
- Dr. Arjun Prakash, SHELL Houston: application of ARO-developed shock tube/laser absorption methods to characterize gasoline pyrolysis and oxidation to assist in the development of HyChem models for selected gasolines and anti-knock additives.

PARTICIPANTS:

Participant Type: PD/PI

Participant: Ronald K Hanson

Person Months Worked: 1.00

Project Contribution:

International Collaboration:

International Travel:

National Academy Member: Y

Other Collaborators:

Funding Support:

Participant Type: Staff Scientist (doctoral level)

Participant: David F Davidson

Person Months Worked: 1.00

Project Contribution:

International Collaboration:

International Travel:

National Academy Member: N

Other Collaborators:

Funding Support:

Participant Type: Graduate Student (research assistant)

Participant: Matthew Campbell

Person Months Worked: 6.00

Project Contribution:

International Collaboration:

International Travel:

National Academy Member: N

Other Collaborators:

Funding Support:

RPPR Final Report
as of 12-Oct-2017

Participant Type: Graduate Student (research assistant)

Participant: Yangye Zhu

Person Months Worked: 6.00

Funding Support:

Project Contribution:

International Collaboration:

International Travel:

National Academy Member: N

Other Collaborators:

Participant Type: Graduate Student (research assistant)

Participant: Alison Ferris

Person Months Worked: 6.00

Funding Support:

Project Contribution:

International Collaboration:

International Travel:

National Academy Member: N

Other Collaborators:

Participant Type: Graduate Student (research assistant)

Participant: Valerie Troutman

Person Months Worked: 3.00

Funding Support:

Project Contribution:

International Collaboration:

International Travel:

National Academy Member: N

Other Collaborators:

Participant Type: Graduate Student (research assistant)

Participant: Andrew Tulgestke

Person Months Worked: 6.00

Funding Support:

Project Contribution:

International Collaboration:

International Travel:

National Academy Member: N

Other Collaborators:

ARTICLES:

RPPR Final Report as of 12-Oct-2017

Publication Type: Journal Article

Peer Reviewed: Y

Publication Status: 1-Published

Journal: Fuel

Publication Identifier Type: DOI

Publication Identifier: 10.1016/j.fuel.2014.02.050

Volume: 126

Issue: 0

First Page #: 0

Date Submitted:

Date Published:

Publication Location:

Article Title: Ignition delay times of very-low-vapor-pressure biodiesel surrogates behind reflected shock waves

Authors:

Keywords: Aerosol shock tube Very-low-vapor-pressure, Biodiesel surrogate, Fatty Acid Methyl Ester (FAME), Ignition delay time

Abstract: Ignition delay times for a variety of low-vapor-pressure biodiesel surrogates were measured behind reflected shock waves, using an aerosol shock tube. These fuels included methyl decanoate (C₁₁H₂₂O₂), methyl laurate (C₁₃H₂₆O₂), methyl myristate (C₁₅H₃₀O₂), methyl palmitate (C₁₇H₃₄O₂), and a methyl oleate (C₁₉H₃₆O₂)/Fatty Acid Methyl Ester (FAME) blend. Experiments were conducted in 4% oxygen/ argon mixtures with the exception of methyl decanoate which was studied in 1% and 21% oxygen/argon blends. Reflected shock conditions covered initial temperatures from 1026 to 1388 K, pressures of 3.5 and 7.0 atm, and equivalence ratios from 0.3 to 1.4. Arrhenius expressions describing the experimental ignition delay time data are given and compared to those derived from applicable mechanisms available in the literature. Graphical comparisons between experimental data and mechanism predictions are also provided. Experiments of methyl laurate, methyl myristate, and methyl palmitate represent the fi

Distribution Statement: 1-Approved for public release; distribution is unlimited.

Acknowledged Federal Support:

Publication Type: Journal Article

Peer Reviewed: Y

Publication Status: 1-Published

Journal: Review of Scientific Instruments

Publication Identifier Type: DOI

Publication Identifier: 10.1063/1.4875056

Volume: 85

Issue: 5

First Page #: 55108

Date Submitted:

Date Published:

Publication Location:

Article Title: A second-generation constrained reaction volume shock tube

Authors:

Keywords: Constrained reaction volume strategy, shock tube, constant pressure

Abstract: We have developed a shock tube that features a sliding gate valve in order to mechanically constrain the reactive test gas mixture to an area close to the shock tube endwall, separating it from a specially formulated non-reactive buffer gas mixture. This second-generation Constrained Reaction Volume (CRV) strategy enables near-constant-pressure shock tube test conditions for reactive experiments behind reflected shocks, thereby enabling improved modeling of the reactive flow field. Here we provide details of the design and operation of the new shock tube. In addition, we detail special buffer gas tailoring procedures, analyze the buffer/test gas interactions that occur on gate valve opening, and outline the size range of fuels that can be studied using the CRV technique in this facility. Finally, we present example low-temperature ignition delay time data to illustrate the CRV shock tube's performance.

Distribution Statement: 1-Approved for public release; distribution is unlimited.

Acknowledged Federal Support:

RPPR Final Report as of 12-Oct-2017

Publication Type: Journal Article Peer Reviewed: Y **Publication Status:** 1-Published
Journal: Combustion and Flame
Publication Identifier Type: DOI **Publication Identifier:** 10.1016/j.combustflame.2013.06.028
Volume: 161 **Issue:** 3 **First Page #:** 634
Date Submitted: **Date Published:**
Publication Location:

Article Title: 1-Butanol ignition delay times at low temperatures: An application of the constrained-reaction-volume strategy

Authors:

Keywords: Ignition delay, Pre-ignition, 1-Butanol, Constant pressure, shock tube

Abstract: Ignition delay times behind reflected shock waves are strongly sensitive to variations in temperature and pressure, yet most current models of reaction kinetics do not properly account for the variations that are often present in shock tube experiments. Particularly at low reaction temperatures with relatively long ignition delay times, substantial increases in pressure and temperature can occur behind the reflected shock even before the main ignition event, and these changes in thermodynamic conditions of the ignition process have proved difficult to interpret and model. To obviate such pressure increases, we applied a new driven-gas loading method that constrains the volume of reactive gases, thereby producing near constant-pressure test conditions for reflected shock measurements. Using both conventional operation and this new constrained-reaction-volume (CRV) method, we have collected ignition delay times for 1-butanol/O₂/N₂ mixtures over temperatures between 716 and 1121 K and no

Distribution Statement: 1-Approved for public release; distribution is unlimited.

Acknowledged Federal Support:

Publication Type: Journal Article Peer Reviewed: Y **Publication Status:** 1-Published
Journal: Combustion and Flame
Publication Identifier Type: DOI **Publication Identifier:** 10.1016/j.combustflame.2013.09.005
Volume: 161 **Issue:** 2 **First Page #:** 371
Date Submitted: **Date Published:**
Publication Location:

Article Title: Pyrolysis and oxidation of decalin at elevated pressures: A shock-tube study

Authors:

Keywords: shock tube, Ignition delay, Laser absorption, Pyrolysis, Decalin, Ethylene

Abstract: Ignition delay times and ethylene concentration time-histories were measured behind reflected shock waves during decalin oxidation and pyrolysis. Ignition delay measurements were conducted for gasphase decalin/air mixtures over temperatures of 769–1202 K, pressures of 11.7–51.2 atm, and equivalence ratios of 0.5, 1.0, and 2.0. Negative-temperature-coefficient (NTC) behavior of decalin autoignition was observed, for the first time, at temperatures below 920 K. Current ignition delay data are in good agreement with past shock tube data in terms of pressure dependence but not equivalence ratio dependence. Ethylene mole fraction and fuel absorbance time-histories were acquired using laser absorption at 10.6 and 3.39 μ m during decalin pyrolysis for mixtures of 2200–3586 ppm decalin/argon at pressures of 18.2–20.2 atm and temperatures of 1197–1511 K. Detailed comparisons of these ignition delay and species time-history data with predictions based on currently available decalin reaction mecha

Distribution Statement: 1-Approved for public release; distribution is unlimited.

Acknowledged Federal Support:

WEBSITES:

RPPR Final Report as of 12-Oct-2017

URL: <http://purl.stanford.edu/kb621cw6967>

Date Received: 30-Aug-2016

Title: Davidson, David F. and Hanson, Ronald K. (2016). Fundamental Kinetics Database Utilizing Shock Tube Measurements. Stanford Digital Repository. Available at: <http://purl.stanford.edu/kb621cw6967>

Description: The Fundamental Kinetic Database Utilizing Shock Tube Measurements Database summarizes the published shock tube experimental work performed under the supervision of Prof. Ronald K. Hanson of the Mechanical Engineering Department at Stanford University. The database covers the years from 1974 to 2013 inclusively. The database is divided into three types of data: ignition delay times, species time-history measurements, and reaction rate measurements. Volumes are in DOCX format and data tables in the volumes can be easily cut and pasted into separate user spread sheets.

URL: <http://purl.stanford.edu/kb621cw6967>

Date Received: 30-Aug-2016

Title: Davidson, David F. and Hanson, Ronald K. (2016). Fundamental Kinetics Database Utilizing Shock Tube Measurements. Stanford Digital Repository. Available at: <http://purl.stanford.edu/kb621cw6967>

Description: The Fundamental Kinetic Database Utilizing Shock Tube Measurements Database summarizes the published shock tube experimental work performed under the supervision of Prof. Ronald K. Hanson of the Mechanical Engineering Department at Stanford University. The database covers the years from 1974 to 2013 inclusively. The database is divided into three types of data: ignition delay times, species time-history measurements, and reaction rate measurements. Volumes are in DOCX format and data tables in the volumes can be easily cut and pasted into separate user spread sheets.

Final Report

ARO Contract # W911NF1310206

Studies of ARO-Relevant Fuels using Shock tube/Laser Absorption Methods

R. K. Hanson

Mechanical Engineering Department

Stanford University, Stanford CA, 94121

Dr. Ralph Anthenien, Contract Monitor

August 19, 2017

Executive Summary

Validation and refinement of reaction mechanisms and development of new and improved reduced mechanisms describing the pyrolysis, oxidation and ignition of practical fuels requires a reliable database of experimental combustion targets. This database must cover relevant combustion conditions and encompass realistic practical fuels, fuel surrogate mixtures and individual surrogate components. Shock tubes and laser absorption diagnostics are able to provide three important types of experimental measurements for this database: ignition delay times, species concentration time-histories and elementary reaction rate constants. These experimental methods are the mainstay of this ARO research program at Stanford.

The primary scientific problem that this research addresses is the need for a very high-quality experimental database with which to test and refine detailed reaction mechanisms for jet and diesel fuel surrogates. Over the past several years, we have made several advances in shock tube and laser absorption methodology that we believe are strongly supportive of the desired rapid advancement of fuel research in this area.

Research was performed in three main areas: improvements to shock tube performance, ignition delay times and species time-histories, and high-speed end-wall imaging. A full list of all publications that acknowledge support from this contract is attached to this report. Summary overviews of each area follow and have been adapted from the key paper abstracts. These papers have been included in this final report.

Improvements to shock tube performance

Several techniques have been developed for obtaining long, constant-pressure test times in reflected shock wave experiments in a shock tube, including the use of driver inserts, driver gas tailoring, helium gas diaphragm interfaces, driver extensions, and staged driver gas filling. These techniques were explored under this research program including the most recent strategy, staged driver gas filling. Experiments indicate that this staged filling strategy increases available test time by roughly 20 % relative to single-stage filling of tailored driver gas mixtures, while simultaneously reducing the helium required per shock by up to 85 %. Using this staged driver gas filling, in addition to the other techniques listed above, post-reflected shock test times of up to 0.102 s (102 ms) at 524 K and 1.6 atm have been obtained. Spectroscopically based temperature measurements in non-reactive mixtures have confirmed that temperature and pressure conditions remain constant throughout the length of these long test duration trials. Finally, these strategies have been used to measure low-temperature *n*-heptane ignition delay times. (Campbell et al. 2017).

Ignition delay times and species time-histories

Ignition delay times were measured behind reflected shock waves in a shock tube for a wide variety of distillate and single component fuels over a range of temperatures, pressures and mixtures. The fuels studied include: jet fuels (JP-5, JP-8, and Jet A), rocket propellants (RP-2), diesel fuels (F-76 and DF-2) and gasoline. A simple correlation was found to describe the ignition delay times for all these fuel/air experiments for equivalence ratios near unity, temperatures from 1000 to 1400 K, and pressures from 6 to 60 atm. A simple correlation was also found for low-fuel-concentration experiments diluted in argon. Previously published

ignition delay time data were found to be in good agreement with these correlations. For several fuels studied, systematic variations were seen in the activation energy for ignition delay time measurements with varying equivalence ratio and oxygen concentration. (Davidson et al. 2017).

Ignition delay times of normal heptane have been measured at temperatures ranging from 651 to 823 K and at pressures between 6.1 and 7.4 atm at an equivalence ratio of 0.75 in 15%O₂/5%CO₂/Ar and in 15%O₂/Ar mixtures behind reflected shock waves in a shock tube. Time-history measurements of fuel, OH, aldehydes (mostly CH₂O), CO₂, H₂O, and temperature were also measured under these conditions. These time-histories provide critically needed kinetic targets to test and refine detailed reaction mechanisms. Measurements were acquired using a novel constrained reaction volume approach, wherein a sliding gate valve confined the reactant mixture to a region near the end-wall of the shock tube. A staged-driver gas filling strategy, combined with driver section extensions, driver inserts, and driver gas tailoring, was used to obtain constant-pressure test times of up to 55 ms, allowing observations of the chemistry in the Negative Temperature Coefficient (NTC) region. Experiments with conventional shock tube filling were also performed, showing similar overall ignition behavior. Comparisons between current data and simulations using the Mehl et al. *n*-Heptane mechanism (2011) are provided, revealing that the mechanism generally under-predicts first-stage ignition delay times in the NTC region, and that at low temperatures it over-predicts the extent of fuel decomposition during first stage ignition. (Campbell et al. 2015).

High-speed endwall imaging

A high-speed OH* chemiluminescence imaging diagnostic was developed to image the structure and homogeneity of combustion events behind reflected shock waves in the Stanford Constrained Reaction Volume Shock Tube. An intensified high-repetition-rate imaging system was used to acquire images of OH* chemiluminescence (near 308 nm) through a fused quartz shock tube end-wall window at 10–33 kHz during the combustion of *n*-heptane (21 % O₂/Ar, E.R.= 0.5). In general, the imaging technique enabled observation of the main ignition event in the core of the shock tube that corresponded to typical markers of ignition (e.g., pressure rise), as well as localized ignition near the wall that preceded the main core ignition event for some conditions. Case studies were performed to illustrate the utility of this novel imaging diagnostic. First, by comparing localized wall ignition events to the core ignition event, the temperature homogeneity of the post-reflected shock gas near the end-wall was estimated to be within 0.5 % for the test condition presented ($T = 1159\text{K}$, $P = 0.25\text{MPa}$). Second, the effect of a recession in the shock tube wall, created by an observation window, on the combustion event was visualized. Localized ignition was observed near the window, but this disturbance did not propagate to the core of the shock tube before the main ignition event. Third, the effect of shock tube cleanliness was investigated by conducting tests in which the shock tube was not cleaned for multiple consecutive runs. For tests after no cleaning was performed, ignition events were concentrated in the lower half of the shock tube. In contrast, when the shock tube was cleaned, the ignition event was distributed around the entire circumference of the shock tube; validating the cleaning procedure. (Troutman et al. 2016).

Archival Publications Supported by this Contract

Shock Tube Performance

M. F. Campbell, K. G. Owen, D. F. Davidson, R. K. Hanson, "Dependence of Calculated Post-Shock Thermodynamic variables on Vibrational Equilibrium and Input Uncertainty," *Journal of Thermophysics and Heat Transfer* 31 Issue 3, January 2017, DOI: [10.2514/1.T4952](https://doi.org/10.2514/1.T4952)

M.F. Campbell, D.R. Haylett, D.F. Davidson and R.K. Hanson, "AEROFROSH: A Shock Condition Calculator for Multi-component Fuel Aerosol-laden Flows," *Shock Waves* (2015) DOI [10.1007/s00193-015-0582-3](https://doi.org/10.1007/s00193-015-0582-3)

M.F. Campbell, T. Parise, A.M. Tulgestke, R.M. Spearrin, D.F. Davidson and R.K. Hanson, "Strategies for Obtaining Long Constant-Pressure Test Times in Shock Tubes," *Shock Waves*, DOI [10.1007/s00193-015-0596-x](https://doi.org/10.1007/s00193-015-0596-x)

M.F. Campbell, A.M. Tulgestke, D.F. Davidson and R.K. Hanson, "A Second-generation Constrained Reaction Volume Shock Tube," *Rev. Sci. Inst.* 85 055108 (2014) DOI [10.1063/1.4875056](https://doi.org/10.1063/1.4875056)

Ignition Delay Times and Species Time Histories

D.F. Davidson, Y.Y. Zhu, J. Shao and R.K. Hanson, "Ignition Delay Times of Distillate Fuels," *Fuel* 187 (2017) 26-32 DOI: [10.1016/j.fuel.2016.09.047](https://doi.org/10.1016/j.fuel.2016.09.047)

M.F. Campbell, D.F. Davidson and R.K. Hanson, "Scaling Relation for High-Temperature Biodiesel Surrogate Ignition Delay Times," *Fuel* **164** 151–159 (2016) [10.1016/j.fuel.2015.09.078](https://doi.org/10.1016/j.fuel.2015.09.078)

M. F. Campbell, D. F. Davidson, R. K. Hanson, "Ignition Delay Times of Very-Low-Vapor-Pressure Biodiesel Surrogates behind Reflected Shock Waves," *Fuel* 136 (2014) 271-281 DOI [10.1016/j.fuel.2014.02.050](https://doi.org/10.1016/j.fuel.2014.02.050)

M.F. Campbell, S. Wang, C. S. Goldenstein, R. M. Spearrin, A. M. Tugestke, L. T. Zaczek, D. F. Davidson, R. K. Hanson, "Constrained Reaction Volume Shock Tube Study of n-Heptane Oxidation: Ignition Delay Times and Time-Histories of Multiple Species and Temperature," *Proceedings of the Combustion Institute* 35 (2015) 231-239, DOI [10.1016/j.proci.2014.05.001](https://doi.org/10.1016/j.proci.2014.05.001)

I. L. R. Bec, Y. Zhu, D. F. Davidson, R. K. Hanson, "Shock Tube Measurements of Ignition Delay Times for the Butanol Isomers Using the Constrained-Reaction-Volume Strategy," *International Journal of Chemical Kinetics* 46 (2014) 433-442.

Y. Zhu, D. F. Davidson, R. K. Hanson, "Pyrolysis and oxidation of decalin at elevated pressures: a shock tube study," *Combustion and Flame* 161 (2014) 371-383.

Y. Zhu, D. F. Davidson, R. K. Hanson, "1-Butanol Ignition Delay Times at Low Temperatures: An Application of the Constrained-Reaction-Volume Strategy," *Combustion and Flame* 161 (2014) 634-643.

A.M. Ferris, D.F. Davidson and R.K. Hanson, "Combined Laser Absorption and Gas Chromatography (GC) Speciation in a Shock Tube: Validation and Application to Ethylene Pyrolysis," Paper, 10th U.S. National Combustion Meeting, April 2017.

High-Speed Endwall Imaging

V.A. Troutman, C.L. Strand, M.F. Campbell, A.M. Tulgestke, V.A. Miller, D.F. Davidson, R.K. Hanson, "High-speed OH* Chemiluminescence Imaging of Ignition through a shock Tube End Wall," Applied Physics B (2016) 122:56 DOI: [10.1007/s00340-016-6326-y](https://doi.org/10.1007/s00340-016-6326-y). .

D.F. Davidson, A.M. Tulgestke, and R.K. Hanson, "High-speed Imaging of Ignition behind Reflected Shock Waves," AIAA Science and Technology Meeting San Diego, January 2016 , [DOI 10.2514/6.2016-0188](https://doi.org/10.2514/6.2016-0188).

D. F. Davidson, A. Tulgestke, C. Strand, M. F. Campbell, S.Wang, R. K. Hanson, "Rapid Chemiluminescent Imaging behind Reflected Shock Waves," 30th International Symposium on Shock Waves, Paper 180, Tel Aviv Israel, July 20-24 2015.

A.M. Tulgestke, S. Johnson, D.F. Davidson and R.K. Hanson, "High-Speed Imaging of Inhomogeneous Ignition in a Shock Tube," 26th ICDERS, Boston, Massachusetts, July 2017.


Review papers

R. K. Hanson, D. F. Davidson, "Advances in Shock Tube Techniques for Fundamental Studies of Combustion Kinetics," 25th International Colloquium on the Dynamics of Explosions and Reactive Systems, Paper 260, Leeds United Kingdom, August 2-7 2015.

R.K. Hanson and D.F. Davidson, "Chemical Kinetics and Chemical Reacting Flows," invited paper, ISSW30/Tel Aviv (July 2015).

R. K. Hanson, D. F. Davidson, "Chemical Kinetics and Chemical Reacting Flows," 30th International Symposium on Shock Waves, Plenary Paper, Tel Aviv Israel, July 20-24 2015.

Strategies for obtaining long constant-pressure test times in shock tubes

M. F. Campbell¹  · T. Parise² · A. M. Tulgestke² · R. M. Spearrin² ·
D. F. Davidson² · R. K. Hanson²

Received: 18 March 2014 / Revised: 13 May 2015 / Accepted: 20 August 2015 / Published online: 22 September 2015
© Springer-Verlag Berlin Heidelberg 2015

Abstract Several techniques have been developed for obtaining long, constant-pressure test times in reflected shock wave experiments in a shock tube, including the use of driver inserts, driver gas tailoring, helium gas diaphragm interfaces, driver extensions, and staged driver gas filling. These techniques are detailed here, including discussion on the most recent strategy, staged driver gas filling. Experiments indicate that this staged filling strategy increases available test time by roughly 20 % relative to single-stage filling of tailored driver gas mixtures, while simultaneously reducing the helium required per shock by up to 85 %. This filling scheme involves firstly mixing a tailored helium–nitrogen mixture in the driver section as in conventional driver filling and, secondly, backfilling a low-speed-of-sound gas such as nitrogen or carbon dioxide from a port close to the end cap of the driver section. Using this staged driver gas filling, in addition to the other techniques listed above, post-reflected shock test times of up to 0.102 s (102 ms) at 524 K and 1.6 atm have been obtained. Spectroscopically based temperature measurements in non-reactive mixtures have confirmed that temperature and pressure conditions remain constant throughout the length of these long test duration

trials. Finally, these strategies have been used to measure low-temperature *n*-heptane ignition delay times.

Keywords Long test time · Driver insert · Driver gas tailoring · Staged driver gas filling · Reflected shock · Shock tube

1 Introduction

1.1 Motivation

The use of shock tubes for studies of combustion chemical kinetics has enabled the precise determination of reaction rates, the measurement of ignition delay times, and studies of other combustion phenomena for the past 60 years. To date, most of these studies have employed test times less than about 15 ms (e.g., [1,2]) and often times less than 2 ms. Although this short duration has been sufficient to examine the chemistry of hydrocarbon fuels of practical significance at elevated temperatures (>900 K) and high pressures, recent interest in low-temperature combustion at practical engine conditions (between 600 and 900 K at moderate-to-high pressures and a range of equivalence ratios), which is characterized by much longer timescales, has created a need for greater test times in shock tubes.

1.2 Previous research

Several researchers have contributed to the extension of shock tube test times. For instance, Amadio et al. [3] and Hong et al. [4] developed driver gas tailoring relationships for use with low-sound-speed gases and convergent shock tubes, respectively. Additionally, Dumitrescu [5], Stotz et al. [6], and Hong et al. [7] modified the geometry of the driver section

Communicated by B. Skews and A. Higgins.

✉ M. F. Campbell
mfcampb@sandia.gov
<http://crf.sandia.gov/>

R. K. Hanson
<http://hanson.stanford.edu/>

- ¹ Combustion Research Facility, Sandia National Laboratory, Livermore, CA 94551, USA
- ² Department of Mechanical Engineering, Stanford University, Stanford, CA 94305, USA

to achieve either non-attenuating incident shock waves or to mitigate pressure increases in the post-reflected shock region. Rossmann et al. [8] developed a shock tunnel with a plunger in the driver section, which allowed the driver section length to be modified to reduce high-pressure helium use. However, this helium consumption reduction came at the expense of a decrease in test time as well. Similarly, Pang et al. [9], Lam et al. [10], and Gates et al. [11] used driver section extensions together with driver gas tailoring to achieve test times approaching 20, 25, and 45 ms, respectively (see also Ref. [12]). Hanson et al. [13], Zhu et al. [14], and Campbell et al. [15] demonstrated a constrained reaction volume approach to confine the reactive gas volume to an area very close to the endwall of the shock tube, reducing the adverse effects of reactions occurring far from the test location at long test times. Also, Campbell et al. [15] used a staged driver gas-filling approach, in combination with the other techniques listed above, to achieve test times as long as 55 ms.

Several groups have studied shock propagation phenomena numerically or theoretically. Hooker [16] and Polachek and Seeger [17] examined shock interactions at gas interfaces; their work led to better understanding of driver/driven gas mixing and the need for a lightweight interface gas (i.e., helium) near the shock tube diaphragm [4]. Frazier et al. [18] numerically examined the effects of heat transfer on post-reflected shock average gas temperature and concluded that heat transfer did not significantly reduce area-averaged temperature for test times up to (and longer than) 20 ms in 8-cm-diameter or larger shock tubes. Jacobs developed a quasi-one-dimensional Lagrangian code for the simulation of transient flow facilities such as free piston-driven shock tunnels [19]. Also, a second-order, MUSCL–Hancock method finite volume code with an exact Riemann solver has been developed by the University of Wisconsin Shock Tube Lab (WiSTL) [20]. This code is able to generate $x-t$ diagrams, which graphically depict wave propagation in shock tubes and help predict test time. Finally, Rossmann et al. developed an empirically informed computer routine capable of generating $x-t$ diagrams [8]. The routine used experimental incident shock attenuation data to better model the incident shock trajectory and also accounted for the acceleration of the contact surface due to boundary layer growth.

1.3 Background

A pressure-driven shock tube consists of two parts: the driver section, filled with high-pressure driver gas (often helium), separated by a thin polycarbonate or metal diaphragm from the driven section, which contains a low-pressure driven gas (often argon, although many shock tube studies, especially those studying fuel ignition, use nitrogen dilution). The experiment commences when the diaphragm bursts due to pressure-induced strain, and an incident shock wave prop-

agates in the driven section toward the shock tube endwall, located at the end of the driven section. As it moves, the shock wave heats and compresses the gas, setting it in motion in the direction of the incident shock. When the incident shock reaches the endwall, it reflects back toward the driver section, further compressing and heating the driven gas and also stagnating the flow. The arrival of the reflected shock at the test location (typically 1–2 cm from the endwall) marks the beginning of the test time. Meanwhile, an expansion wave moves in the driver section away from the burst diaphragm toward the driver section's end cap. After reaching the driver section end cap, this wave is reflected and moves toward the driven section endwall. When the expansion wave arrives at the test location, it causes a decrease in pressure, ending the test time.

An $x-t$ diagram can be used to clarify the various interactions between the waves introduced above, as shown in Fig. 1. On this plot, the use of straight lines implies that ideal shock tube behavior is assumed (i.e., shock and expansion wave velocity attenuation is neglected); this results in a slight underprediction of test time. The black line represents the incident and reflected shock waves, the blue and purple lines denote the expansion head and tail waves, respectively, and the red line represents the contact surface between the driver and driven gases. In this figure, the dimensions shown represent those of the shock tube used in this study, with its shortest driver section. This shock tube has a driven section length of $L_{\text{driven}} = 9.73$ m and a driver length of $L_{\text{driver}} = 3.63$ m. The test time shown in this figure is denoted τ . Several areas in this figure are denoted with numbers, which correspond to different regions in space–time during the shock experi-

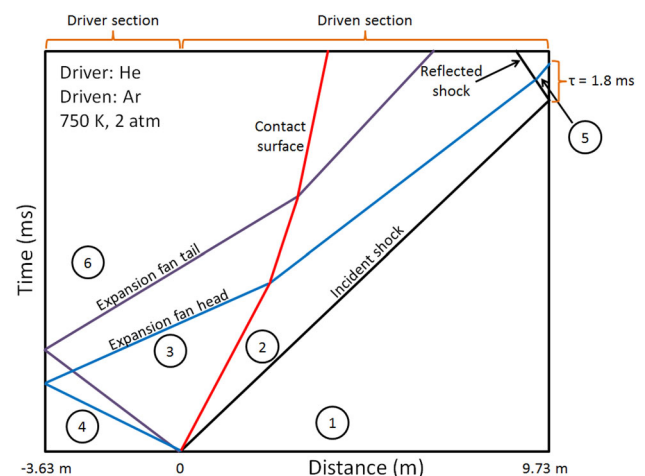


Fig. 1 Idealized $x-t$ diagram for a basic shock tube experiment, generated based on the WiSTL code [20] with thermodynamic data taken from Ref. [21]. Conditions: $M_{\text{IS}} = 1.68$ (incident shock Mach number), $T_1 = T_4 = 22$ C, $P_4 = 1.2$ atm, $P_1 = 179$ Torr, $P_5 = 2.0$ atm, $T_5 = 750$ K, $A_{\text{driver}} = A_{\text{driven}}$ (identical driver and driven cross-sectional areas). Driver 100 % He; driven 100 % Ar

ment. The initial, undisturbed driven section is termed Region 1, and that in the driver section is termed Region 4. Likewise, the interval behind the incident shock wave bounded first by the contact surface and then by the expansion wave head is Region 2. The region behind the reflected shock is Region 5. Finally, Region 3 denotes the conditions in the driver gas between the contact surface and the expansion fan, and Region 6 refers to the driver gas conditions following the reflected expansion wave.

When test times longer than a few milliseconds are attempted, a new phenomenon occurs wherein the reflected shock interacts with the contact surface, sending either a shock or an expansion wave back to the test location. This causes either a pressure increase (shock wave) or a pressure drop (expansion wave). Both of these conditions are undesirable and result in the termination of the test time (for detailed $x-t$ diagrams of these cases, see Figs. 3 and 4 of Ref. [3]). To counteract this contact surface interaction, driver gas tailoring, made possible by blending a lower-sound-speed gas such as nitrogen, argon, carbon dioxide, or propane with helium, is used such that the pressures on both sides of the contact surface, following the passage of the reflected shock, are identical. This stagnates the contact surface and as a result no wave is reflected back to the test section (see Refs. [3, 4, 22]). Ultimately, the test time is ended by the arrival of the expansion wave, reflected from the driver section end cap, at the test location.

An idealized $x-t$ diagram showing a shock experiment at the tailored condition is shown in Fig. 2. Region 8 refers to the time behind the reflected shock, bounded by the expansion wave head. Notice that the contact surface is motionless (vertical red line between Regions 5 and 8) after interact-

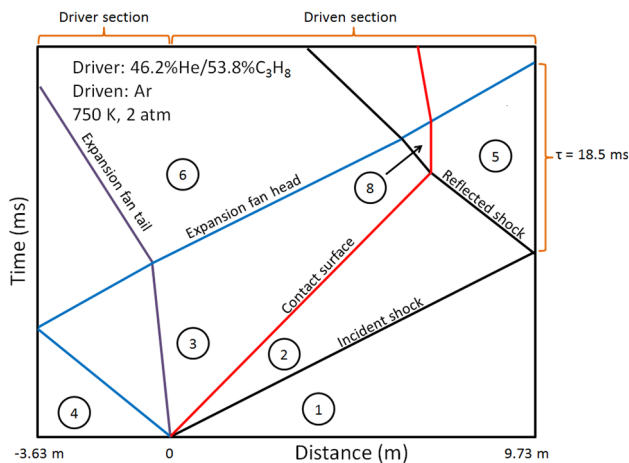


Fig. 2 Idealized $x-t$ diagram for a tailored shock tube experiment, generated based on the WiSTL code [20] with thermodynamic data taken from Ref. [21] and driver gas tailoring generated using the methodology of Amadio et al. [3]. Conditions: $M_{IS} = 1.68$, $T_1 = T_4 = 22$ C, $P_4 = 2.0$ atm, $P_1 = 179$ Torr, $P_5 = 2.0$ atm, $T_5 = 750$ K, $A_{\text{driver}} = A_{\text{driven}}$. Driver 46.2 % He/53.8 % C_3H_8 ; driven 100 % Ar

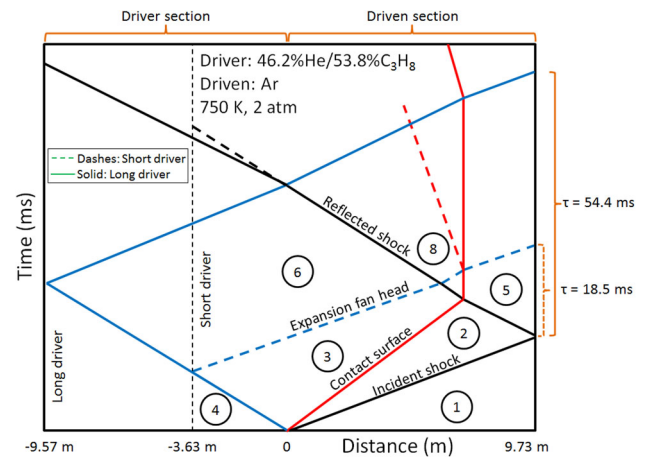


Fig. 3 Idealized $x-t$ diagram comparing two driver lengths (3.63 and 9.57 m), generated based on the WiSTL code [20] with thermodynamic data taken from Ref. [21] and driver gas tailoring generated using the methodology of Amadio et al. [3]. The conditions are identical to those in Fig. 2

ing with the reflected shock wave, but before encountering the expansion wave head. Also, the test time in this case is almost ten times longer than in the untailored example. In this figure, a driver mixture of helium and propane (see Ref. [3]) was chosen to enlarge the area of Region 8 at the given temperature, making the plot easier to read (tailoring is also possible using helium/nitrogen at this temperature, although this results in a smaller Region 8 area).

An $x-t$ diagram can also be used to predict test time as a function of the length of a shock tube's driver section. For instance, consider Fig. 3, an idealized $x-t$ plot showing two different driver section lengths (3.63 and 9.57 m, representing two driver lengths available for the shock tube in this study). As evident, expanding the driver section length increases test time.

Now consider a fictitious shock tube whose total length, driven plus driver, is 20 m. Using an idealized $x-t$ diagram allows the test time of such a shock tube to be easily estimated as a function of the driver length. We have developed an in-house computer algorithm for this purpose that relies on ideal shock relations taken from Refs. [3, 22]. Similar to the code developed by Rossmann et al. [8], this routine employs several simplifications that cause its test time predictions to deviate slightly from the experiments. Despite this shortcoming, we introduce it here because it is a useful tool for both understanding trends observed in experiments and for aiding shock tube design. Figure 4 shows, at one particular test pressure and three test temperatures, the effect of increasing the driver length, while decreasing the driven length to keep the total shock tube length constant. Notice that increasing the driver length, rather than driven length, results in the longest test time at all Region 5 temperatures (T_5) shown. This figure also provides values predicted by the WiSTL code [20]. The

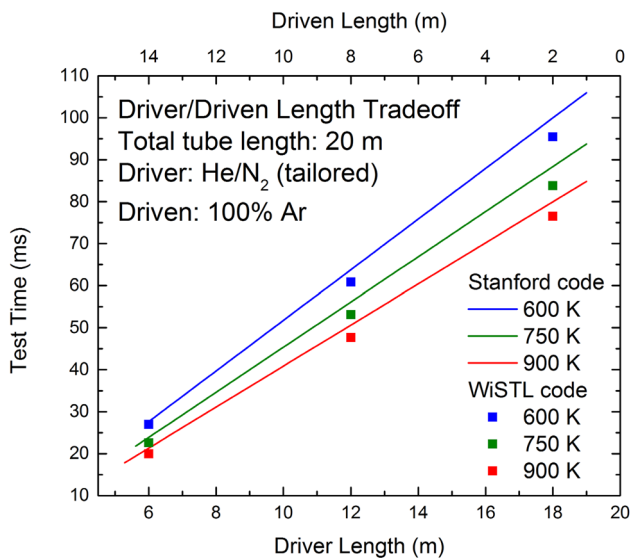


Fig. 4 Approximate shock tube test time τ at the tailored condition [3] as a function of driver section length, for a total shock tube length of 20 m. Lines are computations by the Stanford code, and individual points are values obtained using the WiSTL code [20], with thermodynamic data taken from Ref. [21]. The positively sloped lines indicate that increasing driver section length is more effective at increasing test time than increasing driven section length. As discussed in Amadio et al. [3], tailoring is not possible at the shortest driver lengths at some low temperatures. Conditions: $T_1 = T_4 = 22$ C, $P_5 = 2.0$ atm, $A_{\text{driver}} = A_{\text{driven}}$. Driver He/N₂ (tailored); driven 100 % Ar

values of both programs are in good agreement, although the simple assumption in the current Stanford calculations that the expansion wave velocity remains constant results in a longer test time prediction. It is also important to note that both the WiSTL and Stanford codes assume a driver-to-driven section area ratio of $\frac{A_{\text{driver}}}{A_{\text{driven}}} = 1$. As a consequence, these codes predict a driver gas helium mole fraction that is higher than that necessary in the Stanford tube, which has a convergent driver-driven design with $\frac{A_{\text{driver}}}{A_{\text{driven}}} = 2.38$ [4, 23] (see dimensions in Sect. 2). This results in higher driver gas sound speeds and corresponds to an underprediction of test time relative to times observed in the Stanford facility (the sound speeds and other properties of several gases at 20 C are provided in Table 1).

Plots can also be generated to estimate the available test time as a function of Region 5 temperature T_5 , for different driver section lengths and a fixed driven section length. This is shown in Fig. 5. Note again the good agreement between the WiSTL code's predictions and those of the Stanford code. As temperature increases, available test time decreases, because at the tailored condition more helium is required in the driver gas, thereby increasing the speed of the expansion wave head. Conveniently, above about 900 K, the timescale for kinetic processes generally decreases with temperature as well. This implies that a shock tube with sufficient driver length operating at the tailored condition is able to observe

kinetic processes over a very large range of temperatures. Plots such as Fig. 5 are useful in determining the driver length necessary to obtain the required test time.

In the High Temperature Gasdynamics Laboratory at Stanford University, we have developed numerous techniques for extending the test time in shock tubes, including driver inserts [7], driver gas tailoring [4], the use of helium interface gas in front of the diaphragm [4], driver extensions [9–11], and staged driver gas filling [15]. Our goal in this work is to use these tools sequentially to achieve and even exceed the test time predictions offered by the $x - t$ diagrams shown above.

2 Experimental setup

As introduced above, the shock tube employed in this study was initially composed of a 9.73-m driven section with a round internal diameter of 11.5 cm, and a driver section composed of a 3.63-m driver section with a round internal diameter of 17.8 cm. Using driver extensions, which had internal diameters of 15.4 cm, the driver section length was extendable to a maximum of 13.42 m. The driver and driven sections were separated by a polycarbonate diaphragm with a thickness of 0.25 mm, and a four-blade cutter was used to decrease shock-to-shock variation in burst pressure and minimize the occurrence of diaphragm fragments released in the tube. Driver inserts, discussed later in this article, were constructed according to the methodology of Hong et al. [7] to counteract the non-ideal pressure rise in the test section associated with boundary layer formation and shock attenuation.

Diagnostics were located 2 cm away from the endwall of the driven section. Sidewall pressures were monitored using a Kistler 603B1 transducer covered in room temperature vulcanizing silicone (RTV) mounted at this location, and shock speeds were measured using the time-of-arrival technique via a series of seven PCB 113A26 transducers (with a 483B08 amplifier) and extrapolated to the endwall with an accuracy of better than ± 0.2 %. Data from these instruments were recorded using a LabVIEW data acquisition system with a measurement rate of 10 MHz. Note that test times measured at the 2-cm location (as in these experiments) and on the endwall (as in the simulations performed in this study) are essentially identical. The temperature and pressure at the endwall behind the incident and reflected shocks were computed using 1-D shock relations (for instance, see Ref. [24]) to an accuracy of better than ± 0.6 and ± 1.6 %, respectively, using thermodynamic data taken from the Burcat database [21].

Prior to each experiment, the driven section was mechanically pumped to a pressure of less than 0.1 Torr, and the driver section was rough pumped to a pressure of less than 1 Torr. Research-grade argon, helium, nitrogen, propane, and carbon dioxide were obtained from Praxair Inc. Spectroscopic-grade normal heptane, used in ignition experiments, was obtained

Table 1 Properties of several gases at 20 °C using data obtained from the Burcat database [21]

Species	Molecular weight (g/mol)	$\gamma = \frac{c_p}{c_v}$ (20 °C)	Gas constant (J/kg K)	Sound speed (20 °C) (m/s)	Category
H ₂	2.02	1.41	4124.5	1303.8	Diatomic
He	4.00	1.67	2077.3	1007.4	Noble gas
Ne	20.18	1.67	412.0	448.7	Noble gas
CH ₄	16.04	1.31	518.3	445.6	Hydrocarbon
H ₂ O	18.02	1.33	461.5	424.1	Triatomic
N ₂	28.01	1.40	296.8	349.0	Diatomic
CO	28.01	1.40	296.8	349.0	Diatomic
NO	30.01	1.39	277.1	335.5	Diatomic
O ₂	32.00	1.40	259.8	326.0	Diatomic
Ar	39.95	1.67	208.1	318.9	Noble gas
C ₂ H ₆	30.07	1.19	276.5	310.7	Hydrocarbon
CO ₂	44.01	1.29	188.9	267.4	Triatomic
C ₃ H ₈	44.10	1.13	188.6	249.8	Hydrocarbon
Kr	83.80	1.67	99.2	220.2	Noble gas
SO ₂	64.06	1.27	129.8	219.4	Triatomic
Xe	131.29	1.67	63.3	175.9	Noble gas
C ₂ HF ₅	120.02	1.10	69.3	149.2	Refrigerant
Rn	222.00	1.67	37.5	135.3	Noble gas
SF ₆	146.06	1.09	56.9	135.2	Insulator
C ₂ Cl ₆	236.74	1.07	35.1	104.7	Refrigerant
C ₄ F ₁₀	238.03	1.05	34.9	103.5	Refrigerant

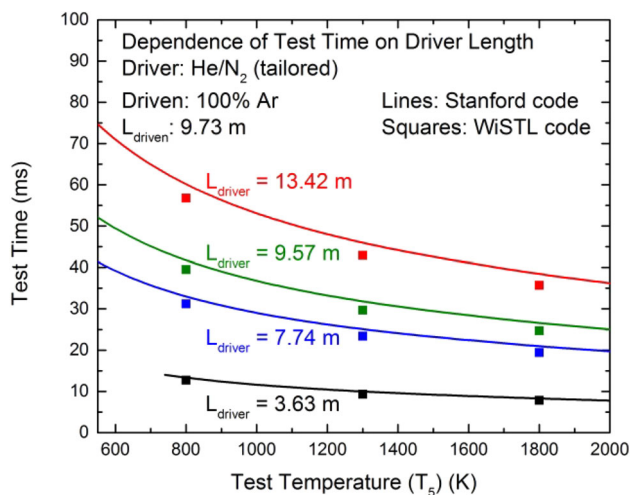


Fig. 5 Shock tube test time τ at the tailored condition [3] as a function of test temperature, for $L_{\text{driver}} = 9.73$ m and several values of L_{driver} (corresponding to available Stanford shock tube driver section configurations). Lines are computations by the Stanford code, and individual points are values obtained using the WiSTL code [20], with thermodynamic data taken from Ref. [21]. As discussed in Amadio et al. [3], tailoring is not possible at the shortest driver length at some low temperatures. Conditions: $T_1 = T_4 = 22$ °C, $P_5 = 2.0$ atm, $A_{\text{driver}} = A_{\text{driven}}$. Driver He/N₂ (tailored); driven 100 % Ar

from Sigma Aldrich and was degassed prior to use. Binary (tailored) driver section mixtures were prepared in the driver section by alternately filling two components (usually in three cycles) and allowing the mixture to settle for at least 2 min prior to bursting the diaphragm; this technique has also been used by other researchers [3]. Due to shock-to-shock variations in filling pressures, the actual driver gas tailoring varied slightly between individual experiments, as the reported values in the plots contained in this article suggest. Finally, to initiate the experiment, the non-helium component (usually nitrogen) was filled until the diaphragm ruptured. Because filling ports in our shock tube are located near the driver section end cap in all driver section configurations, this had the side effect of prolonging test time by pushing the helium-containing mixture toward the diaphragm, much like in the staged driver filling technique described in detail in Sect. 4.

3 Application of existing test time extension techniques

In this section, we will sequentially demonstrate the use of driver inserts [5–7], driver gas tailoring [4], helium interface

gas in front of the diaphragm [4], and driver extensions [9–11] to achieve a long test time with uniform pressure throughout the shock experiment. Details of these individual techniques may be found in greater detail in the referenced papers.

3.1 Driver insert

Pressure profiles from two baseline cases are shown in Fig. 6: one experiment using a driver insert and the other without. In both experiments, the driver gas was 100 % nitrogen and the driven gas was 100 % argon. Also, the driver and driven lengths were 3.63 and 9.73 m, respectively, and the driver-to-driven cross-sectional area ratio was $\frac{A_{\text{driver}}}{A_{\text{driven}}} = 2.38$. At time zero, both pressure records show a step change corresponding to the arrival of the incident and reflected shocks at the 2-cm test location (the resolution of the plot's abscissa is insufficient to differentiate the two shocks). Notice that in the shock taken without the driver insert, a subsequent normalized pressure increase of approximately $\frac{dP^*}{dt} = 1.8 \text{ \%}/\text{ms}$ is observable (the non-uniform increase occurring at about 9 ms in this trace will be discussed later). Pressure increases such as these are highly undesirable, since they isentropically increase the experimental temperature according to (1) [25], with representative values at 1000 K as shown in Fig. 7.

$$T = T_0 \left(\frac{P}{P_0} \right)^{\frac{\gamma-1}{\gamma}}. \quad (1)$$

In this equation, T_0 and P_0 are the initial temperature and pressure in Region 5, and $\gamma = \frac{c_p}{c_v}$ is the temperature-

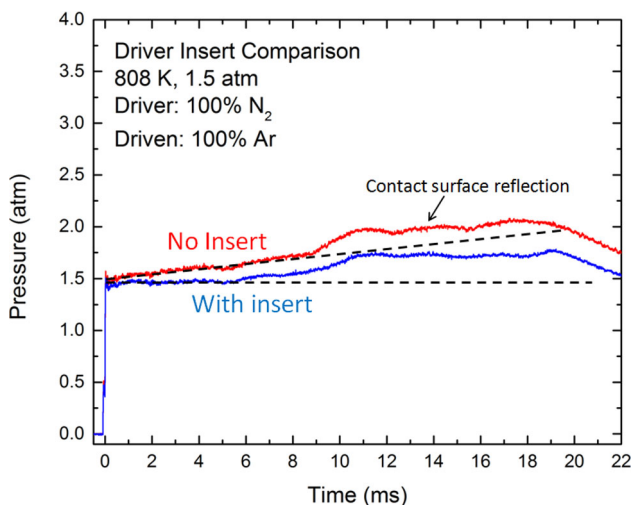


Fig. 6 Comparison of shocks with and without a driver insert. The pressure increase around 9 ms is caused by a driver gas tailoring mismatch. Notice that before and after this increase, the pressure in the presence of the driver insert is constant to within $\pm 5 \text{ \%}$. Conditions: $T_5 = 808 \text{ K}$, $P_5 = 1.5 \text{ atm}$, $\frac{A_{\text{driver}}}{A_{\text{driven}}} = 2.38$, $L_{\text{driver}} = 3.63 \text{ m}$, $L_{\text{driven}} = 9.73 \text{ m}$. Driver 100 % N_2 ; driven 100 % Ar

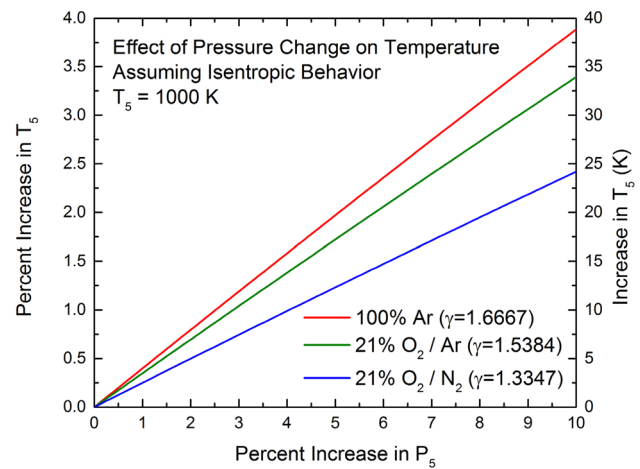


Fig. 7 Percent increase in test temperature for three test gases at a nominal temperature of 1000 K, assuming isentropic behavior according to (1). Gas properties computed using thermodynamic data obtained from Ref. [21]

dependent heat capacity ratio of the driven gas. These pressure increases are caused by factors such as shock attenuation and boundary layer growth behind the incident and reflected shock waves and can be removed by use of a driver insert (see Refs. [5–7]). The driver insert serves to gradually decrease the area of the driver section (as a function of distance) from the diaphragm toward the driver section endwall. This area change prematurely reflects part of the expansion wave back to the test section to counteract the non-ideal pressure increase, resulting in constant post-reflected shock pressure. Thus, in contrast to the record without an insert, the pressure trace with an insert shown in Fig. 6 exhibits a normalized pressure change of $\frac{dP^*}{dt} = 0 \text{ \%}/\text{ms}$ in the time before and after the non-uniform increase (from about 6 to 11 ms in this trace). Finally, the pressure drop in both pressure traces shown near 19 ms represents the arrival of the expansion fan, reflected from the end cap of the driver section, at the 2-cm measurement location.

3.2 Driver gas tailoring

The non-ideal pressure increase seen at a time of about 9 ms in the no-insert pressure trace of Fig. 6 is caused by a driver/driven gas tailoring mismatch. This is the result of the interaction between the contact surface and the reflected shock wave, as discussed in Sect. 1.3. Typically, a pressure increase such as this indicates that the driver gas requires more helium at the given Region 5 temperature (likewise, a pressure decrease indicates a need for a higher mole fraction of the low-sound-speed gas, in this case, nitrogen). Figure 8 compares the untailored shock experiment (driver gas of 100 % N_2) with a tailored experiment, taken using a driver gas of 31 % He/N_2 (the shock tube geometry is identical

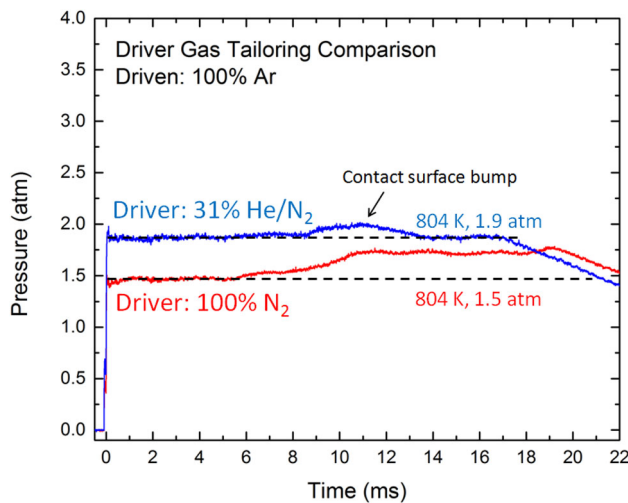


Fig. 8 Result of driver gas tailoring. The 31 % He/N₂ driver gas corresponds to the tailored condition at $T_5 \approx 800$ K in a shock tube which has a driver/driven area ratio $\frac{A_{\text{driver}}}{A_{\text{driven}}} = 2.38$ [4]. Shock tube dimensions are identical to those given in Fig. 6, and a driver insert was used to mitigate non-ideal pressure increases

to that of Fig. 6). At the tailored condition, the pressure in Regions 5 and 8 in the shock tube are matched [3,4,22] (see Fig. 2), such that neither an expansion wave nor a shock wave is transmitted back to the test section. Not surprisingly, a sustained pressure increase is not visible, indicating that the reflected shock wave did not reflect from the driver/driven gas contact surface. However, a pressure hump (contact surface bump) can still be seen near about 10 ms. Finally, the test time at the tailored condition is slightly reduced, indicated by the arrival of the expansion wave at the 2-cm measurement location about 2 ms earlier. This is the result of helium increasing the sound speed of the driver gas, allowing the expansion wave head to move more quickly.

3.3 Helium interface gas

In an ideal shock tube, the contact surface between the driver and driven gases would have zero thickness and no mixing would occur between these fluids. However, for a variety of reasons related to the physics of diaphragm rupture, some driver/driven gas mixing does occur, which results in a contact mixing zone of finite length. The contact surface bump observable in Fig. 8 is the result of the reflected shock interacting with this mixing zone, as described in detail in Refs. [4,16,17]. Use of a lightweight gas such as helium as a buffer between the driver and driven gases greatly reduces the influence of this interaction. In these experiments, helium gas is introduced through a port immediately in front of the diaphragm by first filling the tube with the driven gas mixture (argon) to a pressure very close to the initial pressure (called P_1) and then by filling helium until the pressure is P_1 . Fig-

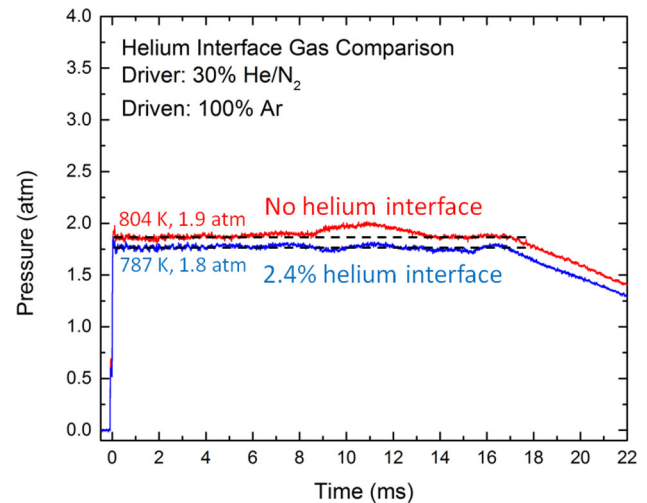


Fig. 9 Effect of helium interface gas. Shock tube geometry is identical to that provided in Fig. 6, and a driver insert was used to mitigate non-ideal pressure increases

ure 9 shows the impact of a helium interface gas which is 2.4 % of P_1 (corresponding to a length in the driven section of about 23 cm) on the contact surface bump. Helium percentages ranging from about 2 to 10 % give the best performance (i.e., elimination of the contact surface bump) in these experiments. Note that other researchers using different shock tubes have reported values as high as 20 % [4]; this large range is likely due to differences in shock tube geometry and diaphragm material (polycarbonate versus metal). Finally, observe that the flat $\frac{dP^*}{dt} = 0$ %/ms test time in the resulting shock is about 16.5 ms.

3.4 Driver extensions

As introduced in Fig. 3, lengthening the driver section can greatly increase test time (see Refs. [9–11]). Figure 10 shows the result of increasing the driver section length from 3.63 to 7.74 m, and then to 9.57 m. True to expectations, increasing driver section length delays the arrival of the expansion wave at the endwall; test time is plotted as a function of length in Fig. 11. Also shown in Fig. 11 are test time predictions made by the Stanford code. Notice that the measured test times are longer than the predicted times, which is likely due to two factors. First, bursting the diaphragm with nitrogen tends to increase test time as discussed in Sect. 2; the model assumed that the entire driver section was filled with the tailored gas mixture. Second, the shock tube employed has a convergent design with $\frac{A_{\text{driver}}}{A_{\text{driven}}} = 2.38$, which allows less driver gas helium to be used as compared to $\frac{A_{\text{driver}}}{A_{\text{driven}}} = 1$ (as assumed by the models) to achieve the same Region 5 temperature, thus decreasing the driver gas sound speed and delaying the arrival of the expansion fan at the test section [4,23].

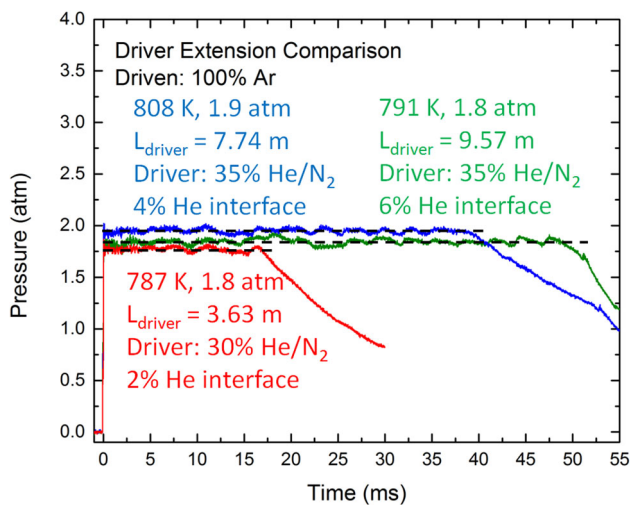


Fig. 10 Comparison of pressure profiles for $\frac{A_{\text{driver}}}{A_{\text{driven}}} = 2.38$, $L_{\text{driven}} = 9.73$ m, with L_{driver} values of 3.63, 7.74, and 9.57 m. The driven gas is 100 % Ar, and the driver gases are tailored He/N₂ mixtures. A driver insert was used to mitigate non-ideal pressure increases

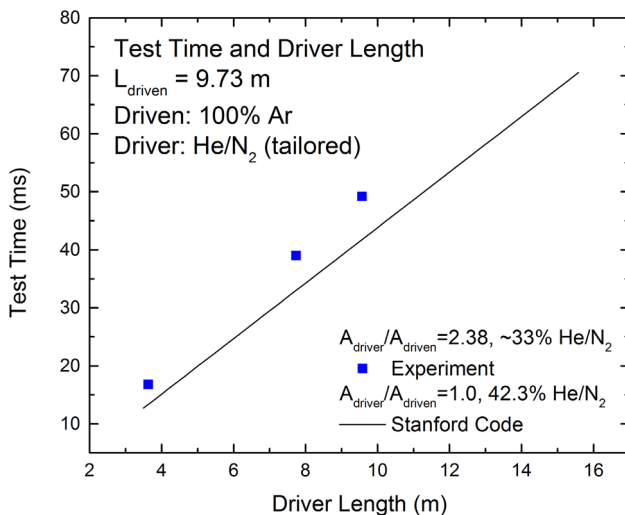


Fig. 11 Test time τ as a function of driver length, for $L_{\text{driven}} = 9.73$ m at $T_5 = 800$ K and $P_5 = 1.9$ atm. The driven gas is 100 % Ar, and the driver gases are tailored He/N₂ mixtures. These experiments employed a driver insert. The line is a computation by the Stanford code using thermodynamic data taken from Ref. [21]

4 Staged driver gas filling

4.1 Theory

Returning to Fig. 2, it is evident that the expansion wave head originates at the diaphragm, propagates toward the driver section end cap, and then is reflected. While undergoing this process, this wave travels at the local sound speed (relative to the gas) of the tailored driver gas mixture [22]. Thus, the use of helium, which has a high sound speed (see Table 1), in the driver gas mixture impedes efforts to achieve long

test times, because it causes the expansion wave to travel more quickly and reach the test section sooner. Moreover, the price of helium has skyrocketed in recent years [26], making it costly to fill the entire driver section (especially once this section is elongated to expand the test time). However, helium is a desirable driver gas because of its propensity to create strong shocks with moderate driver section pressures (the only other alternative considered is hydrogen [27–29], which is not commonly used in the USA because of its explosive potential). To accommodate the need for strong shocks (obtained by having the tailored helium/low-sound-speed gas adjacent to the diaphragm) while achieving the longest possible test time (obtained by filling a majority of the driver section with a low-sound-speed gas), we have developed a staged driver gas-filling technique.

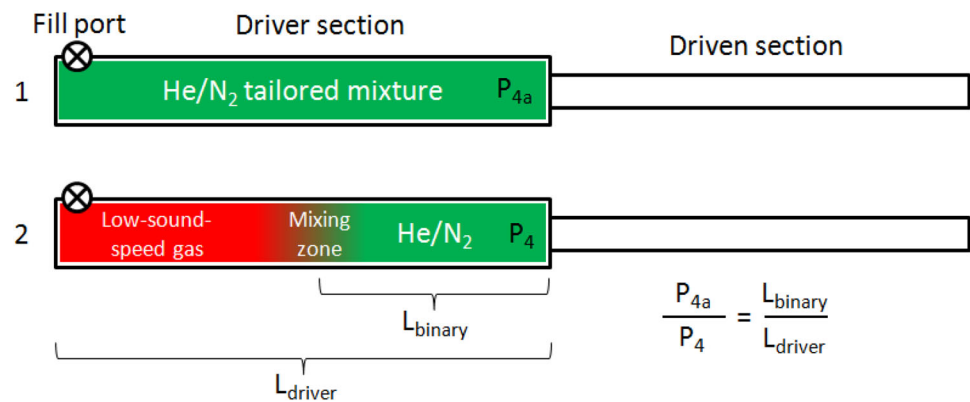
Note that a lower-sound-speed gas (such as nitrogen, krypton, or xenon) in the driven section could also be used to increase test time. However, nitrogen has a finite vibrational relaxation time behind shock waves that can affect data analysis, and krypton and xenon are prohibitively expensive; for these reasons, argon is often the preferred inert driven bath gas for shock tube experiments.

4.2 Technique

In a conventional shock tube experiment that employs driver gas tailoring such as those introduced above, the driver section is filled with a binary mixture, often consisting of helium and nitrogen, until the diaphragm ruptures. The staged filling technique involves one additional step and is performed as follows (see also Fig. 12). First, the driver section is filled to an intermediate pressure P_{4a} as in the conventional filling technique with a tailored binary mixture of helium and nitrogen. Second, the driver section is filled until diaphragm rupture (said to occur at pressure P_4) using a port near the driver section end cap (far from the diaphragm) with a third, low-sound-speed (backfill) gas. As this low-sound-speed gas fills, it pushes the binary mixture toward the diaphragm. A mixing zone also develops between the backfill and binary gases during this process. Thus, the ratio $\frac{P_{4a}}{P_4}$ governs the extent to which the driver section is filled with the binary mixture according to (2) (where L_{binary} is the idealized length of binary gas measured from the diaphragm). Note that this equation ignores the presence of the driver insert, which slightly decreases the driver section area as discussed above. The L_{binary} values provided in this paper do, however, account for the slight change in diameter of our driver section as it changes from 17.8 cm over the first 3.63 m to 15.4 cm over the next 9.79 m (the total maximum driver length is 13.42 m).

$$\frac{P_{4a}}{P_4} = \frac{L_{\text{binary}}}{L_{\text{driver}}} \quad (2)$$

Fig. 12 Staged driver filling procedure [in this case, the tailored (binary) mixture is He/N₂]. The driver section is first filled to pressure P_{4a} with the binary mixture and then filled from a port near the driver end cap with the low-sound-speed gas until diaphragm rupture at pressure P_4



An idealized $x-t$ diagram comparing staged driver filling to conventional driver filling is shown in Fig. 13. In this plot, $L_{\text{binary}} = 3.63$ m, $L_{\text{driver}} = 9.57$ m, and $L_{\text{driven}} = 9.73$ m. For clarity, regions labeled “a” correspond to the backfilled gas and those labeled “b” correspond to the binary (tailored) gas. In the staged driver gas shock (shown in solid lines), within the driver section, notice that the lines denoting the expansion fan wave head propagating in the backfilled (low sound speed) gas have a greater slope (time divided by distance) than those showing the conventional driver filling shock expansion fan wave head (shown in dashed lines). This reflects the fact that in the staged driver gas shock, the expansion fan travels more slowly. Also notice that within the tailored gas, the initial slope of the expansion head and tail lines are low, reflecting the fact that the driver gas immediately adjacent to the diaphragm has a high sound speed. This high sound speed allows a strong shock wave to be generated. The net effect of this staged driver gas-filling procedure is that a strong shock wave is produced via the binary mixture, but the expansion wave head is delayed in reaching the test location at the end of the driven section because it must first pass through the low-sound-speed backfilled gas in the driver section. Moreover, helium gas is only needed in a short length of the driver section next to the diaphragm; the rest of the driver section can be filled with a much less expensive alternative such as nitrogen, argon, or carbon dioxide [3].

In the current experiments, we found no evidence that abrupt expansion or shock waves are reflected back to the test section as the reflected shock interacts with the backfill/binary gas contact surface. In contrast, a tailoring mismatch at the tailored driver/driven gas interface generates a distinct pressure change in the test section, such as that demonstrated in Fig. 8. One possible explanation for this discrepancy is that the mixing zone which develops between the backfill and binary gases as the backfill gas flows into the driver section is much more extensive than that which develops between the binary and driven gases as the diaphragm bursts. Because this mixing zone is longer, the transition in gas properties as seen by the reflected shock entering the

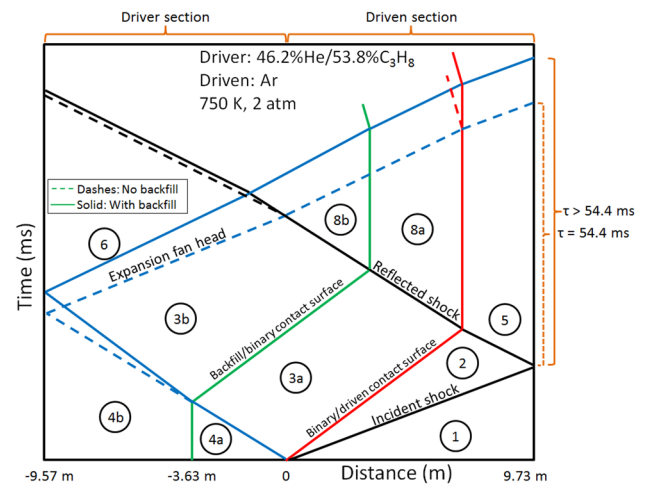


Fig. 13 Idealized $x-t$ diagram comparing staged driver filling (solid lines) to conventional driver filling (dashes), with $L_{\text{binary}} = 3.63$ m, $L_{\text{driver}} = 9.57$ m, and $L_{\text{driven}} = 9.73$ m. Notice that the expansion wave travels more slowly in the low-sound-speed backfill gas, delaying the arrival of the expansion wave at the endwall. Conditions are identical to those in Fig. 2

backfill/binary mixing zone is gradual, and a reflected expansion or shock wave is not generated and sent back to the test section. For this reason, Fig. 13 is drawn with a vertical contact surface line between Regions 8a and 8b, meaning that the backfill/binary gas contact surface is stagnated by the reflected shock. Interestingly, no contact surface bump, as in that shown in Fig. 9, has been observed as the result of the backfill/binary gas contact mixing zone; we attribute this to the similarity in properties between these gases (in the case of the binary/driven gas contact mixing zone, gas properties can vary significantly, and the mixing of these gases does not necessarily result in linearly varying conditions). Finally, in our staged driver gas-filling experiments, we have observed significantly lower non-ideal pressure change $\frac{dP^*}{dt}$ when the expansion wave propagates through the backfill gas as compared to $\frac{dP^*}{dt}$ measured during conventional driver filling (no backfill). We attribute this to the interaction of the expansion

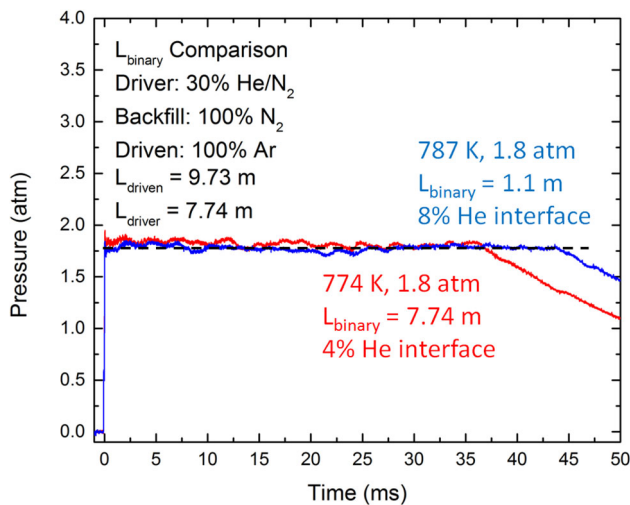


Fig. 14 Comparison of conventional to staged driver gas filling. The use of staged driver gas filling increased test time by roughly 8 ms (22 %) and used 85 % less helium, compared to its conventional counterpart. Conditions: $\frac{A_{\text{driver}}}{A_{\text{driven}}} = 2.38$, $L_{\text{driver}} = 7.74$ m, $L_{\text{driven}} = 9.73$ m. Driver 30 % He/N₂; driven 100 % Ar; backfill 100 % N₂. A driver insert was used to mitigate non-ideal pressure increases

wave with the mixing zone between the backfill and tailored gases; however, further experimentation is necessary to fully understand this phenomenon.

4.3 Staged vs. conventional filling

Figure 14 offers a comparison between the pressure traces of a shock with conventional driver filling ($L_{\text{binary}} = L_{\text{driver}} = 7.74$ m) and a shock with $L_{\text{binary}} = 1.1$ m, where the backfill gas was pure nitrogen. The conventional filling shock was accomplished by filling a pre-mixed 30 % He/N₂ mixture into the driver section. By observing the delayed arrival of the expansion wave, it becomes evident that staged driver gas filling expanded the available test time by approximately 8 ms, or about 22 %. Moreover, the staged driver filling shock required about 85 % less helium than its counterpart.

4.4 Variation of binary length

Figure 15 shows the relationship between test time and L_{binary} for tailored He/N₂ binary gas and pure nitrogen backfill gas. As L_{binary} decreases, a greater proportion of the driver section is filled with the low-sound-speed backfill gas and test time increases. Note that experimental L_{binary} values greater than about 5 m (except the case of filling the entire driven section with a pre-mixed binary mixture) were unachievable, because the corresponding intermediate pressure P_{4a} was too close to the diaphragm burst pressure P_4 . Also shown in this figure are predictions by the Stanford code. Agreement between the Stanford model and experiment is reasonable,

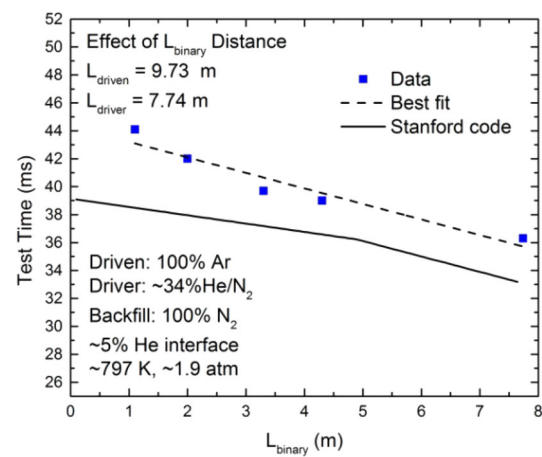


Fig. 15 Test time as a function of binary gas length in the driver section for $\frac{A_{\text{driver}}}{A_{\text{driven}}} = 2.38$. As L_{binary} decreases, the test time increases. Also, within the scatter of the data, this relationship is approximately linear. A comparison is given with backfill test time predictions made by the Stanford code ($\frac{A_{\text{driver}}}{A_{\text{driven}}} = 1.0$) as well

given the assumptions employed in the computer algorithm. Notably, the model correctly predicts the approximate rate of test time increase as L_{binary} is decreased. The underprediction of test times by the Stanford code can be attributed in part to the driver/driven area ratio once again; at this temperature, the simulation required more helium in the binary gas mixture, thus increasing the expansion wave's velocity and reducing predicted test times. Finally, the change in character of the simulation near $L_{\text{binary}} = 5$ m occurs because for shorter L_{binary} , the reflected expansion fan wave head first encounters the reflected shock, whereas for longer L_{binary} , the reflected expansion fan wave head first encounters the backfill/binary gas interface.

4.5 Variation of filling time

To further investigate binary/backfill gas mixing, the flow rate of backfill gas was varied; this resulted in different filling times for the backfill gas. Presumably, as the backfill gas flow rate is increased (i.e., shorter backfill time), the rate of turbulent mixing between the binary and backfill gases should increase, causing the binary/backfill mixing zone to be longer and affecting the resulting test time. However, in our experiments over a wide range of backfilling times, the test time remained constant. Moreover, the non-ideal pressure change $\frac{dP^*}{dt}$ remained approximately constant as well. This could be an indication that the length of the mixing zone has little effect on test time, or that other factors besides backfill gas flow rate are more important in determining the extent of binary/backfill gas mixing.

4.6 Variation of backfill gas sound speed

To investigate the effect of backfill gas sound speed, a series of experiments were conducted using different backfill gases. These gases, in order of lowest sound speed to highest sound speed at 20 C, were 100 % CO₂, 21 % O₂/Ar, 100 % Ar, 21 % O₂/N₂, 100 % N₂, and 30 % He/N₂. A plot relating test time to backfill gas sound speed is provided in Fig. 16. As expected, test time increases as sound speed decreases.

4.7 Selection of backfill gas

The selection of appropriate backfill gas depends on a number of factors, including the desired test time, price of backfill gas, component vapor pressure, and environmental considerations (several potential backfill gases and their properties are provided for reference in Table 1). First, Fig. 16 can be

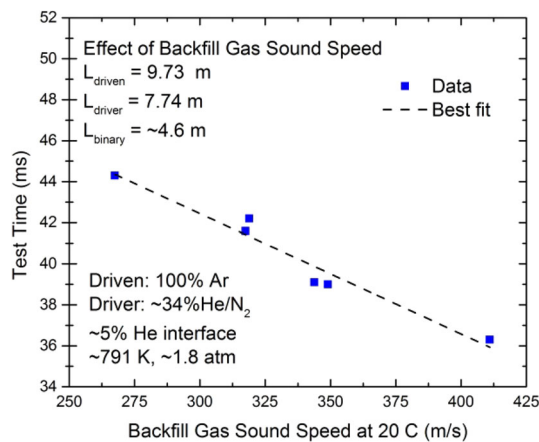


Fig. 16 Test time as a function of backfill gas sound speed at 20 C. The test time is seen to increase linearly with a decrease in the backfill gas sound speed

used as a selection guide for determining the backfill gas necessary to obtain the desired test time, holding other factors (e.g., L_{driver} , L_{driven} , and L_{binary}) constant. Second, backfill gas prices are somewhat dependent on geographical location. However, in general, gases obtained from the atmosphere (e.g., N₂ and Ar), natural gas (e.g., CH₄ and C₃H₈), and combustion products (e.g., CO₂) have reliably low prices. Third, in terms of gas properties, the driver section burst pressure (P_4) is limited by the vapor pressure of the backfill gas [3]. For example, C₃H₈ and CO₂ have vapor pressures of about 9 and 57 atm at 20 C, meaning that the maximum P_4 values when backfilling with these species are 9 and 57 atm, respectively. Since driver burst pressure P_4 generally scales with reflected shock pressure P_5 [22], these gases may be excluded for very high-pressure experiments. Finally, environmental considerations are important factors in choosing a backfill gas. As evident from Table 1, sound speed generally decreases with gas molecular weight, making larger molecules attractive candidates. Several examples include large hydrocarbons (e.g., C₃H₈), noble gases (e.g., Kr and Xe), and insulators/refrigerants (e.g., SF₆ and C₄F₁₀). However, these groups possess some notable drawbacks. In particular, pressurized hydrocarbons have explosive potential, noble gases are often prohibitively expensive unless a trace gas exhaust recovery system is implemented, and insulators/refrigerants are known to be potent greenhouse gases. Moreover, some agents such as CO are known to be poisonous, making even small leaks very dangerous. As such, care must be exercised in selecting the most appropriate backfilling gas for experimentation.

5 Combination of techniques

Figure 17 provides a demonstration of the use of the above techniques in concert. This experiment employed pure argon

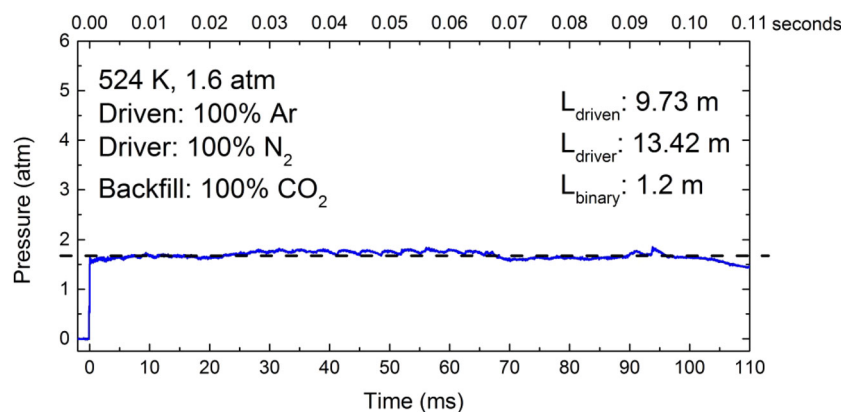


Fig. 17 Demonstration of combined test time extension techniques. This shock shows 102 ms (0.102 s) of test time at $T_5 = 524$ K and $P_5 = 1.6$ atm; the dashed line shows the average pressure (1.695 atm). Conditions: $\frac{A_{\text{driver}}}{A_{\text{driven}}} = 1.0$, $L_{\text{driven}} = 9.73$ m, $L_{\text{driver}} = 13.42$ m,

$L_{\text{binary}} = 1.2$ m. Driver 100 % N₂ (at this temperature, the correct tailoring requires no helium); driven 100% Ar; backfill 100% CO₂. No helium interface gas was needed. A series of driver inserts was used to mitigate non-ideal pressure increases

in the 9.73-m driven section. The 13.42-m driver section was filled with pure nitrogen gas as the tailored “binary” gas mixture (0 % He/100 % N₂) and pure carbon dioxide as the backfill gas. A short L_{binary} value of 1.2 m was used. Moreover, a series of driver inserts were employed to mitigate non-ideal pressure changes. These included a conical insert similar to that of Ref. [6] to reduce the driver section diameter, such that $\frac{A_{\text{driver}}}{A_{\text{driven}}} = 1.0$, allowing the reflected shock wave to pass back into the driver section with no immediate area change. (For $\frac{A_{\text{driver}}}{A_{\text{driven}}} > 1$, an expansion wave is generated and propagates back to the test location when the reflected shock passes back into the driver section; likewise, for $\frac{A_{\text{driver}}}{A_{\text{driven}}} < 1$, a shock wave is generated and propagates back to the test section). In this experiment, the resulting post-reflected shock temperature was sufficiently low that no helium interface gas was required as discussed in Ref. [4]. The resulting pressure trace shows a test time of 102 ms. To our knowledge, this is the longest constant-pressure test time to have been achieved in a reflected shock experiment.

Figure 18 shows the Stanford code’s estimate as to the test time obtainable as a function of T_5 with and without backfilling, for $L_{\text{driven}} = 9.73$ m, $L_{\text{driver}} = 13.42$ m, $L_{\text{binary}} = 1.2$ m, tailored He/N₂ driver gas, argon driven gas, and carbon dioxide backfill gas. Importantly, the introduction of staged driver gas filling can substantially increase the available test time at all temperatures. Relative to the experiment shown in Fig. 17, the model underpredicts the measured test time. Again, this is likely due to the idealized assumptions implicit in the computer code, such as zero backfill/binary gas mixing, but could also be the result of uncertainty in the experimental value of $L_{\text{binary}} = 1.2$ m, since this value does not account for the volume occupied by the inserts employed. Note that the code predicts that backfilling allows for greater

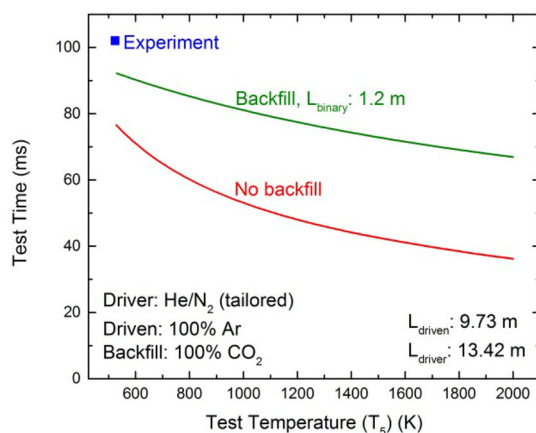


Fig. 18 Benefit of backfill technique on test time versus T_5 . Lines show Stanford code predictions and blue square shows experimental measurement. Conditions: $\frac{A_{\text{driver}}}{A_{\text{driven}}} = 1.0$, $L_{\text{driven}} = 9.73$ m, $L_{\text{driver}} = 13.42$ m, $L_{\text{binary}} = 1.2$ m. Driver He/N₂ (tailored); driven 100 % Ar; backfill 100 % CO₂. No helium interface gas

increases in test time at higher temperatures as compared to low temperatures. This reflects the fact that at high temperatures, a majority of the tailored driver gas consists of helium, implying that replacing this gas with a low-sound-speed alternative can yield great performance enhancements.

6 Sample ignition delay time measurement

We turn now to an example application of the long constant-pressure test time concept by examining a problem of practical interest, namely the measurement of ignition delay time. A sample ignition delay time measurement for an *n*-heptane/21 % oxygen/argon ($\phi = 0.5$) mixture at 4.6 atm and 648 K is provided in Fig. 19. Details of the diagnostics employed in this experiment are available elsewhere [15], hence only a concise summary will be provided here. At these conditions, *n*-heptane exhibits two-stage ignition. The first-stage ignition was monitored by observing the fuel decay according to the Beer–Lambert relation using a continuous wave helium neon (HeNe) laser at 3.39 μm that probes Region 5 at a location 2 cm from the endwall; the decline in absorbance near 50 ms clearly marks this event. Second-stage ignition is monitored by emission from excited OH (OH*) radicals near 306 nm through a port in the shock tube endwall; the rise in the emission signal near 65 ms indicates this occasion and is corroborated by the rise in pressure and the final drop in HeNe absorbance. The second-stage ignition delay time shown is >65 ms, making it, to our knowledge, one of the longest ignition delay times ever measured in a

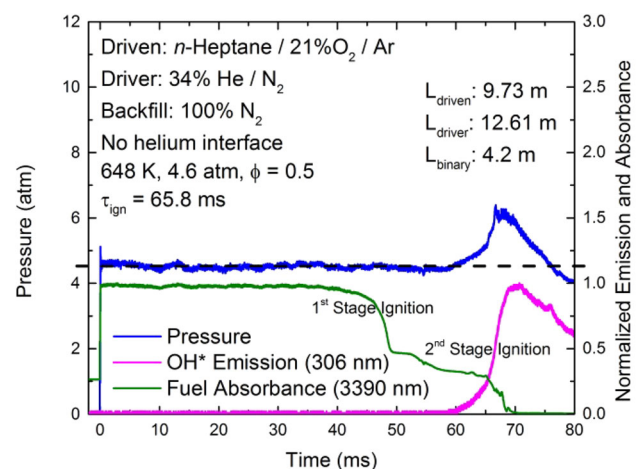


Fig. 19 Sample ignition delay time measurement. The first drop in fuel absorbance indicates first-stage ignition; the rise in OH* emission, rise in pressure, and further drop in fuel absorbance indicate second-stage ignition. Conditions: $\frac{A_{\text{driver}}}{A_{\text{driven}}} = 1.0$, $L_{\text{driven}} = 9.73$ m, $L_{\text{driver}} = 12.61$ m, $L_{\text{binary}} = 4.2$ m. Driver 34 % He/N₂; driven *n*-heptane/21 % O₂/Ar; backfill 100 % N₂. A driver insert was employed to eliminate non-ideal pressure increases, and no helium interface gas was used. $\tau_{\text{ign},1} = 48.0$ ms; $\tau_{\text{ign},2} = 65.8$ ms

shock tube. This experiment would not have been possible without the test time extension techniques discussed in this work and the results provide a good example of the negative temperature coefficient (NTC) region behavior exhibited by many large alkane fuels at practical engine conditions. It is worth noting that these experiments provide data similar to that obtainable in a rapid compression machine (RCM), but without ambiguity associated with the finite compression time and gradual pressure decays in such facilities.

7 Heat transfer

As mentioned in Sect. 1.2, a numerical analysis by Frazier et al. [18] concluded that wall heat transfer does not reduce area-averaged temperature at long times, for shock tubes with 8 cm or larger internal diameters. To examine this statement, we measured gas pressure and temperature *in situ* for several carbon dioxide-seeded experiments (4 % CO₂/Ar) over long test durations. Like the ignition measurement, details of the CO₂-based spectroscopic temperature diagnostic are available elsewhere [15,30], so only a brief overview is provided here. The temperature diagnostic was based on a two-color absorption technique, which exploited the steep inverse temperature dependence between CO₂ transitions in different infrared absorption bands to achieve high sensitivity. Spectroscopic measurement uncertainty is estimated to be <2 % for the reflected shock conditions in these experiments.

Figure 20 depicts one of these shocks, taken at 635 K and 5.1 atm. During this experiment, a very small residual non-ideal pressure change of $\frac{dP^*}{dt} = 0.22$ %/ms was allowed to examine the isentropic relationship between gas temperature

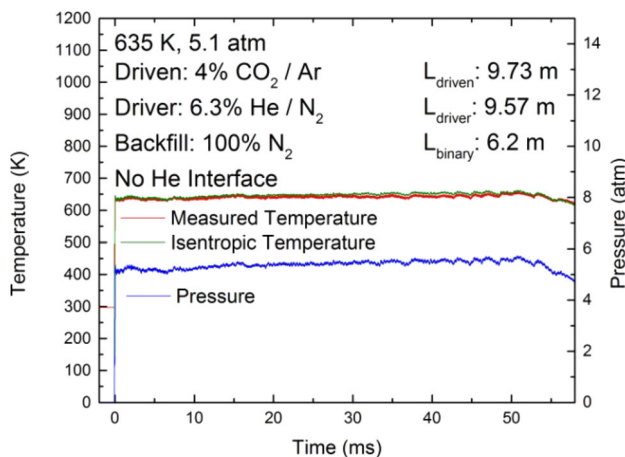


Fig. 20 Sample CO₂-based spectroscopic temperature measurement and comparison with isentropically computed temperature (1). Conditions: $\frac{A_{\text{driver}}}{A_{\text{driven}}} = 2.38$, $L_{\text{driven}} = 9.73$ m, $L_{\text{driver}} = 9.57$ m, $L_{\text{binary}} = 6.2$ m. Driver 6.3 % He/N₂; driven 4 % CO₂/Ar ($\gamma_5 = 1.6128$); backfill 100 % N₂. A driver insert was employed to control the non-ideal pressure increase, and no helium interface gas was used

and pressure (1); near the end of the test time this amounted to an 11 % overall increase in pressure. Several important notes can be made about this graphic. First, the initial post-reflected shock temperature computed based on incident shock speed matches the spectroscopically obtained value to within 0.5 %, which is the approximate uncertainty in the measured temperature; this underscores the reliability of the velocity-based calculation technique used widely in shock tube studies. Moreover, the uncertainty in shock speed-based temperature for this experiment is conservatively estimated to be only about 0.3 % by accounting for errors in measured incident shock speed (0.14 % in this trial), initial (pre-shock) temperature and pressure, and thermodynamic properties (heat capacity and enthalpy). At this stage of development of the laser-based diagnostic, there is slightly less uncertainty in the shock speed-based temperature value than that measured spectroscopically, but the important message is that these values agree within their (small) experimental uncertainties. Second, the subsequent spectroscopically-measured temperature change matches that which was calculated from the change in pressure [assuming isentropic compression according to (1)] very closely. This gives confidence for use of the isentropic relationship to estimate changes in post-reflected shock temperature based on observed pressure profiles. Hence, the conclusion of Frazier et al. that wall heat transfer is not a significant concern in large-diameter shock tubes, like that employed in this work, at conditions similar to those of this study, seems well founded [18]. Were heat transfer a problem, we might expect a significant temperature and pressure drop over the course of the experiment. Note that the spectroscopic diagnostic yields a path-average temperature value; due to conduction heat transfer, the temperature of the gas in the thin boundary layer at the edges of the shock tube will be lower than the bulk temperature. Further work is needed to investigate the role of heat transfer over a wider range of conditions, including higher temperatures.

Finally, it should be noted that under some conditions, shock bifurcations can cause additional effects. Shock bifurcations occur as the reflected shock interacts with the gas boundary layer following the incident shock. While a complete treatment of the effects of shock bifurcations and boundary layers is beyond the scope of this work, it should be noted that these issues are less significant when experimenting with large-bore shock tubes, monatomic gases, and low pressures [31–33]. Additionally, the effects of the shock bifurcation on the post-reflected shock gases are most important immediately following the reflected shock wave and not at long times (though boundary layer mixing that affects the shock tube temperature field can still occur at long timescales like those demonstrated in this work). Nevertheless, the spectroscopic temperature measurements obtained in this work lend confidence to the use of shock tubes at long test times with well-defined thermodynamic conditions.

8 Concluding remarks

We have demonstrated the use of several shock tube techniques for achieving extended reflected shock test times with uniform pressure, including driver inserts, driver gas tailoring, the use of helium interface gas in front of the diaphragm, driver extensions, and staged driver gas filling. The latter method, which involves first filling the driver section with a tailored binary gas mixture, and secondly backfilling a low-speed-of-sound gas near the driver section end cap, can increase test times by approximately 20 % while reducing necessary driver helium consumption by up to about 85 %. By combining the above techniques together, we have achieved an experiment with 102 ms of test time at 524 K and 1.6 atm. We have demonstrated the value of these strategies by measuring long *n*-heptane/21 % O₂/Ar ($\phi = 0.5$) ignition delay times at pressures near 4.5 atm and temperatures near 650 K. Also, we have employed a novel spectroscopic CO₂-based temperature diagnostic to demonstrate the viability of using isentropic relations to predict changes in test temperature based on the measured pressure profile for each shock, and hence have shown that temperature remains constant throughout the entire test duration in long shocks when pressure is held constant. The techniques introduced herein will allow use of shock tubes to explore low-temperature, moderate-pressure chemistry which is of practical importance to a variety of combustion devices in use today.

Acknowledgments This work was supported by the Army Research Office, with Dr. Ralph Anthenien as technical monitor. M.F.C. was supported by the Division of Chemical Sciences, Geosciences, and Biosciences, the Office of Basic Energy Sciences (BES), the US Department of Energy (DOE). Also, during a portion of this work, M.F.C. was supported by a National Defense Science and Engineering Graduate (NDSEG) Fellowship, 32 CFR 168a. Sandia National Laboratories is a multi-program laboratory managed and operated by Sandia Corporation, a wholly owned subsidiary of Lockheed Martin Corporation, for the US Department of Energy's National Nuclear Security Administration under contract DE-AC04-94AL85000. The authors wish to acknowledge Andrew Lawson and Kaley Boyce for their assistance in the configuration of the shock tube, and further wish to thank the technicians in the Stanford University plumbing shop for assistance in configuration of driver inserts.

References

- Ciezki, H.K., Adomeit, G.: Shock-tube investigation of self-ignition of *n*-heptane-air mixtures under engine relevant conditions. *Combust. Flame* **93**(4), 421–433 (1993)
- Shen, H.-P.S., Vanderover, J., Oehlschlaeger, M.A.: A shock tube study of the auto-ignition of toluene/air mixtures at high pressures. *Proc. Combust. Inst.* **32**(1), 165–172 (2009)
- Amadio, A., Crofton, M., Petersen, E.: Test-time extension behind reflected shock waves using CO₂-He and C₃H₈-He driver mixtures. *Shock Waves* **16**, 157–165 (2006)
- Hong, Z., Davidson, D., Hanson, R.: Contact surface tailoring condition for shock tubes with different driver and driven section diameters. *Shock Waves* **19**, 331–336 (2009)
- Dumitrescu, L.Z.: An attenuation-free shock tube. *Phys. Fluids* **15**(1), 207–209 (1972)
- Stotz, I., Lamanna, G., Hettrich, H., Weigand, B., Steelant, J.: Design of a double diaphragm shock tube for fluid disintegration studies. *Rev. Sci. Instrum.* **79**(12), 125106 (2008)
- Hong, Z., Pang, G., Vasu, S., Davidson, D., Hanson, R.: The use of driver inserts to reduce non-ideal pressure variations behind reflected shock waves. *Shock Waves* **19**, 113–123 (2009)
- Rossmann, T., Mungal, M.G., Hanson, R.K.: A New shock tunnel facility for high compressibility mixing layer studies. In: 37th AIAA Aerospace Sciences Meeting and Exhibit, pp. 99–0415. American Institute of Aeronautics and Astronautics, Reno (1999) (Paper Number: AIAA 99-0415)
- Pang, G.A., Davidson, D.F., Hanson, R.K.: Experimental study and modeling of shock tube ignition delay times for hydrogen-oxygen-argon mixtures at low temperatures. *Proc. Combust. Inst.* **32**(1), 181–188 (2009)
- Lam, K.Y., Hong, Z., Davidson, D.F., Hanson, R.K.: Shock tube ignition delay time measurements in propane/O₂/argon mixtures at near-constant-volume conditions. *Proc. Combust. Inst.* **33**(1), 251–258 (2011)
- Gates, S.D., McCartt, A.D., Jeffries, J.B., Hanson, R.K., Hokama, L.A., Mortelmans, K.E.: Extension of Bacillus endospore gas dynamic heating studies to multiple species and test conditions. *J. Appl. Microbiol.* **111**(4), 925–931 (2011)
- Davidson, D., Hanson, R.: Recent advances in shock tube/laser diagnostic methods for improved chemical kinetics measurements. *Shock Waves* **19**, 271–283 (2009)
- Hanson, R.K., Pang, G.A., Chakraborty, S., Ren, W., Wang, S., Davidson, D.F.: Constrained reaction volume approach for studying chemical kinetics behind reflected shock waves. *Combust. Flame* **160**, 1550–1558 (2013)
- Zhu, Y., Davidson, D.F., Hanson, R.K.: 1-Butanol ignition delay times at low temperatures: an application of the constrained-reaction-volume strategy. *Combust. Flame* **161**(3), 634–643 (2014)
- Campbell, M.F., Wang, S., Goldenstein, C.S., Spearrin, R.M., Tulgestke, A.M., Zaczek, L.T., Davidson, D.F., Hanson, R.K.: Constrained reaction volume shock tube study of *n*-heptane oxidation: ignition delay times and time-histories of multiple species and temperature. *Proc. Combust. Inst.* **35**(1), 231–239 (2015)
- Hooker, W.J.: Testing time and contact-zone phenomena in shock-tube flows. *Phys. Fluids* **4**(12), 1451–1463 (1961)
- Polachek, H., Seeger, R.J.: On shock-wave phenomena; refraction of shock waves at a gaseous interface. *Phys. Rev.* **84**(5), 922–929 (1951)
- Frazier, C., Lamnaouer, M., Divo, E., Kassab, A., Petersen, E.: Effect of wall heat transfer on shock-tube test temperature at long times. *Shock Waves* **21**(1), 1–17 (2011)
- Jacobs, P.A.: Quasi-one-dimensional modeling of a free-piston shock tunnel. *Am. Inst. Aeronaut. Astronaut. J.* **32**(1), 137–145 (1994)
- Oakley, J.G., Bonazza, R.: xt.exe software. In: Wisconsin Shock Tube Laboratory (WiSTL), Madison, WI (2004)
- Burcat, A., Ruscic, B.: Third millennium ideal gas and condensed phase thermochemical database for combustion with updates from active thermochemical tables. In: Argonne National Laboratory and Technion Israel Institute of Technology, Report number ANL-05/20 TAE 960 (2005)
- Nishida, M.: Chapter 4.1—shock tubes and tunnels: facilities, instrumentation, and techniques. In: Ben-Dor, G., Igra, O., Elperin, T. (eds.) *Handbook of Shock Waves*, pp. 553–585. Academic Press, Burlington (2001)
- Alpher, R.A., White, D.R.: Flow in shock tubes with area change at the diaphragm section. *J. Fluid Mech.* **3**(5), 457–470 (1958)
- Davidson, D.F., Hanson, R.K.: Real gas corrections in shock tube studies at high pressures. *Isr. J. Chem.* **36**, 321–326 (1996)

25. Oehlschlaeger, M.A., Davidson, D.F., Jeffries, J.B.: Temperature measurement using ultraviolet laser absorption of carbon dioxide behind shock waves. *Appl. Opt.* **44**(31), 6599–6605 (2005)
26. Nuttall, W.J., Clarke, R.H., Glowacki, B.A.: Resources: stop squandering helium. *Nature* **485**, 573–575 (2012)
27. Lifshitz, A., Bauer, S.H., Resler Jr, E.L.: Studies with a single-pulse shock tube. I. The cis-trans isomerization of butene-2. *J. Chem. Phys.* **38**(9), 2056–2063 (1963)
28. Tsang, W.: Thermal decomposition of some tert-butyl compounds at elevated temperatures. *J. Chem. Phys.* **40**(6), 1498–1505 (1964)
29. Robinson, W.M.J.: Mass spectrometric studies of ionization precursors ahead of strong shock waves. Ph.D. Dissertation, California Institute of Technology (1969)
30. Spearrin, R.M., Ren, W., Jeffries, J.B., Hanson, R.K.: Multi-band infrared CO₂ absorption sensor for sensitive temperature and species measurements in high-temperature gases. *Appl. Phys. B* **116**(4), 855–865 (2014)
31. Petersen, E.L., Hanson, R.K.: Nonideal effects behind reflected shock waves in a high-pressure shock tube. *Shock Waves* **10**(6), 405–420 (2001)
32. Petersen, E.L., Hanson, R.K.: Improved turbulent boundary-layer model for shock tubes. *AIAA J.* **41**(7), 1314–1322 (2003)
33. Petersen, E.L., Hanson, R.K.: Measurement of reflected-shock bifurcation over a wide range of gas composition and pressure. *Shock Waves* **15**(5), 333–340 (2006)



ELSEVIER



CrossMark

Available online at www.sciencedirect.com

ScienceDirect

Proceedings of the Combustion Institute 35 (2015) 231–239

Proceedings
of the
Combustion
Institute

www.elsevier.com/locate/proci

Constrained reaction volume shock tube study of *n*-heptane oxidation: Ignition delay times and time-histories of multiple species and temperature

Matthew F. Campbell^{*}, Shengkai Wang, Christopher S. Goldenstein, R. Mitchell Spearrin, Andrew M. Tulgestke, Luke T. Zaczek, David F. Davidson, Ronald K. Hanson

Department of Mechanical Engineering, Stanford University, Stanford, CA 94305, USA

Available online 16 June 2014

Abstract

Ignition delay times of normal heptane have been measured at temperatures ranging from 651 to 823 K and at pressures between 6.1 and 7.4 atm at an equivalence ratio of 0.75 in 15%O₂/5%CO₂/Ar and in 15%O₂/Ar mixtures behind reflected shock waves in a shock tube. Time-history measurements of fuel, OH, aldehydes (mostly CH₂O), CO₂, H₂O, and temperature were also measured under these conditions. These time-histories provide critically needed kinetic targets to test and refine large reaction mechanisms. Measurements were acquired using a novel constrained reaction volume approach, wherein a sliding gate valve confined the reactant mixture to a region near the endwall of the shock tube. A staged-driver gas filling strategy, combined with driver section extensions, driver inserts, and driver gas tailoring, was used to obtain constant-pressure test times of up to 55 ms, allowing observations of the chemistry in the Negative Temperature Coefficient (NTC) region. Experiments with conventional shock tube filling were also performed, showing similar overall ignition behavior. Comparisons between current data and simulations using the Mehl et al. *n*-Heptane mechanism (2011) are provided, revealing that the mechanism generally under-predicts first-stage ignition delay times in the NTC region, and that at low temperatures it over-predicts the extent of fuel decomposition during first stage ignition.

© 2014 The Combustion Institute. Published by Elsevier Inc. All rights reserved.

Keywords: Constrained reaction volume; Ignition delay time; Species time-history; Temperature time-history; *n*-Heptane

1. Introduction

Recent efforts to improve internal combustion engine efficiency have resulted in the need for

better kinetic mechanisms that describe fuel oxidation chemistry at practical conditions. One important fuel that has been the subject of numerous experimental (e.g., [1–5]) and modeling (e.g., [6,7]) studies is normal heptane, as it is a primary reference fuel.

To date, most shock tube ignition delay time studies of *n*-heptane at Negative Temperature Coefficient (NTC) region temperatures (between 600 and 900 K) (e.g., [1–3]) have been performed

^{*} Corresponding author. Address: 452 Escondido Mall, Building 520, Room 520I, Stanford, CA 94305, USA. Fax: +1 650 723 1748.

E-mail address: matthew.campbell@stanford.edu (M.F. Campbell).

at pressures above 10 atm, since available test times for shock tubes have historically been restricted to about 10 ms and ignition delay times are longer than this at lower pressures. As a result, leading kinetic mechanisms (e.g., that of Lawrence Livermore National Laboratory, LLNL [7]) have not been validated at NTC region temperatures and moderate pressures. Moreover, long ignition delay times experimentally measured in shock tubes have been subject to pre-ignition phenomena occurring away from the test location, which have been known to cause an increase in pressure and temperature and ultimately decrease measured ignition delay times [2]. This creates challenges in simulating measured ignition delay times, as conditions during each experiment cannot be properly classified as possessing constant internal energy and constant volume (U–V) [8,9] as has been commonly assumed.

The need for experimental data that are easy to simulate at engine-relevant (moderate-pressure/low-temperature) conditions is evident. Thus we have designed a new shock tube that is able to achieve near-constant-pressure test times of up to 55 ms using a family of techniques including driver extensions [10], driver inserts [11], driver gas tailoring [12], and staged-driver gas filling [13]. Moreover, this shock tube employs a sliding gate valve to confine the reactant mixture to a region near the endwall, minimizing total energy release (and hence pressure change) and eliminating the effects of chemistry occurring far from the endwall; we call this implementation a constrained reaction volume (CRV) shock tube [8,9,14]. Using this device, we have measured *n*-heptane ignition delay times, mole fraction time-histories (fuel, OH, aldehydes, CO₂, and H₂O), and temperature histories at NTC region conditions.

2. Experimental setup

2.1. Shock tube facility

The new CRV shock tube consists of a 9.57-m driver section filled with a high-pressure tailored mixture of helium and nitrogen (see [12]), separated by a polycarbonate diaphragm from a low-pressure mixture called the buffer gas (CO₂/N₂/Ar) in a 9.32-m driven section (internal diameter of 11.53 cm). Positioned at the end of the buffer gas section is the sliding gate valve, which confines the test gas mixture to a 39-cm long test section adjacent to the endwall. The buffer gas is specially formulated so that its molecular weight and specific heat ratio $\gamma = \frac{c_p}{c_v}$ match that of the test gas at the initial temperature of the experiment. Additionally, the driver section is equipped with two filling ports to allow for staged-driver gas filling; one port is used to initially fill the tailored helium/nitrogen mixture, and the second, located

far from the diaphragm, allows a low-sound-speed gas (in these experiments, nitrogen) to be filled subsequently. Since the secondary port is located near the end of the long driver section, the tailored helium/nitrogen mixture immediately adjacent to the diaphragm remains undiluted prior to experimentation.

A shock experiment commences when the final nitrogen is added through the secondary driver port, causing the diaphragm to burst. This rapid bursting results in the formation of an incident shock wave, which moves toward the test section, and an expansion wave, which moves back into the driver section. The velocity of the shock wave is measured using a series of seven PCB model 113A26 transducers. This velocity is extrapolated to the shock tube endwall with an accuracy of $\pm 0.2\%$ and is used to calculate post-shock temperature and pressure to within $\pm 0.6\%$ and $\pm 1.5\%$, respectively, using standard gasdynamic relations and thermodynamic properties. Pressure is measured *in situ* using a Kistler model 601B1 transducer located in the test section, confirming computed conditions. A few seconds prior to diaphragm rupture, the sliding gate valve is opened; *in situ* spectroscopic measurements of fuel concentration have shown that mixing between the buffer and test gases during this short interval is negligible. Since the buffer and test gases have nearly identical molecular weights and specific heat ratios, the velocity and attenuation rate of the shock wave are constant across the buffer-test gas interface. Moreover, this formulation prevents reflected shock/expansion waves at this interface. As the shock wave propagates into the test gas, it heats and compresses this gas from its original volume, spanning a distance $L_1 = 39$ cm between the endwall and the gate valve, to a smaller volume close to the endwall. Ultimately, the shock wave reflects from the endwall of the test section and moves back through the test gas toward the diaphragm, further heating and compressing the test gas. This results in the test gas being stagnated and confined in a volume with a nominal length L_5 as measured from the endwall, enabling spectroscopic and pressure diagnostics to probe the reactive test gas at a location 2.0 cm from the endwall. Typical values of L_5 in these CRV experiments were between 5 and 10 cm, whereas values of L_5 for conventional (entire shock tube) test gas filling were between 130 and 240 cm. Additional details concerning the CRV shock tube technique can be found in Ref. [14].

Meanwhile, the expansion wave in the driver section proceeds through the tailored helium/nitrogen mixture and then propagates into the back-filled pure nitrogen at the end of the driver section. Since this expansion wave travels at the local speed of sound, its velocity is greatly reduced in the pure nitrogen compared to that in the tailored helium/nitrogen mixture. Eventually this

expansion wave reflects from the endwall of the driver section and proceeds back toward the test section; its arrival at the test section ends the experiment. The use of staged-driver filling substantially increases test time by delaying this arrival. Additional details concerning the staged-driver gas filling technique can be found in Ref. [13].

Mixtures were prepared manometrically in stainless steel mixing tanks pumped to less than 0.10 Torr prior to gas mixing. The shock tube was turbo-mechanically pumped to better than 10^{-5} Torr prior to most experiments, with negligible subsequent leak-plus-outgassing. Normal heptane was obtained from Sigma Aldrich (99.3%) and was degassed prior to use; research-grade oxygen, carbon dioxide, nitrogen, and argon were obtained from Praxair, Inc.

2.2. Laser absorption measurements

Details of the laser absorption techniques applied in this study are available in the papers referenced in this section, hence only a brief treatment will be given here. Laser diagnostics are able to make quantitative measurements of gaseous species because the ratio of monochromatic light intensity at frequency ν incident upon an absorbing gas mixture I_o to that exiting the mixture I is related to the number density of absorbing species n according to the Beer–Lambert relation.

$$\alpha = -\ln\left(\frac{I}{I_o}\right) = n\sigma_\nu L \quad (1)$$

In this equation, α is known as the absorbance, σ_ν is the propensity for light absorption by the molecule at frequency ν (called the absorption cross section) and L is the path length along which the absorption occurs.

2.2.1. Laser absorption of fuel

Measurements of fuel concentration were made using the 3.39 μm output of a continuous wave (CW) Helium–Neon (HeNe) laser. Cross section values were obtained from [15–17] and were confirmed using shock tube experiments. Before each shock experiment, the mole fraction of fuel was measured using this spectroscopic technique; measured values were typically 3% lower than manometric values, attributed to fuel loss to the walls of the unheated shock tube. Fuel mole fraction values were also measured between the incident and reflected shocks on each experiment, confirming that mixing of buffer and test gases had not diluted the reactive mixture.

2.2.2. Laser absorption of OH and aldehydes

OH concentration was measured using the output of a narrow-linewidth CW laser at 306.7 nm, the peak of the well-characterized $R_1(5)$ absorp-

tion line in the OH A–X (0,0) band [18,19]. The laser light was obtained by intracavity frequency-doubling of 613.4 nm light generated by a Spectra Physics 380 ring dye laser that was pumped by a 5 W Coherent Verdi at 532 nm. Common mode rejection was used to reduce laser intensity noise, resulting in a minimum detectivity of 5 ppm at the conditions of this work, with an estimated uncertainty of $\pm 10\%$. Measurements were also performed with the laser tuned off the OH line to observe other absorbing species, enabling use of a simple subtraction scheme to cancel spectrally broad interference. At the conditions of these experiments, interference is largely due to molecules possessing a C=O bond, i.e., aldehydes, ketenes, and formic acid. Kinetic simulations performed using the LLNL mechanism [7] revealed that CH_2O is the dominant aldehyde produced during first stage ignition of *n*-heptane. Therefore, the cross section of CH_2O [20] was assumed to represent that of aldehydes/ketenes/formic acid, and time-histories of these species' total concentration have thus been inferred and reported here. Finally, emission by OH at 306 nm in the laser absorption scheme, which used a series of irises to limit radiation reaching the detector, was found to be negligible.

2.2.3. Laser absorption of CO_2

Carbon dioxide mole fraction measurements were attained by a fixed-wavelength direct absorption method near 4.2 μm using a CW external-cavity quantum cascade laser [21]. The laser was tuned to the R(66) transition in the fundamental band near 2387.24 cm^{-1} , which offers minimal absorption temperature sensitivity over the temperature range 700–1000 K. The measurement uncertainty is $<10\%$, and the minimum detectivity is approximately 5 ppm.

2.2.4. Laser absorption of H_2O and temperature measurement

Water mole fraction and temperature measurements were acquired along a single line-of-sight using two frequency-multiplexed tunable diode lasers centered upon H_2O absorption transitions near 3920.09 and 4029.52 cm^{-1} . The wavelength of each laser was scanned across the transition linecenter at 20 kHz and modulated at 90 and 112 kHz, respectively, to monitor first-harmonic-normalized wavelength-modulation spectroscopy with second-harmonic detection (WMS-2f/1f) signals at linecenter. Details regarding the experimental setup and select spectroscopic parameters are given in [22,23].

2.3. Light emission

The emission from kinetically excited OH radicals (OH^*) at $306 \pm 75\text{ nm}$ was also measured

during ignition using a silicon photo-detector and a UG-5 Shott glass band-pass filter. This diagnostic was positioned at both a window located 2 cm from the endwall and at a port in the endwall; ignition delay time measurements at the two locations generally agreed to within 10%.

2.4. Ignition measurement

Ignition delays were measured relative to the time of arrival of the reflected shock, taken here as the time of the half-rise in pressure caused by the reflected shock. First and second stage ignition events in the NTC region were measured by observing the fuel decay process by way of the $3.39\ \mu\text{m}$ HeNe diagnostic. The time of first stage ignition was taken to be the instant of maximum slope in the initial decline of the fuel absorbance, and the time of second stage ignition was taken to be the instant when the absorbance declined to 5% of its initial post-reflected-shock value. At high temperatures, the maximum OH^* emission slope was extrapolated to the baseline (zero) value to determine the ignition delay time.

A sample ignition measurement, including a comparison between CRV and conventional shock tube-filling experimentation, is shown in Fig. 1. Observe that the decreasing HeNe absorbance provides a clear indication of the two stages of ignition. Moreover, comparing the reactive pressure traces to the non-reactive trace near these ignition events serves to illustrate the differences between CRV and conventional experimentation. Near the first ignition event, the conventional shock exhibits a clearly visible and sustained pressure increase, whereas the CRV experiment shows virtually no rise relative to the nonreactive pres-

sure. Furthermore, at the second ignition event, the conventional shock shows an exponential pressure rise to a level roughly four times that of the non-reactive experiment, whereas the CRV experiment shows only a small pressure increase that quickly relaxes to the non-reactive pressure. Importantly, since the CRV shock remains at nearly constant pressure up to and even throughout its ignition process, this experiment can be effectively modeled as a constant enthalpy–pressure (H–P) reactor. In contrast, the conventional-fill experiment cannot be correctly modeled in a simple way, e.g. as a zero-dimensional reactor at constant energy–volume (U–V), though such an approach may be adequate in many cases for simulating first stage ignition, or in strong ignition cases with no pre-ignition energy change. The slight difference in first-stage ignition time, between conventional and CRV experiments, is likely due to small mismatches in equivalence ratio and initial reaction temperature.

3. Results

3.1. Ignition delay times

Ignition delay times for *n*-heptane were measured using the CRV strategy at an equivalence ratio of 0.75 in $15\%\text{O}_2/5\%\text{CO}_2/\text{Ar}$ and in $15\%\text{O}_2/\text{Ar}$ mixtures at 6.5 atm and temperatures between 651 and 823 K. (CO_2 was included in mixtures in support of a new CO_2 -absorption based temperature diagnostic, not reported here. Additionally, CO_2 was not included in the determination of equivalence ratio, and simulations [7] revealed that the presence of CO_2 had negligible effects on ignition kinetics). Measurements were also conducted using the conventional filling strategy throughout this range for purposes of comparison. In addition to these low temperature tests, experiments were conducted using both the CRV and conventional strategies at higher temperatures and a pressure of 7 atm. These ignition delay data are summarized in Fig. 2. Small scaling corrections, obtained from the LLNL mechanism [7] by perturbing pressure and equivalence ratio at several temperatures and observing the effect on τ_1 and τ_2 , to ignition delay times have been applied to normalize individual points to a common P and ϕ (these scaling factors are temperature-dependent). Furthermore, ignition delay time predictions made using the LLNL [7] mechanism have been included in this figure.

Several observations can be made about Fig. 2. First, compare the constant U–V and constant H–P modeling methods (henceforth referred to as simply “UV” and “HP”, respectively). Observe that at high temperatures, the UV and HP simulations yield nearly identical results. However, in the NTC region, the UV simulation yields strikingly

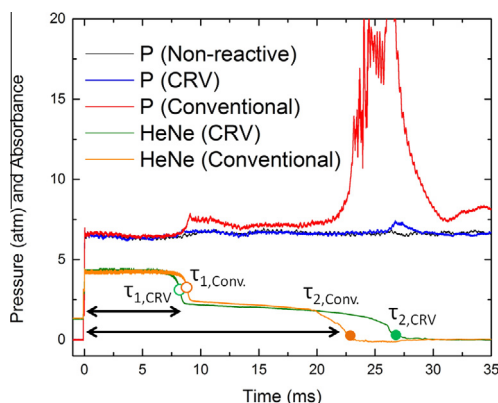


Fig. 1. Comparison between CRV and conventional shock measurements. Reflected shock initial conditions: $\phi \cong 0.75$ (*n*-heptane/ $15\%\text{O}_2/5\%\text{CO}_2/\text{Ar}$), 6.6 atm, $\sim 703\ \text{K}$, $L_5 = 9\ \text{cm}$. Ignition delay times (indicated by open and solid circles): $\tau_{1,\text{CRV}} = 8.2\ \text{ms}$, $\tau_{1,\text{CRV}} = 26.8\ \text{ms}$, $\tau_{1,\text{conventional}} = 8.8\ \text{ms}$, $\tau_{2,\text{conventional}} = 22.7\ \text{ms}$.

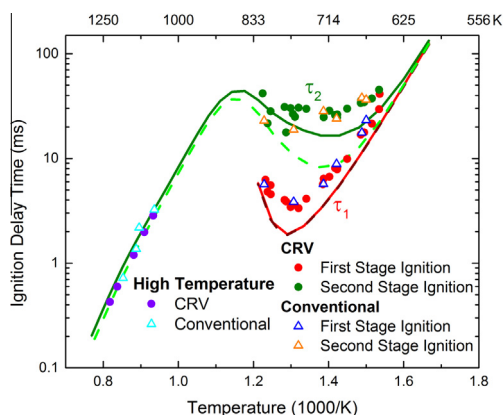


Fig. 2. *n*-Heptane ignition delay time values (*n*-heptane/15%O₂/5%CO₂/Ar, $\phi = 0.75$, 6.5 atm). Solid lines: constant H–P modeling; dashed lines: constant U–V modeling. NTC region data are presented at the initial post-reflected shock temperature, prior to the temperature increase associated with first stage ignition. Error bars are not visible at the resolution used in this plot.

lower second stage (i.e., complete) ignition delay times than the HP simulation, while the two predict identical first stage times. This paradox is the result of an ignition-accelerating pressure increase which occurs in UV simulations during first stage ignition but which does not occur in HP simulations. Since the increase occurs during the first stage ignition but not before, differences between UV and HP trials exhibit themselves in the second stage ignition delay times rather than in the first.

Next, compare the CRV and conventional shock tube experiments. Notice that at high temperatures, CRV and conventional data agree closely with one another (as well as with simulations); this similarity was expected, as nonideal effects in shock tubes typically become important at long times, i.e. at lower temperatures [10]. Also in agreement are the CRV and conventional first stage ignition delay times in the NTC (between 825 and 650 K), consistent with the fact that CRV and conventional pressure traces looked identical up to the point of first stage ignition. Furthermore, at temperatures below about 725 K, the CRV and conventional techniques yield similar second stage ignition delay times with low scatter, in contrast with expectation based on simulations. However, between about 825 and 725 K, the second stage ignition data show significantly more scatter; one possible explanation is that ignition phenomena at these temperatures are more sensitive to the small deviations in pressure present in these experiments relative to the nominal value of 6.5 atm. The LLNL mechanism [7] supports this hypothesis; it gives a pressure scaling of $P^{-2.2}$ at 800 K, whereas at 675 K it is

$P^{-0.9}$. In general, it appears that conventional shocks performed between 825 and 725 K have slightly lower second stage ignition times relative to CRV shocks – currently attributed to the influence of the first stage ignition pressure increase.

Finally, compare the experimental data to the simulations. At high temperatures, the CRV and conventional data are described well by both the UV and HP computations. This reflects the accuracy of both the LLNL mechanism [7] and the suitability of simulating single-stage ignition delay times using the UV constraint when the times are relatively short and non-ideal shock tube effects and pre-ignition energy release are minimal. (Nonetheless, we regard HP modeling as physically more correct in reactive experiments where the measured pressure is constant.) At temperatures below 725 K, it appears that the CRV and conventional complete ignition data are more closely modeled by the HP simulation than by the UV modeling. In contrast, above 725 K, there is slight evidence that the UV simulation may more closely match the conventional data, while the HP model more closely tracks the CRV points. The difference between the measured second stage ignition delay times and the UV simulations, at temperatures below 725 K, can once again be linked to the pressure profiles of the two experiment types. At these low temperatures, the LLNL UV simulation predicts a first stage ignition pressure increase of as much as 40%, whereas that observed in the CRV experiments was negligible and that in the conventional experiments was typically only 10% at all temperatures, reflecting the reality that reflected shock ignition is really not a constant UV process. In the regime above 725 K, the UV model predicts a first stage ignition pressure increase of only about 10%, which more closely matches that observed in the conventional experiments, whereas the CRV data were taken in constant pressure conditions. Finally, observe that the LLNL mechanism predicts a slightly higher temperature (775 K) than the measurements (765 K) at which the minimum first stage ignition time occurs. Further experiments, including species and temperature time-histories, are needed to fully characterize this interesting NTC region.

3.2. Fuel time-histories and first stage fuel decomposition fraction

Additional information on the details of ignition can be obtained by measuring time-histories of important reactants, radicals, intermediates, and products during oxidation. In the present work, we report our first measurements of fuel, OH, aldehydes, CO₂, and H₂O, as well as temperature time-histories, all conducted in the CRV mode of operation. These measurements should provide stronger constraints on the kinetic mechanism, allowing improvements to be made with

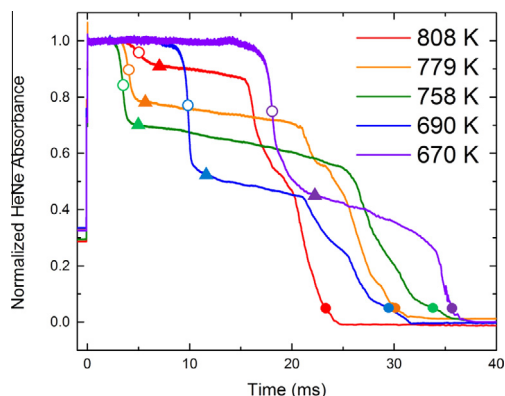


Fig. 3. HeNe absorbance profiles, normalized to unity at time zero, for several temperatures (CRV operation). Conditions: *n*-heptane/15%O₂/5%CO₂/Ar, $\phi = 0.74$, 6.5 atm. Open circles denote first stage ignition (defined as the point of maximum slope), solid triangles denote post-ignition fuel absorbance, and solid circles denote second stage ignition.

more precision than by simply matching global validation targets, e.g. ignition delay times.

HeNe laser absorbance time-histories are plotted at several different NTC region temperatures in Fig. 3. Profiles have been normalized to unity at time zero in order to facilitate comparison. Prior to first stage ignition, some of these measurements have high uncertainty due to high absorbance values (around $\alpha = 4$ in some cases). However, after first stage ignition, absorbance values have fallen due to fuel decomposition such that accurate fuel mole fraction values can be deduced after accounting for interfering species (which also absorb at 3.39 μm) and for the effect of first stage ignition temperature rise on the absorption cross section σ_p .

Several observations can be made from Fig. 3. First, the traces show that first stage ignition delay time decreases with increasing T until about 765 K, at which point first stage ignition delay time increases. A similar pattern can be deduced for second stage ignition, although some shocks showed scatter in ignition time, as discussed above. Furthermore, though convoluted by temperature change and interference, it appears that the fraction of fuel remaining after first stage ignition increases with increasing temperature.

In order to clarify this latter observation, an analysis was performed to quantify the fraction of fuel remaining after first stage ignition. Using the LLNL mechanism [7] with HP modeling, intermediate hydrocarbon mole fractions, as well as the temperature and volume increase upon first stage ignition, were estimated. Also, using cross section values measured by Klingbeil et al. [16], high-temperature absorbance values of interfering species were specified and used to correct the

observed HeNe absorbance. Values for the fraction of fuel remaining after first stage ignition have been plotted in Fig. 4. As also noticed in [5], the fraction of fuel remaining after first stage ignition increases with temperature. Both the data and the model follow an exponential trend, as shown in the semilog scale of this plot. At high temperatures, the LLNL mechanism agrees with the values measured in this work, while it under-predicts these values at low NTC region temperatures.

A sensitivity analysis performed using the LLNL mechanism [7] with HP constraints at 700 K and 7 atm ($\phi = 0.75$) revealed that during first stage ignition the *n*-heptane mole fraction is subject to strong competition between $\text{ROO} \leftrightarrow \text{QOOH}$ rearrangement reactions (promoting ignition) and $\text{ROO} \leftrightarrow \text{Q} + \text{HO}_2$ reactions (inhibiting ignition). Further analysis is necessary to determine the extent to which this competition determines the fraction of fuel remaining after first stage ignition. The analysis also revealed that the fuel mole fraction during first stage ignition is sensitive to the *n*-heptane + $\text{OH} \leftrightarrow \text{R} + \text{H}_2\text{O}$ and $\text{QOOHOO} \leftrightarrow \text{QOOO} + \text{OH}$ reactions.

3.3. OH and aldehyde/ketene/formic acid time-histories

Absorbance profiles of OH and aldehyde/ketene/formic acid were measured during *n*-heptane oxidation at initial temperatures of 669 and 705 K in *n*-heptane/15%O₂/5%CO₂/Ar mixtures with an equivalence ratio of 0.72 using the CRV strategy. To quantify these measurements, the LLNL mechanism was used to predict the post-ignition temperatures, enabling specification of the proper absorption cross section values. The

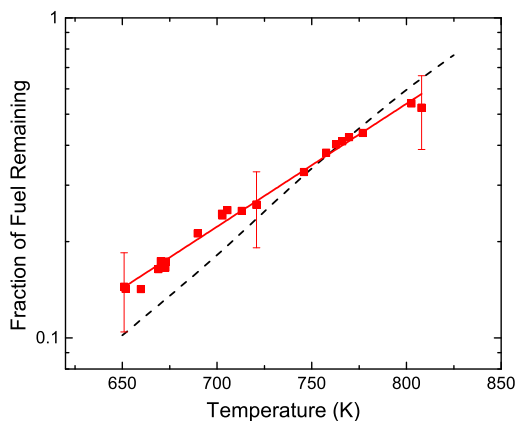


Fig. 4. Fraction of fuel remaining after first stage ignition (points), along with comparison with HP simulation using LLNL mechanism [7] (dashed line) and best-fit line to data (solid line). Conditions: *n*-heptane/15%O₂/5%CO₂/Ar, $\phi = 0.75$, 6.5 atm.

results at 705 K are shown in Fig. 5, together with HP simulations by the LLNL mechanism [7]. In this figure, first stage ignition is marked by a rapid rise in aldehyde concentration, and second stage ignition is marked by the rapid rise in OH concentration (to a predicted plateau level for OH that is dictated by equilibrium thermodynamics) and a characteristically rapid consumption of intermediates. Notice that at these conditions the LLNL mechanism under-predicts these times, consistent with the under-prediction of ignition times shown in Fig. 2. However, the measured plateau values of aldehyde and OH mole fraction match those of the model to within 10%.

3.4. CO_2 and H_2O time-histories

Mole fractions of carbon dioxide and water were measured during *n*-heptane oxidation at initial temperatures of 699 and 744 K in *n*-heptane/15% O_2 /Ar mixtures (no seeded CO_2) with an equivalence ratio of 0.74 using the CRV strategy. The results at 699 K are shown in Fig. 6, together with HP simulations by the LLNL mechanism [7]. First, notice that the first stage ignition delay time, as indicated by the rapidly rising H_2O and CO_2 mole fractions around 9 ms, is under-predicted by the mechanism, consistent with our other measurements. Moreover, the complete ignition time, indicated by the second CO_2 step increase, is also under-predicted (Unfortunately, strong IR emission obscured the second-stage ignition measurement of water.) Note that the CO_2 plateau values following first and second stage ignition closely match those predicted by the mechanism, while the measured initial H_2O plateau value is about 16% lower than the LLNL prediction.

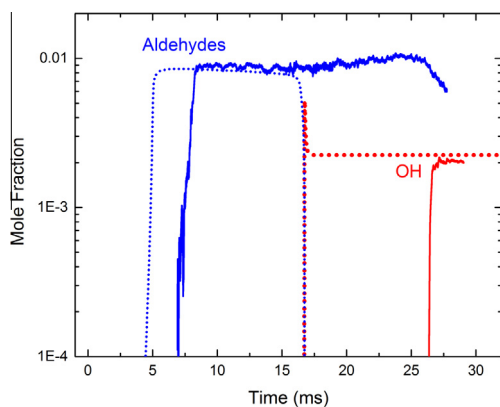


Fig. 5. Measurements of OH and aldehyde/ketene/formic acid mole fraction at an initial (pre-first stage ignition) temperature of 705 K (solid lines), together with HP simulation by the LLNL mechanism [7] (dotted lines). Conditions: *n*-heptane/15% O_2 /5% CO_2 /Ar, $\phi = 0.72$, 6.6 atm.

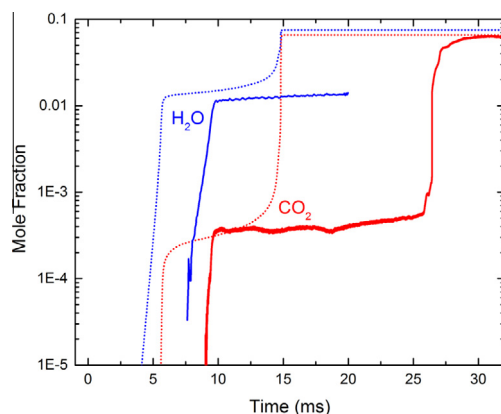


Fig. 6. Mole fraction of carbon dioxide and water at an initial (pre-first stage ignition) temperature of 699 K (solid lines), together with HP simulation by the LLNL mechanism [7] (dotted lines). Conditions: *n*-heptane/15% O_2 /Ar, $\phi = 0.74$, 7.0 atm.

Sensitivity analysis performed for this experiment revealed that the mole fraction of CO_2 is sensitive to a competition between $\text{ROO} \leftrightarrow \text{QOOH}$ and *n*-heptane + $\text{OH} \leftrightarrow \text{R} + \text{H}_2\text{O}$ reactions, but further analysis is needed to quantitatively determine the effect of this competition on the post-first stage ignition plateau level of CO_2 .

3.5. Temperature time-histories and first stage temperature change

First stage temperature measurements were carried out using the water produced in the experiments. (Unfortunately, strong IR emission in these experiments obscured the second-stage ignition event.) These temperature traces are shown in Fig. 7, together with HP-constrained simulation with the LLNL mechanism. Several points are evident. First, observe that the temperature measured after first stage ignition very closely matches that of the simulation. Second, despite beginning at a lower initial temperature, the post-first stage ignition temperature of the 699 K experiment is essentially identical to that of the 744 K experiment; this is shown in both the simulation and the experiment. Finally, notice that the measured temperature remains relatively constant after first stage ignition, whereas that predicted by the HP modeling increases steadily with time, presumably due to incorrect parameters of the mechanism.

Using the thermodynamically calculated pre-ignition temperature as a baseline, the temperature increase during first stage ignition was computed for the two temperature measurements discussed above. The results, together with HP predictions by the LLNL mechanism [7], are shown in the inset of Fig. 7. Interestingly, the simulation predicts an essentially linear relationship

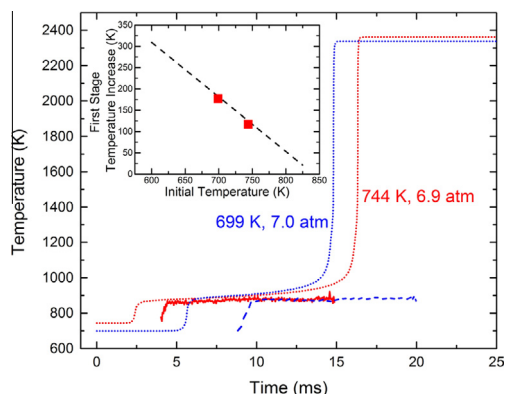


Fig. 7. Temperature time-histories at initial conditions (pre-first stage ignition) of 699 K/7.0 atm (dashes) and 744 K/6.9 atm (solid), together with HP simulation using the LLNL mechanism [7]. Mixture: *n*-heptane/15%O₂/Ar, $\phi = 0.74$. Inset: temperature increase during first stage ignition as a function of initial (pre-first stage ignition) temperature (points), together with HP simulation with the LLNL mechanism [7] (dashed line).

in the temperature increase with the initial pre-first stage ignition temperature. The data match very closely to the simulation, giving confidence in the LLNL mechanism-based temperature-compensation technique used to determine absorption cross section values after the first ignition event in the species time-history analyses above. Although only limited temperature data were observed in this study, the value of such data is seen to be high, and hence we anticipate refining this method and employing it more widely in future work.

4. Summary

We report here the first constant-pressure *n*-heptane ignition delay time data taken at 6.5–7.4 atm in the NTC region using a second-generation CRV technique combined with staged-driver gas filling. Using these techniques, we have achieved test times of up to 55 ms and have observed both first and second stage ignition phenomena under near-constant-pressure conditions. Comparisons between the conventional and CRV filling strategies reveal that ignition delay data taken using these strategies, for the current reactive mixtures and test conditions, agree reasonably well within the scatter of the measurements. In addition to ignition delay times, we measured time-histories of fuel, OH, aldehydes, CO₂, H₂O, and temperature in the NTC region. At high temperatures, we found that the LLNL mechanism [7] with either UV or HP modeling agrees well with the measured single stage ignition delay data. In the NTC region, two stages of ignition were observed. Constant UV and HP simulations for first stage ignition times are

indistinguishable, and the LLNL mechanism consistently under-predicts the measured times. Significant differences were seen between HP and UV modeling of second stage ignition times, with HP simulations generally in better agreement with data. The multi-species and temperature capabilities demonstrated in this study, together with the staged-driver filling technique enabling long test times and the CRV strategy allowing improved gasdynamic modeling, should prove very useful in future studies of combustion chemistry.

Acknowledgements

This material is based upon work supported by the U.S. Army Research Laboratory and the U.S. Army Research Office under contract/grant number W911NF1310206 with Dr. Ralph Anthenien as technical monitor. MFC is supported by a National Defense Science and Engineering Graduate (NDSEG) Fellowship, 32CFR168a. LTZ is supported by the National Science Foundation (NSF) Graduate Research Fellowship Program under Grant No. DGE-114747. The authors wish to acknowledge Andrew Lawson and Kaley Boyce for their assistance in the configuration of the shock tube.

Appendix A. Supplementary data

Supplementary data associated with this article can be found, in the online version, at <http://dx.doi.org/10.1016/j.proci.2014.05.001>.

References

- [1] H.K. Ciezki, G. Adomeit, *Combust. Flame* 93 (4) (1993) 421–433.
- [2] K. Fieweger, R. Bulmenthal, G. Adomeit, *Symp. (Int.) Combust.* 25 (1) (1994) 1579–1585.
- [3] B.M. Gauthier, D.F. Davidson, R.K. Hanson, *Combust. Flame* 139 (4) (2004) 300–311.
- [4] J. Zhang, S. Niu, Y. Zhang, et al., *Combust. Flame* 160 (1) (2013) 31–39.
- [5] D.M.A. Karwat, S.W. Wagnon, M.S. Wooldridge, C.K. Westbrook, *Combust. Flame* 160 (12) (2013) 2693–2706.
- [6] H.J. Curran, P. Gaffuri, W.J. Pitz, C.K. Westbrook, *Combust. Flame* 114 (1–2) (1998) 149–177.
- [7] M. Mehl, W.J. Pitz, C.K. Westbrook, H.J. Curran, *Proc. Combust. Inst.* 33 (1) (2011) 193–200.
- [8] R.K. Hanson, G.A. Pang, S. Chakraborty, W. Ren, S. Wang, D.F. Davidson, *Combust. Flame* 160 (2013) 1550–1558.
- [9] Y. Zhu, D.F. Davidson, R.K. Hanson, *Combust. Flame* 161 (3) (2014) 634–643. <http://dx.doi.org/10.1016/j.combustflame.2013.06.028>.
- [10] K.Y. Lam, Z. Hong, D.F. Davidson, R.K. Hanson, *Proc. Combust. Inst.* 33 (1) (2011) 251–258.

- [11] Z. Hong, G. Pang, S. Vasu, D. Davidson, R. Hanson, *Shock Waves* 19 (2009) 113–123.
- [12] Z. Hong, D. Davidson, R. Hanson, *Shock Waves* 19 (2009) 331–336.
- [13] M.F. Campbell, T. Parise, A.M. Tulgestke, R.M. Spearrin, D.F. Davidson, R.K. Hanson, *Shock Waves*, submitted for publication.
- [14] M.F. Campbell, A.M. Tulgestke, D.F. Davidson, R.K. Hanson, *Rev. Sci. Instrum.*, submitted for publication.
- [15] S.W. Sharpe, T.J. Johnson, R.L. Sams, P.M. Chu, G.C. Rhoderick, P.A. Johnson, *Appl. Spectrosc.* 58 (12) (2004) 1452–1461.
- [16] A.E. Klingbeil, J.B. Jeffries, R.K. Hanson, *Meas. Sci. Technol.* 17 (7) (2006) 1950–1957.
- [17] A.E. Klingbeil, J.B. Jeffries, R.K. Hanson, *J. Quant. Spectrosc. Radiat. Transfer* 107 (3) (2007) 407–420.
- [18] D.F. Davidson, M. Roehrig, E.L. Petersen, M.D. Di Rosa, R.K. Hanson, *J. Quant. Spectrosc. Radiat. Transfer* 55 (6) (1996) 755–762.
- [19] J.T. Herbon, R.K. Hanson, D.M. Golden, C.T. Bowman, *Proc. Combust. Inst.* 29 (1) (2002) 1201–1208.
- [20] S. Wang, D.F. Davidson, R.K. Hanson, *Combust. Flame* 160 (10) (2013) 1930–1938.
- [21] R.M. Spearrin, W. Ren, J.B. Jeffries, R.K. Hanson, *Appl. Phys. B*, in press <http://dx.doi.org/10.1007/s00340-014-5772-7>.
- [22] C.S. Goldenstein, I.A. Schultz, R.M. Spearrin, J.B. Jeffries, R.K. Hanson, *Appl. Phys. B* (in press) <http://dx.doi.org/10.1007/s00340-013-5755-0>.
- [23] K. Sun, X. Chao, R. Sur, C.S. Goldenstein, J.B. Jeffries, R.K. Hanson, *Meas. Sci. Technol.* 24 (2013) 125203.



Full Length Article

Ignition delay time correlations for distillate fuels

D.F. Davidson^{*}, Y. Zhu, J. Shao, R.K. Hanson*Mechanical Engineering Department, Stanford University, Stanford, CA 94305, United States*

ARTICLE INFO

Article history:

Received 17 June 2016

Received in revised form 28 August 2016

Accepted 12 September 2016

Available online 20 September 2016

Keywords:

Ignition delay time

Shock tube

Jet fuel

Rocket propellant

Diesel

Gasoline

ABSTRACT

Ignition delay times were measured behind reflected shock waves in a shock tube for a wide variety of distillate fuels over a range of temperatures, pressures and mixtures. The fuels studied include: jet fuels (JP-5, JP-8, and Jet A), rocket propellants (RP-2), diesel fuels (F-76 and DF-2) and gasoline. A simple correlation was found to describe the ignition delay times for all these fuel/air experiments for equivalence ratios near unity, temperatures from 1000 to 1400 K, and pressures from 6 to 60 atm. A simple correlation was also found for low-fuel-concentration experiments diluted in argon. Previously published ignition delay time data were found to be in good agreement with these correlations. Finally, for several fuels studied, systematic variations were seen in the activation energy for ignition delay time measurements with varying equivalence ratio and oxygen concentration.

© 2016 Elsevier Ltd. All rights reserved.

1. Introduction

The quality and composition of distillate fuels throughout the world varies significantly. With this variation comes a concern that engine performance will be critically affected by fuels with widely varying composition. For certain engines such as gas turbines, significant changes in ignition delay times, for example, can have a significant impact on engine operation. Similarly, high-performance spark ignition engines are sensitive to fuel composition and ignition delay time. For other engines, such as rockets, the assumption that “mixed is burnt” means that for the bulk combustion volume, chemical kinetics are not assumed to play a critical role. Chemical kinetics can however play an important role in predicting rocket engine oscillations and stability. In military engines, the “One Fuel” directive implemented by the U.S. Department of Defense, requires an understanding of the influence of using this one fuel, i.e. jet fuel, in engines designed for other fuels, such as diesel, further motivating the need to understand variations in ignition delay time across a range of distillate fuels.

Thus, there continues to be a wide research effort to develop accurate models for the combustion kinetics of jet fuels and other distillate fuels with particular interest on the role and importance of fuel composition. Critical to this development is a need for accurate kinetics target data to validate and refine these models. Common laboratory modeling targets include ignition delay time (IDT)

and flame speed, which place global constraints on model predictions, and species time-histories that place more specific constraints on the internal sub-mechanisms of these models. Although a wide literature on ignition delay time measurements in shock tubes exists, these data are primarily for neat hydrocarbons and to a much lesser extent for a range of practical distillate fuels. For a review of methods and data, for example, see Lifshitz [1] and Davidson and Hanson [2].

One concern of model developers is that because distillate fuels have variable compositions, kinetics models and fuel surrogates may have to be tuned to the specific composition of the individual fuel to accurately reproduce critical combustion parameter such as ignition delay times and flame speeds. Based on our current knowledge, for example of the large variation of ignition delay times for archetypal individual surrogate components, this concern is justified [3].

Distillate fuels, however, are not composed of a small and limited number of components as are surrogate fuels. Surrogate fuels are often designed to include a small number of selected individual archetypal components of *n*-alkane, iso-alkane, cyclo-alkane and aromatic species. GCxGC analyses of distillate fuels, on the other hand, demonstrate an immense array of different component species. While this large variability in composition might be viewed with concern, recent measurements of distillate fuel pyrolysis products have demonstrated that only a small number of common intermediate species form [4], providing the basis for a possible argument that some combustion characteristics of distillate fuels should actually be similar.

^{*} Corresponding author at: Mechanical Engineering Research Laboratory, 418 Panama Street, Room 104, Stanford, CA 94305, United States.

E-mail address: dfd@stanford.edu (D.F. Davidson).

Related to this, recent work on model development for practical distillate fuels (e.g. the hybrid model of Wang et al. [5]) assumes that ignition may be viewed at high temperatures, simply yet accurately, as initial pyrolysis (including abstraction reactions) followed by oxidation of stable intermediates. This assumption is completely consistent with shock tube measurements of the species time-history of fuel and intermediate fuel product species (e.g. the major product C_2H_4) during *n*-heptane, *n*-dodecane and *n*-hexadecane oxidation [6–8]. With this model, the observed commonality in decomposition products may work in the modeler's favor to simplify the task of generating a common mechanism for all jet fuels. In short, if most fuels generate approximately the same decomposition products, should not the ignition delay times be similar?

This question has been difficult to study because of the paucity of high-temperature IDT data for distillate fuels. In part, this is because of a lack of a single source for research fuel and the inherent variability of the generic fuel composition. Gauthier et al. measured ignition delay times in gasoline in 2004 [9]. Early jet fuel studies were performed by Dean et al. [10]. Vasu et al. in our laboratory then investigated IDT for a series of jet fuels [11]; this work was continued by Zhu et al. for F-76 [12], and Haylett et al. for DF-2 [13]. Wang and Oehlschlaeger [14] and Dooley et al. [15] provided high-pressure ignition delay time for a specific Jet A fuel (POSF4658). Liang et al. measured ignition delay times for China #3 aviation kerosene [16]; Steil et al. measured highly dilute kerosene in O_2 /argon [17]. Other workers have studied jet fuel ignition delay times, but without a major emphasis on gas-phase high temperature IDT (see Ref. [11]).

Recently, Gowdagiri et al. found in a study of F-76 and bio-fuels that high-molecular weight, mostly aliphatic fuels had very similar high-temperature ignition properties [18]. In their study, they found an IDT correlation for these fuels at temperatures above 1000 K of the form

$$\tau_{\text{ign}} = 1.7 \times 10^{-8} \phi^{-0.36} P^{-0.71} \exp(25.82/R[\text{kcal/mol K}]) \text{ [s]} \quad (1)$$

This expression captures the weak dependence on equivalence ratio (ϕ) and an approximate expected dependence on pressure P in atm and temperature T in K for these distillate fuels.

In this study, we further investigate the observation of Gowdagiri et al. about high-molecular-weight fuels and measure the ignition delay times for a wide variety of distillate fuels over a wide range of temperatures, pressures, and mixtures. We find that under certain constraints, these ignition delay times can all be well-correlated with simple relationships.

2. Experimental method

Ignition delay times were measured behind reflected shock waves in two shock tubes. High-pressure measurements (greater than 10 atm) were made in a heated 5.0 cm inner diameter shock tube using scribed aluminum diaphragms; low-pressure measurements (near 1.2 atm) were made in a heated 14.1 cm inner diameter shock tube using polycarbonate diaphragms. The experimental setup for the high-pressure shock tube is shown in Fig. 1. Both shock tubes are helium driven, turbo-molecular pumped, and heated to 90 °C; their accompanying gas mixing assemblies were also heated to 90 °C and turbo-molecular pumped. Full evaporation of the fuel components was verified visually by first evaporating small liquid samples of the fuel in an external glass volume at the same temperature and then expanding this gas into the mixing assembly at an even lower pressure. Separate tests were performed to ensure that the partial pressure in the mixing assembly scaled linearly with the liquid sample volume over the range of fuel sample volumes used for each experiment (typically 0.5–2 cc). Mano-

metric measurements (in the mixing assembly) and laser absorption measurements (in the shock tube) of the fuel loading were then compared to ensure that condensation losses in the transfer and shock tube filling processes were negligible. Incident shock speeds in both shock tubes were measured using arrival times from a series of 5 PCB™ pressure transducers approximately equally-spaced and located near the end wall. Reflected-shock temperatures and pressures based on the measured shock speed extrapolated to the end wall and the ideal frozen-chemistry shock relations, assuming vibrationally-equilibrated test gas in both the incident and reflected regions, were accurately determined ($2\sigma = 1\%$). The assumption that the reflected shock conditions are vibrationally equilibrated was tested and confirmed by Gauthier et al. in heptane/air mixtures [9]. Non-reactive pressure profiles in these experiments (using N_2 instead of O_2 in the mixture) were adjusted using driver inserts to limit pressure (and hence also temperature) variations to less than 1% over the required test times [19]. (A representative non-reactive pressure profile is shown in Fig. 2.)

Ignition delay times were measured using OH^* emission near 306 nm (Thorlabs™ model PDA36A photodiode, UG5 Schott™ glass filter, and simple collection optics) and side-wall pressure using a Kistler™ 603B PZT. Ignition delay times were defined as the time from the arrival of the reflected shock wave at the side-wall observation port (2 cm from the end wall for the low-pressure shock tube and 1 cm from the end wall for the high-pressure shock tube) to the time derived from back extrapolating the steepest rise in the OH^* or side-wall pressure signal to the local baseline. Ignition delay times using the two methods were normally in close agreement (within $\pm 3\%$) with each other.

The largest uncertainty in the IDT measurements can be associated with the influence of the reflected shock temperature on the ignition delay times. With activation energies for the majority of the experiments performed being near 40 kcal/mol, uncertainties of 1% in T_5 , the reflected shock temperature, translates into an absolute uncertainty in the ignition delay times of $\pm 15\%$. (Error bars are not shown on the figures as they are approximately the same dimensions as the symbols.) However, systematic differences in the data of 10% (e.g. because of pressure or fuel/oxygen loading) can readily be distinguished. Representative data for JP-8 and Jet A are shown in Fig. 2. In the JP-8 example, the ramp in $3.39 \mu\text{m}$ absorbance seen in the incident shock regime from -50 to $0 \mu\text{s}$ is a result of a small transverse misalignment of this beam across the shock tube. The temporally-broad pressure rise seen from -10 to $30 \mu\text{s}$ is a result of a bifurcation of the reflected shock wave traveling through the boundary layer that is seen with diatomic gases. The pressure rise seen near 200 ms before the ignition event at 210 ms is a result of weak non-local ignition increasing the local pressure. Individual experiments were examined for non-local ignition occurring away from the end wall and deflagration-to-detonation transitions (DDT) that can shorten measured IDT. Measurements where there is evidence of significant shortening of the measured IDT were not included in the dataset. IDT can also be estimated from rates of fuel consumption measured using IR laser absorption (see next paragraph). Measurements where the effects of non-local ignition or DDT start to become evident at the same time (within $\sim 5\%$) as the estimated IDT (from IR laser absorption) are deemed acceptable.

In order to minimize uncertainty in fuel concentration, this quantity was measured directly in the shock tube using IR laser absorption at $3.39 \mu\text{m}$ and Beer's law; absorption coefficients for each fuel that were measured in separate experiments in our laboratory using the method of Klingbeil et al. [20]. Typical uncertainties in the fuel loading based on these absorption coefficients have a Standard Error of $2\sigma = 2\text{--}5\%$. For all fuels tested, C_NH_M values, needed for accurately determining gas-phase equivalence ratios

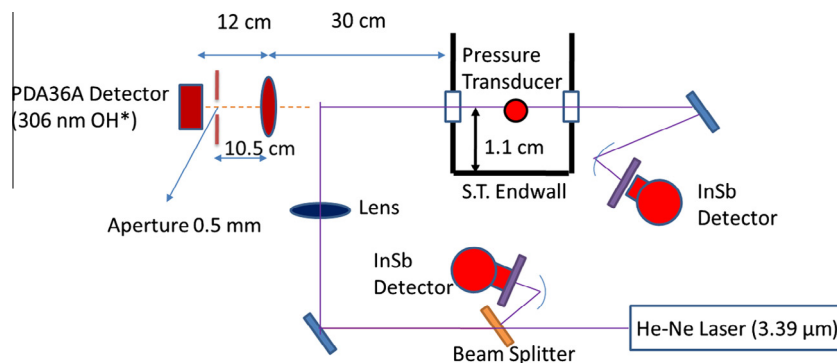


Fig. 1. Schematic of experimental setup for high-pressure experiments.

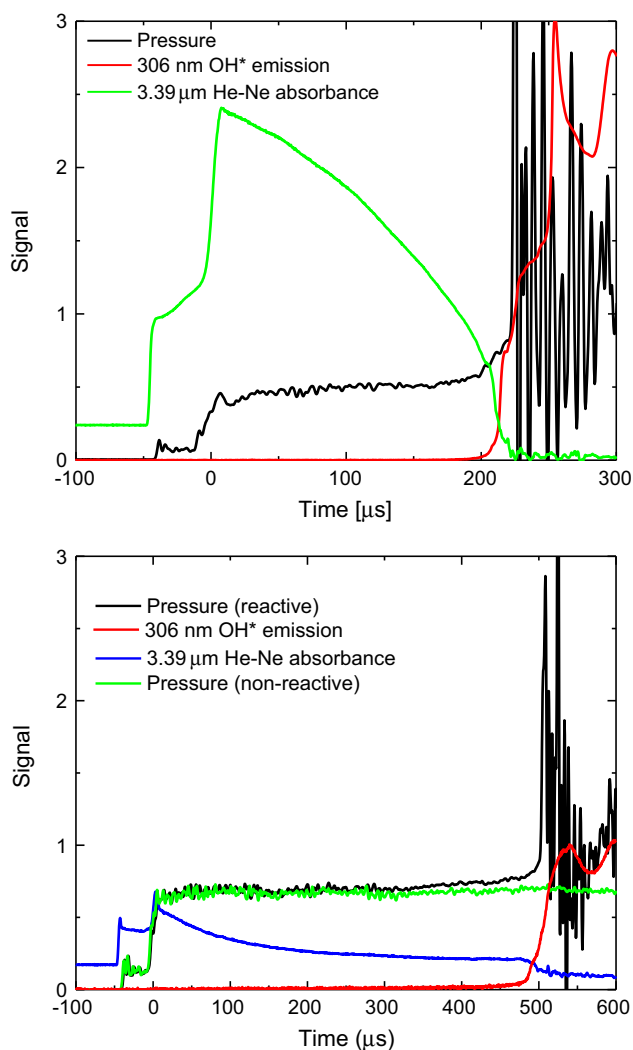


Fig. 2. Representative ignition delay time data. Upper panel: JP-8 (A1)/air, initial reflected shock conditions: 1208 K, 10.2 atm, $\phi = 1.0$; lower panel: Jet A (A2)/4% O_2 /argon, 1278 K, 15.3 atm, $\phi = 1.0$.

in the mixtures, were determined from independent H/C ratio and GCxGC composition measurements [21–23].

Finally, while subtle changes in IDT are expected with changes in equivalence ratio (ϕ), experiments were binned to include all measurements with equivalence ratios between 0.85 and 1.15. This is because in the temperature range of the present study, 1000–

1400 K, and for ϕ near unity, little sensitivity to ϕ was seen in the IDT data. See Section 3.7 for a further discussion of this point.

3. Results and discussion

The correlations of the data are based on recent ignition delay time measurements in a variety of fuels. A summary of these fuels and their properties is given in Table 1. Table 2 outlines the compositions of the first 5 fuels. A table of measured ignition delay times can be found in the supplementary material associated with this paper.

When analyzing the data and evaluating expressions for correlations, the data was binned into several groups, i.e. of high pressure (HP), low pressure (LP), Air versus O_2 /Argon, variable equivalence ratio (ϕ), and variable O_2 mole fraction (X_{O_2}).

New HP air IDT data: distillate fuels in air at high pressures (10–60 atm) with $\Phi = 1$ (0.85–1.15).

Previous HP air IDT data: previously published IDT data for distillate fuels in air at high pressures (10–60 atm) with $\Phi = 1$ (0.85–1.15).

HP 4% O_2 /Ar IDT data: distillate fuels in 4% O_2 in argon at high pressure (10–60 atm) with $\Phi = 1$ (0.85–1.15).

LP 4% O_2 /Ar IDT data: distillate fuels in 4% O_2 in argon at low pressure (1–15 atm) with $\Phi = 1$ (0.85–1.15).

HP N_2 vs Ar IDT data: comparison of IDT of high Pressure (12 atm) distillate fuels in air and 21% O_2 /argon.

Variable X_{O_2} IDT data: comparison of IDT with varying X_{O_2} , O_2 concentration.

Variable Φ IDT data: comparison of IDT with varying ϕ , equivalence ratio.

3.1. New HP air IDT data

All the new ignition delay time (IDT) data in synthetic air for distillate fuels (A1 through G10 in Table 1) for equivalence ratios between 0.85 and 1.15 and for temperatures above 1000 K and pressures from 10 to 60 atm can be correlated with the simple formula

$$\tau_{\text{ign}} = 1.037 \times 10^{-2} P^{-1.194} \exp(30.54/RT) \quad (2)$$

where τ_{ign} is in μs , P is in atm and the activation energy is in kcal/mol and temperature are in Kelvins. Correlations were determined by a linear regression of the logarithm of the IDT (all equally weighted) vs the logarithms of the pressure and inverse temperature. Ignition delay times the same units are also used in Eqs. (3) and (4). Experiments were binned to include equivalence ratios between 0.85 and 1.15, as over this temperature range and equivalence ratio, little sensitivity to τ was seen in the IDT data (see Sec-

Table 1

Fuels for which IDT were measured or cited in this study.

FUEL/identifier	P range [atm]	Equivalent molecular formula	Military POSF# (when available)	Lower heating value (MJ/kg)	Aromatic% (v/v)	Reference
<i>New data</i>						
JP-8 (A1)	1.4–35.9	C _{10.8} H _{21.8}	10,264	43.1	13.4	Present study
Jet A (A2)	0.9–14.5	C _{11.4} H _{22.1}	10,325	43.0	18.7	Present study
JP-5 (A3)	1.0–32.3	C _{11.9} H _{22.6}	10,289	43.0	20.6	Present study
RP-2 (R4)	1.0–52.2	C _{12.0} H _{24.1}	7688	43.6	0.3	Present study
RP-2 (R5)	1.1–15.9	C _{12.6} H _{25.7}	5433	43.8	0.6	Present study
Kerosene (K6)	12.5–59.3	C _{11.5} H _{25.0}				Present study
Kerosene (K7)	21.4–61.6	C _{12.0} H _{23.0}				Present study
DF-2 (D8)	54.6–59.3	C _{13.7} H _{23.0}				Present study
DF-2 (D9)	11.7–56.9	C _{13.6} H _{25.9}	12,407	42.9	19.3	Present study
Gasoline (G10)	13.1–27.8	C _{7.4} H _{13.7}		42.9	30.7	Present study
<i>Older data</i>						
JP-8 (J11)	5.6–37.8	C _{10.9} H _{22.0}	6169		16	[11]
Jet A (J12)	22.0–50.5	C _{10.17} H _{19.91}	4658			[11]
JP-8 (J13)	18.4–30.7	C ₁₁ H ₂₁ est.			13.9	[11]
Jet A (J14)	21.8–26.2	C ₁₁ H ₂₂ est.				[11]
F-76 (F15)	15.9–44.0	C _{14.8} H _{26.9}				[11]
DF-2 (D16)	4.0–7.9	C ₁₂ H ₂₃ est.				[13]
Gasoline (G17)	15.4–54.6	C _{7.5} H _{13.9} est.			30 est.	[9]
Jet A (J18)	8.1–9.5	C ₁₁ H ₂₂ est.			21.5	[10]
Jet A (J19)	16.7–24.8	C _{10.17} H _{19.91}	4658			[14,15]
Kerosene (K20)	5.0–27.6	C _{9.49} H _{19.5}			7.0	[16]
F-76 (F21)	10.0–21.3	C _{14.0} H _{25.1}			16	[18]

Table 2

Composition breakdown for selected fuels. Composition shown in volume %. Values adapted from Refs. [23,24].

	Aromatics	iso-paraffins	n-paraffins	cyclo-paraffins
A1 10264	13.4	39.7	26.8	20.0
A2 10325	18.7	29.5	20.5	31.9
A3 10289	20.6	18.1	13.9	47.4
R4 7688	0.3	38.3	2.6	58.3
R5 5433	0.6	41.4	14.2	43.7

tion 3.7 for a discussion of this point). The Standard Error for this correlation $\sigma = 18\%$ and for the activation energy is 480 K. The new data correlated with this expression are shown in Fig. 3. Of particular note is that the IDT for the kerosene fuels (A1–K8), gasoline (G10) and diesel fuel (D9) exemplars all correlate well with this expression. These fuels span molecular formulae from C_{7.4}H_{13.7} (G10) to C_{13.6}H_{25.9} (D9) and contain between 0.3% (R4) and 30.7% (G10) aromatic components. This insensitivity to aromatic compo-

nents is consistent with measurements of heptane/toluene mixtures performed by Schulz et al. who found little change in IDT from the neat heptane values until a significant fraction of the mixture was aromatic [24]. Uncertainties in the mole fraction of heavy aromatic fuel components, as a result of their high sensitivity to condensation losses in the mixing, transfer, and shock tube filling processes, are thus not expected to have a significant influence on IDT measurements.

3.2. Previous HP air IDT data

Previous distillate fuel/air shock tube ignition delay time data (J11–J14, J18, J19, G17) from our laboratory are compared with this correlation (Eq. (2)) in Fig. 4. These data exhibit greater scatter, but are still in reasonable agreement with Eq. (2). Notably, earlier measurements of the same fuel (J19) by Wang and Oehlschlaeger [14,15] and (J12) by Vasu et al. [9] are in good agreement with this correlation. Good agreement is also seen with the F-76 data (F21) from Gowdagiri et al. [18]. The largest deviation is seen in the shortest-time ignition delay measurements (J18) by Dean et al. [10] that occurred at the highest temperatures (above 1200 K); larger uncertainties are expected at the shorter IDT times reported in that study.

3.3. HP 4% O₂/Ar IDT data

Fig. 5 includes high pressure (10–16 atm and 50–55 atm) distillate fuel data measured in 4% O₂/balance argon (A1, A2, R4, R5, D9, J11, F15). These data (with equivalence ratios between 0.85 and 1.15) can be correlated with the similar formula

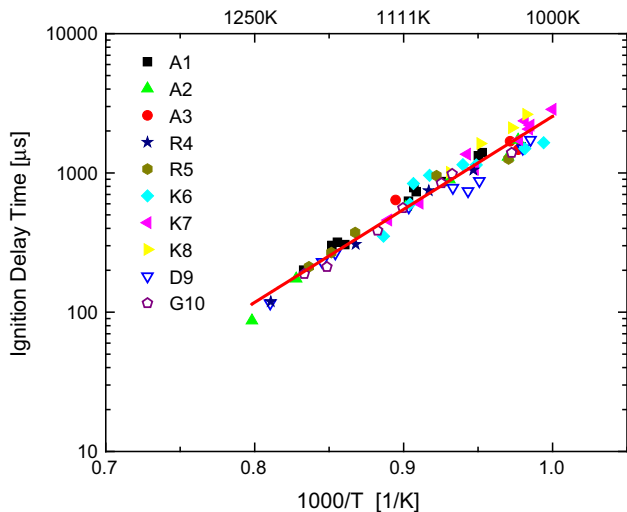


Fig. 3. Ignition delay time data for distillate fuel/air, $\phi = 0.85$ –1.15, normalized to 12 atm using the pressure dependence of Eq. (2). Eq. (2) correlation is shown as a solid line.

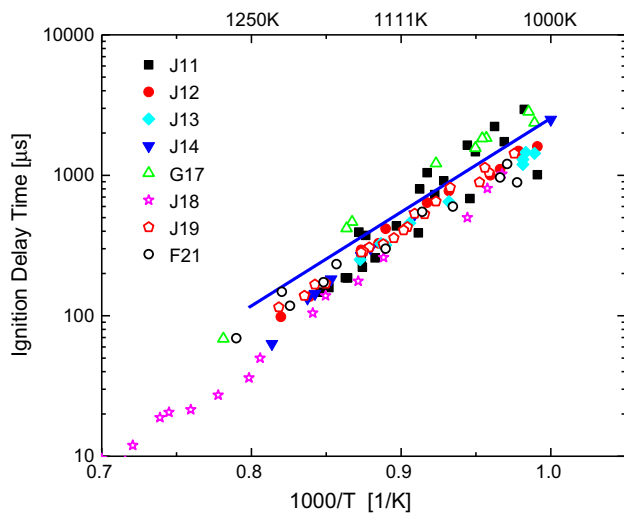


Fig. 4. Ignition delay time data for previously published fuel/air data, $\phi = 0.85$ –1.15, normalized to 12 atm using pressure dependence of Eq. (2). Eq. (2) correlation is shown as a solid line.

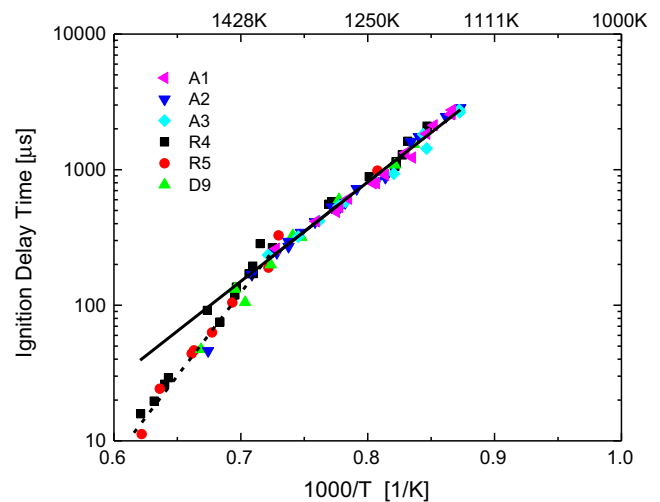


Fig. 6. Ignition delay time data for fuel/4% O_2 /argon data, $f = 0.85$ –1.15, normalized to 12 atm using pressure dependence of Eq. (4). Eq. (4) correlation is shown as a solid line. (Data has been scaled to 12 atm for graphic comparison with other data in this study.)

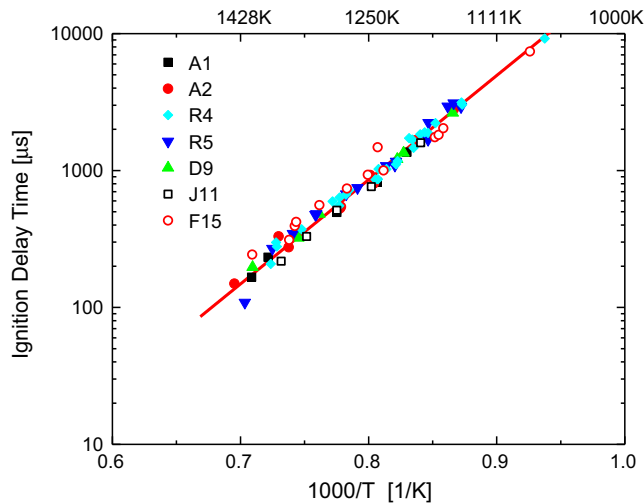


Fig. 5. Ignition delay time data for fuel/4% O_2 /argon data, $\phi = 0.85$ –1.15, normalized to 12 atm using pressure scaling of Eq. (3). Eq. (3) correlation is shown as a solid line. Earlier data are shown with open symbols.

$$\tau_{\text{ign}} = 1.387 \times 10^{-2} P^{-1.205} \exp(34.81/RT) \quad (3)$$

Notably, the ignition delay time data in argon exhibit smaller scatter (Standard Error is 14%) as shock wave experiments in a monatomic carrier gas do not experience large bifurcation in the reflected shock regime or suffer significantly from possible vibrational relaxation effects. Also notable is that the activation energy (Standard Error = 0.68 kcal/mol) of the lower concentration 4% O_2 /balance argon experiments is slightly larger than the activation energy for the fuel/air data. Both sets of earlier data (J11 & F15) are in excellent agreement with the correlation [11,12].

3.4. LP 4% O_2 /Ar IDT data

Fig. 6 includes low pressure, 1–10 atm, distillate fuel data (A1–R5, D9) measured in 4% O_2 balance argon. These data, with temperatures between 1000 and 1400 K and equivalence ratios between 0.85 and 1.15, can be correlated with the formula

$$\tau_{\text{ign}} = 4.73 \times 10^{-3} P^{-0.565} \exp(33.40/RT) \quad (4)$$

Again, the activation energy (Standard error is 0.81 kcal/mol) is slightly higher for this lower concentration (lower fuel and oxygen and lower pressure) data. At temperatures above 1400 K, a higher activation energy (52.07 kcal/mol) would better capture behavior of data for the jet fuels shown; see the dashed line in Fig. 6. It is important to note that while the scaled IDT values in this segment of the plot are less than 100 μs , the actual measured values at lower pressures are longer than 100 μs , and the uncertainties in the IDT values are not different than the lower temperature data. An increase in the reactivity and shorter IDT values at the higher temperatures is likely related to the decreased competition to radical formation and branching (that is directly linked to the rate of the reaction of $H + O_2 = OH + O$) from radical removal or scavenging processes (that are dominated by reactions of pyrolysis and oxidation intermediates with H and OH). These radical removal processes are strongly sensitive to the distribution of fuel decomposition products and to their decomposition products, both of which are expected to change with elevated temperature. Also of note is that for this low-pressure data, the pressure scaling is significantly reduced from the high-pressure region.

Because of the weak dependence on equivalence ratio for rich mixtures (discussed in Section 3.7), data at higher equivalence ratio, up to $\phi = 2$, were also found to be in agreement with this correlation.

3.5. HP N_2 vs Ar IDT data

Fig. 7 shows a comparison of ignition delay times at high pressures (near 15 atm) for A1, A2 and A3 fuels with 21% O_2 in nitrogen (synthetic air) or 21% O_2 in argon as the carrier gas, along with the Eq. (2) correlation. Because of the lower heat capacity (C_p) for the monatomic carrier gas compared to the diatomic nitrogen carrier gas, temperatures modeled using either a constant P or constant V assumption can change differently and in different directions depending on whether the reaction chemistry is endothermic or exothermic. In the case of fuel ignition, during fuel decomposition, an endothermic process, the temperature drop with argon as the carrier gas is larger than in nitrogen. However, during the oxidation process which is exothermic, the temperature rise is larger in argon than in nitrogen. These two effects have an opposite effect on the overall ignition delay time. Argon lengthens the decomposition step, but shortens the oxidation step. The same changes hap-

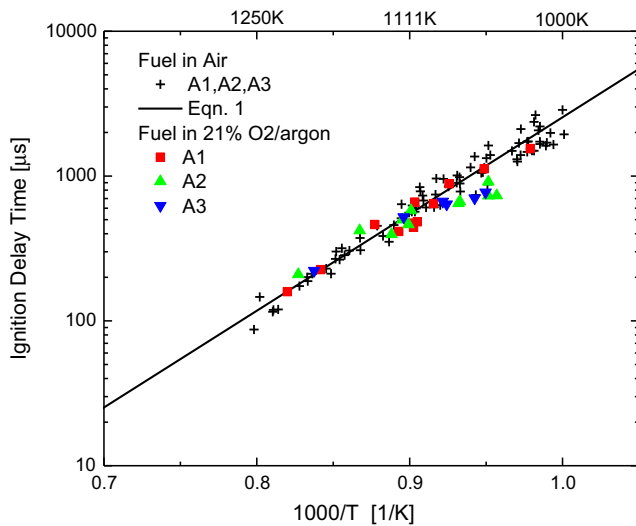


Fig. 7. A comparison of ignition delay time data for fuel/21% O₂/argon and fuel/air normalized to 12 atm.

pen with nitrogen, but to a lesser degree. However, independent of these possible effects, the measured values of the ignition delay times in 21%O₂/argon are very close to the IDT values in air, though there is some evidence that the A2 and A3 fuel/21% O₂/argon are tending to be shorter than the air data at lower temperatures.

3.6. Variable X_{O2} IDT data

Fig. 8 shows a comparison of IDT values for jet fuel (A2) with variable O₂ concentration for equivalence ratios near unity. The variation in O₂ concentration scaling is temperature dependent. The activation energy appears to drop as the fuel and oxygen concentration are increased. In the case of the 1.2 atm 4% O₂/argon experiments, these data fall in the quadratic roll-off region seen in Fig. 5.

At 12 atm in argon, the ratio of the ignition delay times for A2 fuel with 4% and 21% O₂ (a ratio of ~1/5.25) implies an IDT scaling of X_{O2}^{-1.25} in the overlapping temperature window. A simple corre-

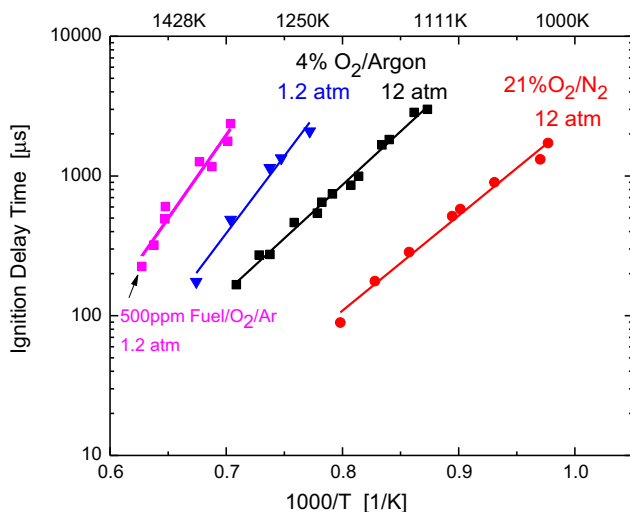


Fig. 8. A comparison of A2 jet fuel ignition delay time data for $\phi = 1$ for varying amounts of O₂ in argon and N₂. The 500 ppm fuel/O₂/Ar data is POSF6169 (Jet A) which is very similar to the A2 fuel.

lation of IDT with O₂ concentration over the full concentration set, however, is not yet possible.

3.7. Variable Φ IDT data

The ignition delay time correlations in the Sections 3.1–3.6 were limited to experiments with equivalence ratios between 0.85 and 1.15. This is because an examination of a larger set of data with a wider range of equivalence ratios shows only limited variation of the IDT with equivalence ratio in this range. Fig. 9 shows the variation of ignition delay time with equivalence ratio for A1 jet fuel for two pressures: 1.2 and 12 atm.

What is evident in Fig. 8 is that the dependence of ignition delay time on equivalence ratio varies with temperature. In addition, this variation produces a cross-over point or temperature, near 1200 K, where there is effectively no dependence of ignition delay time on equivalence ratio for A2 jet fuel. Above 1200 K, as equivalence ratio is decreased, ignition delay times get shorter. Below 1200 K, as equivalence ratio is decreased, ignition delay times get longer. In either case, in this temperature range, small changes in equivalence ratio near values of unity, do not strongly affect the ignition delay times. In contrast to this however, Dean et al. [7] found in their study at 8.1–9.5 atm that higher equivalence ratios always resulted in shorter IDT values, and no cross-over temperature was observed in their data up to 1660 K. Further work is needed to characterize this cross-over.

4. Conclusions

Ignition delay times for a wide variety of distillate fuels were found to be well correlated if care was taken to identify the important variables and areas of commonality. Of importance is the observation that ignition delay times for distillate petroleum fuels in air with stoichiometries near unity scale together when pressure and temperature are considered for temperatures above 1000 K. Large variations in fuel composition do not appear to significantly affect the ignition delay times. This observation is useful in supporting the approach of using a common detailed or reduced mechanism to describe high-temperature jet fuel oxidation.

Equally interesting is the observation that at temperatures above 1000 K, there is only a weak dependence of ignition delay time on equivalence ratio in the range from 0.85 to 1.15. There does appear to be a cross-over temperature near 1200 K, where

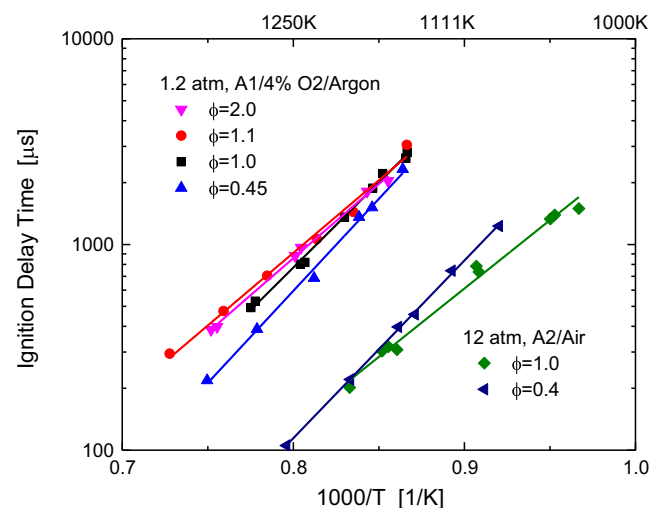


Fig. 9. Variation of ignition delay time with equivalence ratio for A1 jet fuel.

below this temperature the ignition shortens with higher equivalence ratio and above this temperature the ignition time lengthens.

The activation energy of the ignition delay time was also found to be dependent on oxygen concentration for equivalence ratios near unity, with lower concentrations experiencing higher activation energies.

Finally, it should be noted that the commonality seen in the IDT of distillate fuels still needs to be tested over a wider equivalence ratio range. As well, though this commonality in IDT is seen at higher temperatures as seen in this study above 1000 K, there is growing evidence that at lower temperatures (and in the NTC negative temperature coefficient regime) that significant differences in IDT are seen between different distillate fuels.

Acknowledgements

This work was supported by several agencies and companies. Rocket propellant measurements were supported by the Air Force Research Laboratory (AFRL/RQRC, ERC, Inc. PO RS150071) with Matt Billingsley as contract monitor. Jet fuel and diesel measurements were supported by the Air Force Office of Scientific Research through AFOSR Grant No. FA9550-11-1-0217, under the AFRL Integrated Product Team, the U.S. Army Research Laboratory and U. S. Army Research Office under contract/grant number W911NF1310206 and General Electric Research, New York. Gasoline measurements were supported by TOTAL Marketing & Services, Paris France. A portion of the analysis of this data was funded by the U.S. Federal Aviation Administration (FAA) Office of Environment and Energy as a part of ASCENT Project 25 under FAA Award Number: 13-C-AJFE-SU-008. Any opinions, findings, and conclusions or recommendations expressed in this material are those of the authors and do not necessarily reflect the views of the FAA or other ASCENT Sponsors.

Appendix A. Supplementary material

Supplementary data associated with this article can be found, in the online version, at <http://dx.doi.org/10.1016/j.fuel.2016.09.047>.

References

- [1] Lifshitz A. Chapter 16.5: ignition delay times. In: Ben-Dor G, Igra O, Elperin T, Lifshitz A, editors. *Handbook of shock waves*, vol. 3. San Diego: Academic Press; 2001.
- [2] Davidson DF, Hanson RK. Fundamental kinetics database utilizing shock tube measurements. Stanford Digital Repository <<http://purl.stanford.edu/kb621cw6967>>.
- [3] Lawrence Livermore National Laboratory Combustion Mechanisms website <<https://combustion.llnl.gov/mechanisms>> [accessed November 2, 2015].
- [4] Banerjee S, Tangko R, Sheen DA, Wang H, Bowman CT. An experimental and kinetic modeling study of n-dodecane pyrolysis and oxidation. *Combust Flame* 2016;163:12–30.
- [5] Wang H, Xu R, Davidson DF, Banerjee S, Bowman T, Hanson RK. A experiment-based lumped model of jet fuel combustion at high temperatures: a reaction model for POSF10325 Jet Fuel. Stanford University, May 24, 2016, available from haiwang@stanford.edu.
- [6] Davidson DF, Hong Z, Pilla GL, Farooq A, Cook RD, Hanson RK. *Combust Flame* 2010;157:1899–905.
- [7] Davidson DF, Hong Z, Pilla GL, Farooq A, Cook RD, Hanson RK. *Proc Combust Inst* 2011;33:151–7.
- [8] Haylett DR, Davidson DF, Cook RD, Hong Z, Ren W, Pyun SH, Hanson RK. *Proc Combust Inst* 2012;34:369–76.
- [9] Gauthier BM, Davidson DF, Hanson RK. *Combust Flame* 2004;139:300–11.
- [10] Dean AJ, Penyazkov OG, Sevruck KL, Varatharajan B. *Proc Combust Inst* 2007;31:2481–8.
- [11] Vasu SS, Davidson DF, Hanson RK. *Combust Flame* 2008;152:125–43.
- [12] Zhu Y, Li S, Davidson DF, Hanson RK. *Proc Combust Inst* 2015;35:241–8.
- [13] Haylett DR, Davidson DF, Hanson RK. *Combust Flame* 2012;159:552–61.
- [14] Wang H, Oehlschlaeger MA. *Fuel* 2012;98:249–58.
- [15] Dooley S, Wang SH, Chaos M, et al. *Combust Flame* 2010;157:2333–9.
- [16] Liang JH, Wang S, Hu HH, Zhang ST, Fan BC, Cui JP. *Science China-Physics. Mech Astron* 2012;55:947–54.
- [17] Steil U, Braun-Unkoff M, Aigner M. AIAA Paper 2008-973. 46th AIAA Aerospace Sciences Meeting Reno NV; January 2008.
- [18] Gowdagiri S, Wang W, Oehlschlaeger MA. *Fuel* 2014;128:21–9.
- [19] Hong Z, Pang GA, Vasu SS, Davidson DF, Hanson RK. *Shock Waves* 2009;19:113–23.
- [20] Klingbeil AE, Jeffries JB, Hanson RK. *Meas Sci Technol* 2006;17:1950–7.
- [21] Edwards JT. USAF AFMC AFRL/RQTF. Wright-Patterson AFB, Ohio [private communication 2015].
- [22] Xu R, Wang H, Colket M, Edwards T. Thermochemical properties of jet fuels. Stanford University; 2015 [April 5, 2015, private communication].
- [23] Xu R, Wang H, Billingsley M. Thermochemical properties of rocket fuels. Stanford University; 2015 [May 22, 2015, private communication].
- [24] Herzler J, Kikri M, Hiltzbleck K, Starke R, Schulz C, Roth P, Kalghatgi GT. *Combust Flame* 2007;149:25–31.

High-speed OH* chemiluminescence imaging of ignition through a shock tube end-wall

V. A. Troutman¹  · C. L. Strand¹ · M. F. Campbell² · A. M. Tulgestke¹ · V. A. Miller¹ · D. F. Davidson¹ · R. K. Hanson¹

Received: 19 October 2015 / Accepted: 18 December 2015 / Published online: 11 March 2016
© Springer-Verlag Berlin Heidelberg 2016

Abstract A high-speed OH* chemiluminescence imaging diagnostic was developed to image the structure and homogeneity of combustion events behind reflected shock waves in the Stanford Constrained Reaction Volume Shock Tube. An intensified high-repetition-rate imaging system was used to acquire images of OH* chemiluminescence (near 308 nm) through a fused quartz shock tube end-wall window at 10–33 kHz during the combustion of *n*-heptane (21 % O₂/Ar, $\phi = 0.5$). In general, the imaging technique enabled observation of the main ignition event in the core of the shock tube that corresponded to typical markers of ignition (e.g., pressure rise), as well as localized ignition near the wall that preceded the main core ignition event for some conditions. Case studies were performed to illustrate the utility of this novel imaging diagnostic. First, by comparing localized wall ignition events to the core ignition event, the temperature homogeneity of the post-reflected shock gas near the end-wall was estimated to be within 0.5 % for the test condition presented ($T = 1159$ K, $P = 0.25$ MPa). Second, the effect of a recession in the shock tube wall, created by an observation window, on the combustion event was visualized. Localized ignition was observed near the window, but this disturbance did not propagate to the core of the shock tube before the main ignition event. Third, the

effect of shock tube cleanliness was investigated by conducting tests in which the shock tube was not cleaned for multiple consecutive runs. For tests after no cleaning was performed, ignition events were concentrated in the lower half of the shock tube. In contrast, when the shock tube was cleaned, the ignition event was distributed around the entire circumference of the shock tube; validating the cleaning procedure.

1 Introduction

Shock tubes have been used for over 60 years in a wide range of experimental capacities, including the investigation of chemical kinetics over large spans of temperature and pressure [1]. Traditionally, insight into the temperature, pressure and species concentrations in the shock tube is gained through diagnostics that are positioned at ports machined into the side-wall of the test section. For instance, pressure transducers and windows for observing path-integrated light emission or absorption can be positioned at these port locations [2]. While these diagnostics have proven to be valuable, they cannot provide spatial (radial) information regarding the structure and homogeneity of the test gas. A particular need not met by traditional diagnostics is to understand the facility-specific uniformity of the reflected shock reaction volume for exothermic (combusting) mixtures to allow valid comparison of experimental results with chemical kinetics models that assume homogeneous conditions. There are many potential causes of non-uniformity within the shock tube, including non-ideal fluid flow, reflected shock bifurcation and wall heat transfer, though these effects are generally neglected in modeling reflected shock ignition.

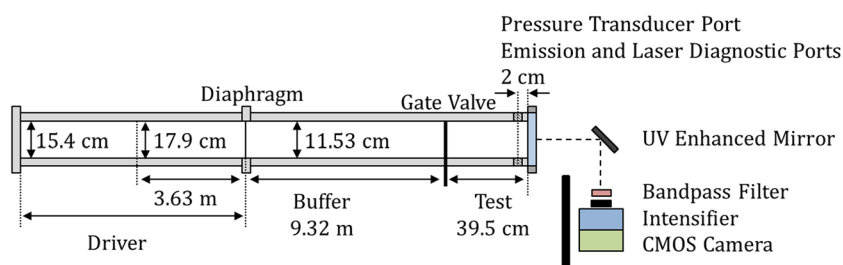
Electronic supplementary material The online version of this article (doi:10.1007/s00340-016-6326-y) contains supplementary material, which is available to authorized users.

✉ V. A. Troutman
vt trout@stanford.edu

¹ High Temperature Gasdynamics Laboratory, Stanford University, Stanford, CA, USA

² Combustion Research Facility, Sandia National Laboratory, Livermore, CA, USA

Fig. 1 The dimensions of the Stanford Constrained Reaction Volume Shock Tube (CRVST) and the configuration of the imaging system are shown



Previous combustion imaging studies in shock tubes have utilized multiple techniques. In early work, Vermeer et al. [3] used schlieren to image the ignition process of hydrocarbons near the end-wall in a rectangular shock tube. Fieweger et al. [4] used shadowgraph to visualize the auto-ignition of several fuels in a square shock tube with transparent side-walls next to the end-wall. Herzler et al. [5] collected a single visible-emission image shortly after the ignition event of propane through a small window in the center of the end-wall of a shock tube. Penyazkov et al. [6] mounted two ($D = 8$ mm) quartz rods into the end-wall to collect emission (OH, CH and C_2 radicals) data simultaneously in the boundary layer and the center of a shock tube for ethylene auto-ignition. More recently, Heufer and Olivier [7] performed schlieren imaging in a rectangular shock tube to investigate biofuel combustion.

Other previous imaging techniques of note investigated various phenomena in shock tubes and similar experimental facilities. Yoo et al. [8] performed toluene PLIF through the side-wall of a shock tube using a transparent and square test section attachment to visualize the flow field and measure the temperature field in non-reactive mixtures at relatively low temperatures. Wegener et al. [9] obtained holographic recordings of the diaphragm rupturing in an expansion tube through optical ports in the wall. In related work, Mansfield et al. [10] used a transparent end-wall in a rapid compression facility to image the ignition process and determine the existence of both inhomogeneous and homogeneous auto-ignition. These imaging studies are akin to imaging in an optically accessible engine, where an understanding of the engine operation can be garnered from watching the combustion process unfold inside the engine cylinder. For example, Stojkovic et al. [11] implemented high-speed OH^* chemiluminescence in an engine through a window located in the piston to study soot formation and oxidation.

In the current work, OH^* chemiluminescence, a common emission diagnostic for combustion systems, was used as a qualitative marker of the reaction zone. OH^* chemiluminescence (peak emission occurring near 308 nm) was used to indicate the locations of high radical concentrations [12, 13]. With emission in the UV, OH^* chemiluminescence was easily studied with very little ambient light contamination by using a band-pass filter.

Here, combustion events in a shock tube were imaged through a UV-transparent (fused quartz) end-wall with a high-repetition-rate intensified camera. The resulting collected images were axially integrated emission indicating the spatial location and geometry of the ignition event. In this work, the reaction volume was constrained to a small portion of the end-wall (see Sect. 2.1 for details), which drastically limited the length of the integration path. For potentially long axial integration paths (e.g., conventional shock tubes), greater care would need to be taken. In general, chemiluminescence images must be interpreted with caution because they are integrated measurements, but they yield powerful information otherwise unavailable from traditional diagnostics through side-wall ports [14].

Through this work, an improved understanding of shock tube performance and diagnostics was sought. Three case studies that illustrate the utility of this imaging diagnostic were performed: Temperature Homogeneity (Sect. 3.1), Shock Tube Wall Defects (Sect. 3.2), and Shock Tube Cleanliness (Sect. 3.3).

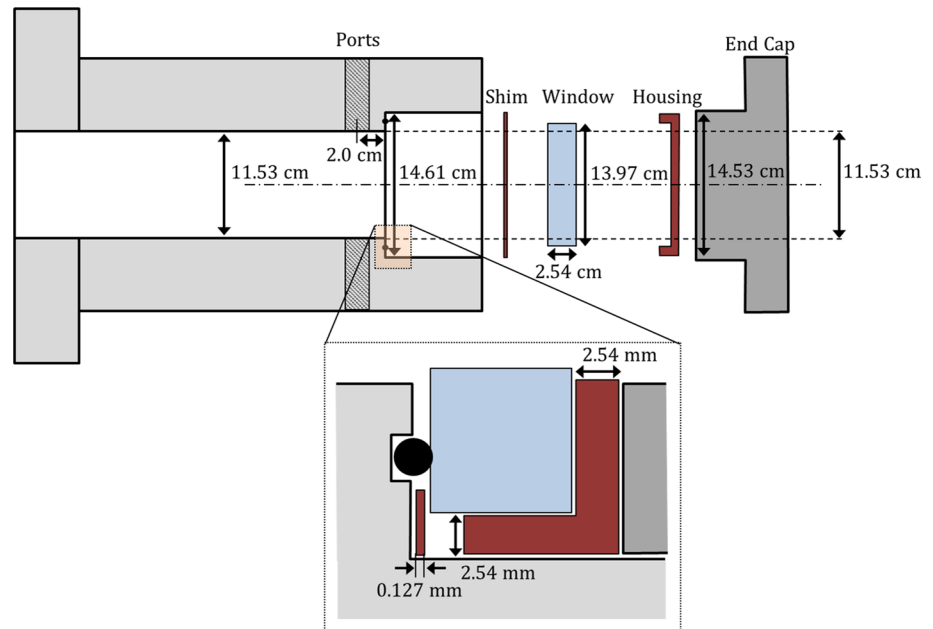
2 End-wall imaging system design

2.1 Stanford Constrained Reaction Volume Shock Tube

The Stanford Constrained Reaction Volume Shock Tube (CRVST), as shown schematically in Fig. 1, was developed to study the kinetics of low-vapor-pressure fuels [15]. The internal diameter of the buffer and test sections is 11.53 cm, and these sections contribute to 9.7 m of the shock tube length. The driver section, with a length of 3.63 m, has an internal diameter of 17.9 cm. A driver extension piece increases the driver section length to a maximum of 13.42 m and has an internal diameter of 15.4 cm (further detailed information regarding the CRVST, the driver section and driver inserts can be found in [16]). Located 2 cm away from the end-wall, machined ports are situated that house windows for laser or emission diagnostics and other sensors such as pressure transducers.

The shock tube was run in constrained reaction volume (CRV) mode. CRV mode employed a sliding gate valve to mechanically confine the reactive gas mixture to a small

Fig. 2 The four-piece transparent end-wall window design allows spatial imaging of the ignition event behind a reflected shock wave through the end-wall of the Stanford CRVST



fraction of the shock tube length, near the end-wall [15]. This gate valve was opened just before the shock wave was initiated, i.e., when the Lexan diaphragm burst, in order to minimize the dilution of the test gas mixture. The axial extent of the test gas after the reflected shock, L_5 , ranged from 5 to 10 cm for the conditions studied [17].

For each experiment, the driver section was filled with a tailored helium and nitrogen mixture. The buffer section contained a tailored mixture of carbon dioxide, nitrogen and argon (see Refs. [15, 16] for driver and buffer gas tailoring details). For all tests presented here, the test section was filled with normal heptane, oxygen and argon, at an equivalence ratio of $\phi = 0.5$. Research-grade helium, nitrogen, carbon dioxide, argon and oxygen were obtained from Praxair, Inc., and spectroscopic-grade normal heptane from Sigma-Aldrich was used. Test gas mixture compositions were determined via partial pressures in a mixing tank. Best practices previously developed to minimize the effect of mixing of the test gas and buffer gas were followed [17].

Initial test gas conditions (behind the reflected shock wave) were calculated from the speed of the incident shock wave, determined using the time-of-arrival technique via seven side-wall pressure transducers (PCB-113A26) distributed over the last section of the shock tube. Time zero for the experiment was defined at the half-rise of a Kistler (603B1) pressure transducer signal for the pressure jump due to the reflected shock wave. This pressure transducer was located 2 cm from the end-wall and was covered in room-temperature vulcanizing silicone (RTV). For reference, the time difference between the incident shock arrival at the end-wall and the passage of the reflected shock by the pressure transducer at 2 cm was typically 70 μ s and

varies slightly with initial conditions. Additionally, a traditional OH* emission diagnostic at 2 cm from the end-wall was implemented using a focusing lens, slit, UG-5 Schott Glass band-pass filter and a silicon photodetector (Thor-Labs PDA36A). Signals from the pressure transducers and emission detector were acquired at 10 MHz using a LabVIEW data acquisition system.

Initial reflected shock temperatures for this work ranged from 1057 to 1240 K. Initial reflected shock pressures ranged from 0.25 to 0.81 MPa.

2.2 End-wall window

The transparent end-wall window, as shown in Fig. 2, consists of four pieces: shim, window, housing and end cap. The window is a 13.97 cm (5.5 in.) diameter, 2.54 cm (1 in.) thick cylinder. In this work, a fused quartz window (GM Associates) transmits the 308 nm OH* chemiluminescence. This easily removable window is a critical design feature, as it allows cleaning of the window with acetone between experiments. The design also does not require any RTV or sealant, further aiding in the ease of window removal and re-installation. The window is rated for a maximum pressure of 2.4 MPa (safety factor of 4). An important feature of this end-wall window design is that it allows optical access out to the edge of the shock tube wall.

The Teflon shim is 0.127 mm (0.005 in.) thick and prevents over-tightening of the shock tube end cap. It allows the shock tube to be adequately sealed, while preventing excessive compressive stress on the window that can cause cracks. The 2.54 mm (0.1 in.) thick Teflon housing holds the window and protects the back of the window from

contact with the metal of the shock tube end cap. The end cap interior is hollow and is attached to the test section of the shock tube using four bolts.

2.3 Imaging system

A Vision Research Phantom v710 high-speed CMOS camera coupled to an intensifier was used to collect the OH* chemiluminescence. The intensifier was a LaVision HS-IRO equipped with a gen II S20 photocathode. A Sodem UV lens, with a focal length of $f = 100$ mm, was used with the aperture set to $f/4$ for all cases. To filter out stray light and other emission, an Asahi Spectra high-transmission band-pass filter centered at 313 nm with 10 nm FWHM was used.

In the interest of protecting the camera and intensifier in the event of a window or end cap failure, a UV-enhanced mirror was used to position the camera at a 90° angle to the shock tube (Fig. 1). Additionally, a shield was placed between the shock tube and camera.

For the v710 camera, there is a trade-off between image resolution (height \times width pixels) and acquisition rate; a smaller window of pixels enables a faster acquisition rate. To allow the full shock tube cross section to be imaged at a faster rate, the camera was moved farther away from the shock tube. In this study, resolutions were used that range from 448×376 to 880×800 pixels, corresponding to acquisition rates of 33–10 kHz (inter-frame times ranging from 0.03 to 0.1 ms), respectively.

For the highest resolution, the projected pixel size was 6.59 pixels/mm (0.15 mm/pixel). For the lowest resolution, the projected pixel size was 3.26 pixels/mm (0.31 mm/pixel). The depth of field for the 10 kHz setup was around 13 cm and for the 33 kHz setup was around 110 cm, both captured the full depth of the compressed test gas section ($L_5 = 5$ cm). The system was focused at the location of the diagnostic ports, 2 cm from the end-wall.

The intensifier was gated to 4 or 5 μ s. The intensifier gain was adjusted specifically to visualize the locations of the earliest flames with 25–50 % of the maximum possible camera signal level. In this work, the gain was typically set at 50–60 % of the maximum gain setting.

3 Results and case studies

3.1 Temperature homogeneity

In a typical shock tube auto-ignition experiment, it is assumed that the test gas is uniformly heated by the reflected shock wave and rapid reaction occurs homogeneously throughout the reactor volume at the ignition delay time (IDT). The collected Kistler pressure transducer (2 cm

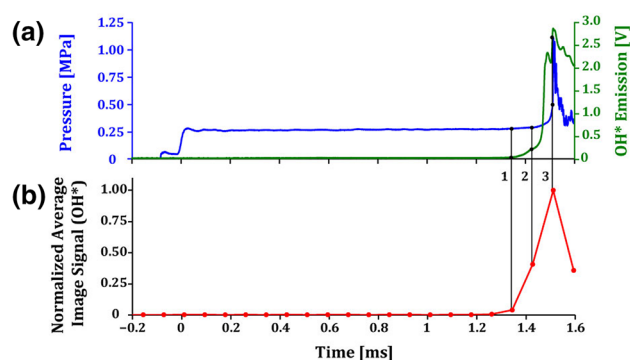


Fig. 3 **a** The pressure trace from the Kistler pressure transducer and voltage from the OH* emission detector (2 cm from the end-wall) of the combustion of *n*-heptane (21 % O₂/Ar, $\phi = 0.5$) are shown. The initial reflected shock conditions were 1159 K and 0.25 MPa. **b** The normalized spatially averaged signal from the collected end-wall images is shown. The images were recorded at 12 kHz with 5 μ s exposure time. The solid vertical bars were numbered corresponding to the timing of the images shown in Fig. 4

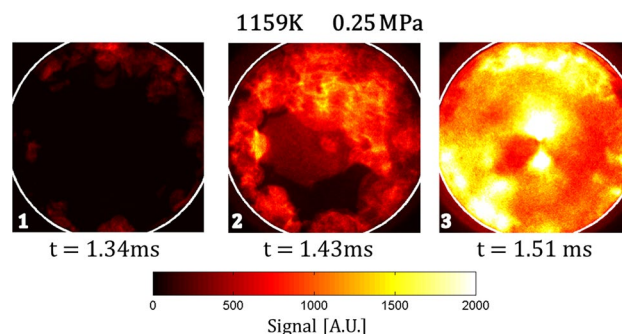


Fig. 4 The combustion of *n*-heptane (21 % O₂/Ar, $\phi = 0.5$) with initial reflected shock conditions of 1159 K and 0.25 MPa was recorded at 12 kHz with 5 μ s exposure time. A white outline was included to mark the location of the shock tube wall. The timing of the three images was also indicated in Fig. 3

from the end-wall) signal is shown in Fig. 3a. The first rise in pressure (near $t = -0.1$ ms) is due to the incident shock wave passing over the pressure transducer and the second rise ($t = 0$ ms) is due to the reflected shock wave. The subsequent large “spike” in pressure (near $t = 1.5$ ms) corresponds to the ignition event and is representative of how IDT may be measured. Small changes in the pressure transducer signal or emission diagnostic, prior to the dramatic increase in pressure, are observed under some conditions and may be taken as evidence of partial inhomogeneity in the ignition event that needs to be better understood.

This imaging technique revealed the spatial distribution of ignition events that occurred in the shock tube as they evolved in time. By acquiring a time series of images, the variability and hence the uncertainty in the IDT were quantified. Uncertainty in measuring the IDT is an often discussed

topic due to multiple choices of definitions, ignition indicators, and a large variability in initial conditions. IDT indicators include the pressure signal or various species from laser absorption diagnostics. Definitions of IDT include the peak, time of the maximum rate of change, or extrapolating the maximum slope to the zero signal level of the chosen indicator [18]. In this work, the OH* chemiluminescence collected in the *images* was used for defining the IDT.

In the case presented in Fig. 3, significant (>0.01 normalized average image signal) OH* chemiluminescence was observed in the image at the time of the first vertical line, before indication of ignition was observed in either the pressure transducer signal or the traditional OH* emission diagnostic (both located 2 cm from the end-wall). The CRVST is generally employed under conditions where pressure increases are minimal, thereby facilitating reaction modeling. Here, higher fuel concentrations and reaction temperatures were intentionally chosen to emphasize inhomogeneous effects and pressure variations.

Figure 4 shows three sequential images collected at 12 kHz (inter-frame time of .083 ms) for the test reported in Fig. 3. A video is available in the supplementary material that contains additional images collected for the test depicted in Figs. 3 and 4.

In the first image ($t = 1.34$ ms) of Fig. 4, initial OH* chemiluminescence was observed near the walls of the shock tube (indicated by the white outline). Ignition in the core was evidenced in the second image ($t = 1.43$ ms), and ignition was evident everywhere within the shock tube cross section by the time of the third image ($t = 1.51$ ms).

Using the timing of the images and known characteristics of the combustion event, a semiquantitative estimate of the homogeneity within the shock tube was made. Equation 1 expresses the exponential temperature dependence of the IDT in an Arrhenius-like form. The relationship between the variation (a measure of uncertainty) in the IDT and the variation in temperature is shown in Eq. 2 where A is the pre-exponential factor, E_a is the activation energy, R is the universal gas constant and T is the temperature. Depending on the IDT correlation, the pre-exponential factor can be expressed as a function of multiple experimental variables (e.g., pressure, oxygen concentration and equivalence ratio) [19].

$$\tau_{\text{ign}} = A \exp\left(\frac{E_a}{RT}\right) \quad (1)$$

$$\frac{\Delta \tau_{\text{ign}}}{\tau_{\text{ign}}} = \left(\frac{-E_a}{RT}\right) \left(\frac{\Delta T}{T}\right) \quad (2)$$

Using Eq. 2 and the assumption that the pressure was uniform throughout the test volume, the spatial variation in temperature was estimated from the variation of the IDT throughout the test section. The key assumption here was

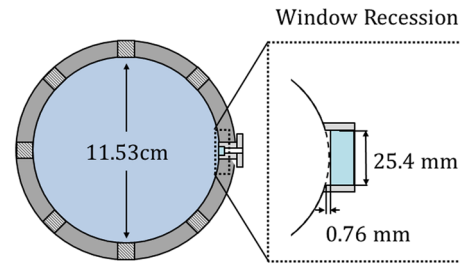


Fig. 5 Port locations are equally spaced circumferentially at an axial distance of 2 cm from the end-wall in the Stanford CRVST. The 0.76 mm recession caused by the window is exaggerated in the drawing. The plug that houses the flat window has the same contour as the shock tube wall

that the pockets of gas within the reaction volume ignited at different times due to the slight temperature differences. Though this was a simplistic assumption, it was nevertheless useful for initial quantification of the temperature variation.

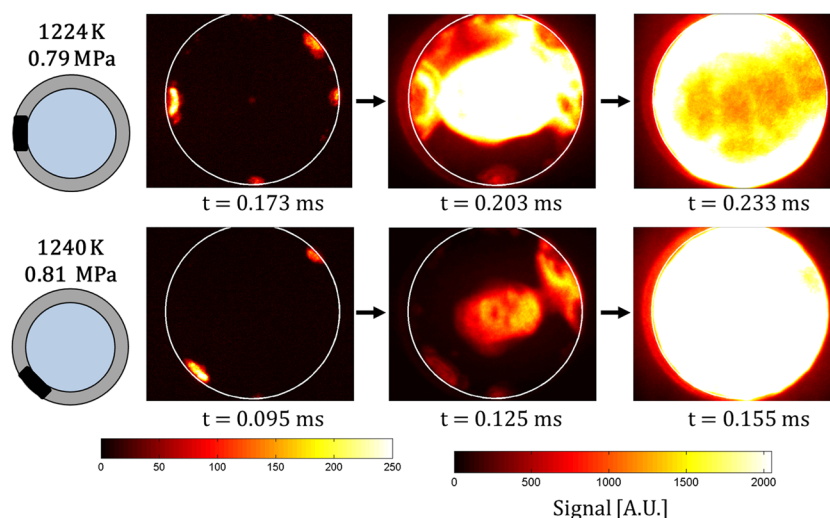
The variation in the IDT throughout the shock tube was estimated as the time interval between the first image with significant OH* chemiluminescence ($t = 1.34$ ms) and the core ignition event with the maximum OH* chemiluminescence ($t = 1.51$ ms). This corresponded to a value of $\Delta \tau_{\text{ign}} = 0.17$ ms. Using Eq. 2 and $E_a = 186.6$ kJ/mol (44.6 kcal/mol) for *n*-heptane, a value of $\Delta T = 6.7$ K was obtained [19]. This estimate indicated that the temperature variation throughout the test section was around 0.5 % for this case.

3.2 Shock tube wall defects

To implement laser absorption and emission diagnostics in the Stanford CRVST, windows are placed in machined ports located 2 cm from the end-wall. There are eight ports equally spaced around the shock tube circumference, which can be filled with smoothly contoured plugs or plugs containing windows. When windows are installed, a 0.76 mm recession is created in the wall at the top and bottom of the window surface (Fig. 5).

These recessions may cause spatial temperature non-uniformities due to interactions with the incident and reflected shock waves. To test this hypothesis, window plugs were installed at different circumferential locations during ignition experiments. Indeed, reactions localized to the windows were observed, as shown in Fig. 6. Initial flames formed at the location of the window, in addition to other locations (some seemed to correspond to locations of smooth plugs, i.e., plugs without windows) along the shock tube wall. A magnified color scale was used to display the first image of the sequence to highlight the location of the initial flames.

Fig. 6 The effects of the window location, evolving over time, were recorded at 33 kHz with 4 μ s exposure time for the combustion of *n*-heptane (21 % O₂/Ar, $\phi = 0.5$). The first image of each sequence has a magnified color scale to highlight the location of the initial flames. The initial reflected shock temperature and pressure along with the window location (*black rectangle*) were labeled for both experiments. A *white outline* was included to mark the location of the shock tube wall



These findings demonstrated that the small recession in a window plug can be sufficient to promote initial local reactions. However, ignition in the core seemed unaffected. The flames that formed on the wall did not propagate to the core before the main ignition event. Nonetheless, it is important to recognize the possibility of local reactions near windows when implementing line-of-sight absorption or emission diagnostics. This could lead to a bias toward shorter measured ignition delay times by those diagnostics and could be an explanation for the early rise in OH* emission diagnostic seen in Fig. 3a for the previous case study.

3.3 Shock tube cleanliness

After three to five experiments in the shock tube, particulate can accumulate near the end-wall of the shock tube. Procedures for cleaning the shock tube have been developed to minimize the potential effects of these particulates. The CRVST was cleaned between experiments by brushing out and cleaning the last 2 m length near the end-wall with acetone before mechanically pumping the shock tube to a pressure of <0.1 Pa. The efficacy of the cleaning methodology was investigated by imaging the combustion event after the shock tube *was not* cleaned.

Figure 7a shows two different combustion events that took place after the shock tube *was not* cleaned for multiple runs (the shock tube was always pumped down between runs). Bright spots were seen that likely result from the small particulates that accumulated at the bottom of the shock tube. Many seemingly independent flames were observed to initiate in the bottom of the shock tube.

Figure 7b shows preignition images from tests after the shock tube *was* cleaned at similar initial reflected shock temperatures and pressures. The reaction zones were distributed circumferentially for both tests, in contrast to the tests conducted with particulates present.

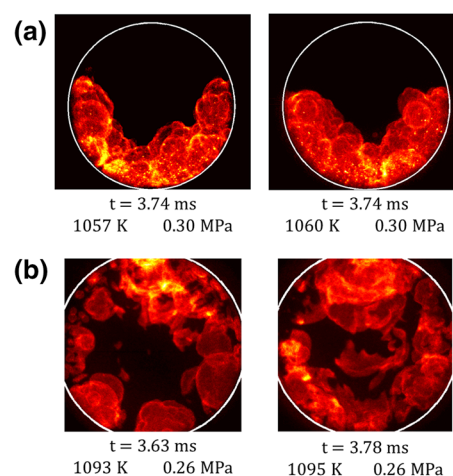


Fig. 7 **a** The combustion of *n*-heptane (21 % O₂/Ar, $\phi = 0.5$), after the shock tube *was not* cleaned, was recorded at 10 kHz with 5 μ s exposure time. The *left* image was acquired after three experiments were performed *without* cleaning, and the *right* image was acquired after four experiments were performed *without* cleaning. **b** The combustion of *n*-heptane (21 % O₂/Ar, $\phi = 0.5$), after the last 2 m of the shock tube *was* cleaned, was recorded at 12 kHz with 5 μ s exposure time. The initial reflected shock temperatures and pressures were labeled for each experiment. A *white outline* was included to mark the location of the shock tube wall

It is important to mention that for the other case studies presented previously, the shock tube was cleaned before each run. Confirming that an unclean shock tube changes the qualitative structure of preignition reactions was not surprising, but was a reminder that careful control of experimental variables is needed to achieve homogeneous or near-homogeneous combustion in reflected shock experiments. End-wall imaging has the potential to be a valuable tool for validating other aspects of shock tube performance and for facilitating further development of best practices for shock tube operation.

4 Conclusion

High-speed end-wall imaging of OH* chemiluminescence was shown to be a powerful tool for understanding time-resolved, spatial details about shock tube kinetics experiments. The end-wall window provides new access for imaging of the structure and location of the earliest reaction zones in the shock tube, as well as the temporal development.

Three case studies that illustrated the utility of the technique were presented. An estimate of the temperature variability throughout the test section was found to be around 0.5 % for the test condition presented (*n*-heptane, 21 % O₂/Ar, $\phi = 0.5$). The window recessions were found to cause initial flames to form at the window location. The importance of routine shock tube cleaning was also demonstrated.

Acknowledgments This material is based upon work supported by the US Army Research Laboratory and the US Army Research Office under Contract/Grant Number W911NF1310206, with Ralph Anthenien as contract monitor. We acknowledge loan of the intensified camera system from an AFOSR-sponsored research program. V.A.T. was supported by the Gabilan Stanford Graduate Fellowship and the National Science Foundation Graduate Research Fellowship Program (Grant No. DGE-114747). Any opinion, findings and conclusions or recommendations expressed in this material are those of the authors(s) and do not necessarily reflect the views of the National Science Foundation. M.F.C. was supported by a National Defense Science and Engineering Graduate Fellowship (32CFR168a).

References

1. W. Bleakney, D.K. Weimer, C.H. Fletcher, The shock tube: a facility for investigations in fluid dynamics. *Rev. Sci. Instrum.* **20**(11), 807–815 (1949)
2. R.K. Hanson, D.F. Davidson, Recent advances in laser absorption and shock tube methods for studies of combustion chemistry. *Prog. Energy Combust. Sci.* **44**, 103–114 (2014)
3. D.J. Vermeer, J.W. Meyer, A.K. Oppenheim, Auto-ignition of hydrocarbons behind reflected shock waves. *Combust. Flame* **18**, 327–336 (1972)
4. K. Fieweger, R. Blumenthal, G. Adomeit, Self-ignition of S.I. engine model fuels: a shock tube investigation at high pressure. *Combust. Flame* **109**(4), 599–619 (1997)
5. J. Herzler, L. Jerig, P. Roth, Shock-tube study of the ignition of propane at intermediate temperatures and high pressures. *Combust. Sci. Technol.* **176**(10), 1627–1637 (2004)
6. O.G. Penyazkov, K.L. Sevrouk, V. Tangirala, N. Joshi, High-pressure ethylene oxidation behind reflected shock waves. *Proc. Combust. Inst.* **32**(2), 2421–2428 (2009)
7. K.A. Heufer, H. Olivier, S.P. Medvedev, S.V. Khomik, Optical investigation of shock induced ignition of different biofuels. in *Proceedings of the 23rd ICDERS*, University of California, Irvine, CA, 24–29 July 2011
8. J. Yoo, D. Mitchell, D.F. Davidson, R.K. Hanson, Planar laser-induced fluorescence imaging in shock tube flows. *Exp. Fluids* **49**, 751–759 (2010)
9. M. Wegener, M. Sutcliffe, R. Morgan, Optical study of a light diaphragm rupture process in an expansion tube. *Shock Waves* **10**, 167–178 (2000)
10. A.B. Mansfield, M.S. Wooldridge, H. Di, X. He, Low-temperature ignition behavior of iso-octane. *Fuel* **139**, 79–86 (2015)
11. B.D. Stojkovic, T.D. Fansler, M.C. Drake, V. Sick, High-speed imaging of OH* and soot temperature and concentration in a stratified-charge direct-injection gasoline engine. *Proc. Combust. Inst.* **30**, 2657–2665 (2005)
12. V. Nori, J. Seitzman, Evaluation of chemiluminescence as a combustion diagnostic under varying operating conditions. in *46th AIAA Aerospace Sciences Meeting and Exhibit*, Reno, Nevada, 7–10 Jan 2008
13. C.T. Bowman, D.J. Seery, Chemiluminescence in the high-temperature oxidation of methane. *Combust. Flame* **12**, 611–614 (1968)
14. H.N. Najm, P.H. Paul, C.J. Mueller, P.S. Wyckoff, On the adequacy of certain experimental observables as measurements of flame burning rate. *Combust. Flame* **113**, 312–332 (1998)
15. M.F. Campbell, A.M. Tulgestke, D.F. Davidson, R.K. Hanson, A second-generation constrained reaction volume shock tube. *Rev. Sci. Instrum.* **85**, 055108 (2014)
16. M.F. Campbell, T. Parise, A.M. Tulgestke, R.M. Spearrin, D.F. Davidson, R.K. Hanson, Strategies for obtaining long constant-pressure test times in shock tubes. *Shock Waves* **25**(6), 651–665 (2015)
17. M.F. Campbell, Studies of biodiesel surrogates using novel shock tube techniques. Ph.D. Thesis, Stanford University (2014)
18. D.F. Davidson, R.K. Hanson, Interpreting shock tube ignition data. *Int. J. Chem. Kinet.* **36**, 510–523 (2004)
19. D.C. Horning, D.F. Davidson, R.K. Hanson, Study of the high-temperature autoignition of *n*-Alkane/O₂/Ar mixtures. *J. Propuls. Power* **18**(2), 363–371 (2002)